NOVEL NANOLASERS, NANO-LEDS, AND MODAL CUTOFF CONFINEMENT LIGHT EMITTERS

BY

AKIRA MATSUDAIRA

DISSERTATION

Submitted in partial fulfillment of the requirements
for the degree of Doctor of Philosophy in Electrical and Computer Engineering
in the Graduate College of the
University of Illinois at Urbana-Champaign, 2012

Urbana, Illinois

Doctoral Committee:

Professor Shun Lien Chuang, Chair and Director of Research
Professor Kent D. Choquette
Professor J. Gary Eden
Professor Joseph W. Lyding

ABSTRACT

Semiconductor metal nanocavity lasers and light emitting diodes together with novel modal cutoff confinement light emitters are investigated for optical interconnection application in future dense photonic integrated circuits. Several different cavity structures are designed, processed, and characterized, and demonstrate operation with current injection at room temperature. We first examined metal-cavity quantum-dot surface-emitting micro-lasers. Different sizes of metal-DBR cavities are fabricated with cavity volume reduction both in the lateral and vertical dimensions following our theoretical design rules to optimize the performance. One of the smallest electrical injection lasers is demonstrated with a minimum diameter of 1-μm and a minimum hybrid DBR-Ag mirror of only 5.5 pairs. From the analysis of various sizes of diameter devices, it is found that self-heating is significant in the smaller diameter devices due to both the higher series resistance and higher threshold gain leading to a high carrier density.

For the further cavity volume reduction, we have designed, fabricated, and characterized metal-encapsulated nano-light-emitters with bulk semiconductor in the active region. The first principal design rule is used to estimate the fundamental mode resonance and threshold condition. The result based on this design rule agrees very well with the numerical three-dimensional calculation. The device recipes have been developed through multiple iterations from the device characterization. The smallest metal cavity diode emitter with electrical injection is 0.086 λ_0^3 in terms of emitting wavelength at room temperature. It is shown that the series resistance of metal-encapsulated nanocavities is much smaller than the metal

coated VCSEL, suppressing the heat generation for the small diameter devices. The fabrication improvement shows a narrow linewidth cavity mode in the metal nanocavity with a volume of 1.23 λ_0^3 at room temperature.

To solve the problem of the high radiation loss caused by a metal mirror, we proposed novel nano/micro-cavities edge-emitting laser using the mode-cutoff reflection of the fundamental TE mode from a metal-semiconductor-metal (MSM) region. The devices are examined by multiple aspects for their function, both qualitatively from the principle of operation and quantitatively from the analytical study of reflection coefficient and numerical simulations by the 2D and 3D models for practically designed devices. The numerical simulations including the metal loss suggest that room temperature lasing with a reasonable threshold material gain is achievable. We have also developed processing recipes to fabricate the device without any semiconductor dry-etching process. The preliminary electrical and optical characterizations of the proposed devices are performed showing excellent I-V characteristics with a thin hetero-junction diode. The light output curve shows a super-linear behavior suggesting possible lasing in the cavity volume less than λ_0^3.

To my family

ACKNOWLEDGMENTS

First I would like to thank my research adviser, Professor Shun Lien Chuang, for the great opportunity to perform this research. His unlimited resources and insightful guidance encouraged me when I faced challenges. His generous support and passion for the research always motivated me to tackle this challenging problem. I also thank his wife, Lolita, for her delicious cooking at the house party and many interesting stories. This work would never have been completed without the help of the many group members. Special thanks to Chien-Yao Lu who taught me cleanroom processing at the beginning and gave me insight in the experiments. We spent never-ending nights in the cleanroom and laboratory. I have had the privilege of working with great group members who provided me with fruitful discussions and technical assistance: Shu-Wei Chang, Adrian Chi-Yu Ni, Thomas O'Brien, Benjamin Kesler, Daniel Zuo, Michael Pengfei Qiao, and Meng Zhang. My life in Urbana-Champaign was never boring with them and they became my important friends for life. I greatly appreciate Professor Dieter Bimberg at Technical University of Berlin and his group members for collaboration on quantum-dot VCSELs and the chance to visit Berlin to conduct experiments. I also appreciate Dr. Liming Zhang of Bell Laboratories, Alcatel-Lucent, for collaborating on crystal growth on metal nanocavity lasers. Finally, I would like to acknowledge the Department of Electrical and Computer Engineering at UIUC, and the Defense Advanced Research Projects Agency (DARPA) for financial support throughout my studies.

TABLE OF CONTENTS

LIST OF TABLES

LIST OF FIGURES

CHAPTER 1

INTRODUCTION TO NANOLASERS

1.1 Motivation

Semiconductor lasers have contributed significantly to our society by enabling long-haul telecommunications in world-wide internet connections. Other applications include the DVD players, printers, optical mouses, range finders, barcode readers, laser surgery and so on. Without semiconductor lasers' capability of high speed signal modulation and dense wavelength division multiplexing technology, today's information society would be impossible. Today, optical communications range from long distance to short distance, such as super-computer nodes, rack-to-rack, and board-to-board high data rate communications. Recently, optical interconnects for chip-to-chip communication or even intra-chip communications have been intensely studied as a solution to existing copper wire transmission lines [1-3]. Optical interconnects have several advantages over electrical signal transceivers, such as signal latency for short distance communications, high bandwidth per channel, scalable architecture with wavelength division multiplexing, absence of bandwidth dependent loss, low crosstalk, and no impedance matching terminating problems. As the technology nodes shrink in size each year, leading companies in the electrical chip industry have already developed integrated optical transceivers for the future shortcomings of Si chip interconnection [4].

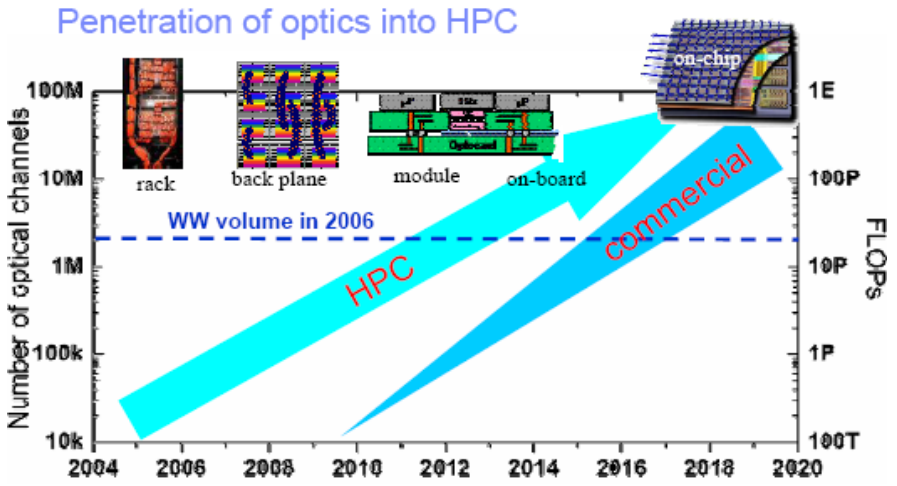

Figure 1.1 Prediction of the number of optical channels and floating-point operations per second (FLOPs) in high performance computers (HPC) in the near future by IBM. As processing power increases exponentially, millions of optical channels become necessary (IBM).

As the optical link is used in the compact systems such as on-board or on-chip interconnect solutions, lasers need to satisfy the application criteria such as easy integration, ultra-small footprints, low energy consumption, and operation at room temperature. The conventional edge emitting semiconductor lasers widely used in telecommunications industry are over 100 μm in length, which is too large for integrated optical interconnection. Today, 2D arrayed vertical-cavity surface-emitting lasers (VCSELs) are widely used for dense optical light sources for their small footprints and low manufacture cost. The typical mesa sizes are generally a few tens of micrometers. Figure 1.1 shows prediction of the necessary number of optical channel and floating-point operations per second (FLOPs) in high performance computers (HPC) from IBM. As computer processing power increases exponentially, millions of lasers need to be integrated soon. As this trend continues, optical sources need to be integrated with processors from module level such as electrical-optical transceiver to chip level for direct hybrid integration.

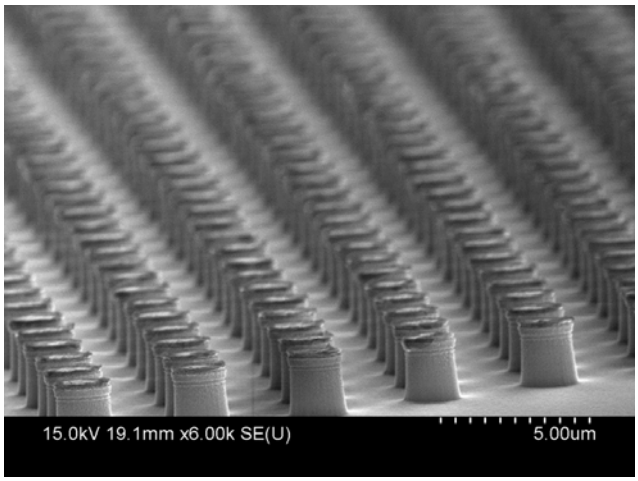

Figure 1.2 Dense arrays of nanocavities fabricated in our laboratory. Nanolasers will have numerous applications including optical interconnect, bio-sensors, and optical processors.

The small footprint semiconductor nanolaser will be the key component in the future optical interconnects systems due to its easier integration to CMOS, electrical pumping operation, and high bandwidth capability. The miniaturization of laser cavity itself has numerous advantages over conventional lasers. Power consumption per bit is significantly reduced due to small cavity volume, which is crucial to replace copper transmission line in CMOS [1, 3]. Optical modulation speed is expected to be improved in nanocavity for enhanced Purcell effect on spontaneous emission [5-8].

Figure 1.2 shows scanning electron microscopy images of dense arrayed nanocavities fabricated in our laboratories. Other than optical interconnect applications, there are many possible applications of nanolasers. One example is biosensing using plasmonic nanolasers for improved detection resolution, sensitivity, and enhanced nonlinear spectroscopy [9]. Other interesting applications are using nanolasers as optical logic gates for digital photonics [10] or dense array of nanolasers for massively parallel processing systems [11]. In a

rapidly changing technology driven society, only our imagination can limit the possibilities of nanolasers applications. In this work, we target metallic nano/micro-cavity lasers for ultra-small volume optical interconnection solutions for the next generation integrated chips.

1.2 State of the Art

In recent years, there have been significant efforts to reduce the size of semiconductor lasers. One of the approaches is using photonic crystals for nanocavities [12-13]. However the lateral confinement of the optical cavity usually requires a number of photonic crystal periods, making it hard to ultimately shrink the device size to something comparable to the optical wavelength. On the other hand, metal is used for plasmonic mode lasing in nanowires [14], and gold particle spaser lasers [15]. These devices demonstrate lasing in deep sub-wavelength dimension beating the well-known diffraction limit ($\lambda_0/2n$). However, they are optically pumped and have serious challenges for practical applications, including controlling device positioning and integration due to bottom up fabrication. Recently, metallic nanocavity semiconductor lasers fabricated by top-down approach have been intensively studied. Figure 1.3 shows a summary of the state-of-the-art metallic semiconductor nano/micro-lasers plotted for the cavity volume as a function of operating temperature. From the work by M. Hill et al. [16] demonstrating sub-wavelength electrical injection lasers at 77K in 2007, several groups have demonstrated metallic nanocavity lasers [16-23]. The key idea is using a high reflective metal for better optical confinement cavity. At cryogenic temperature,

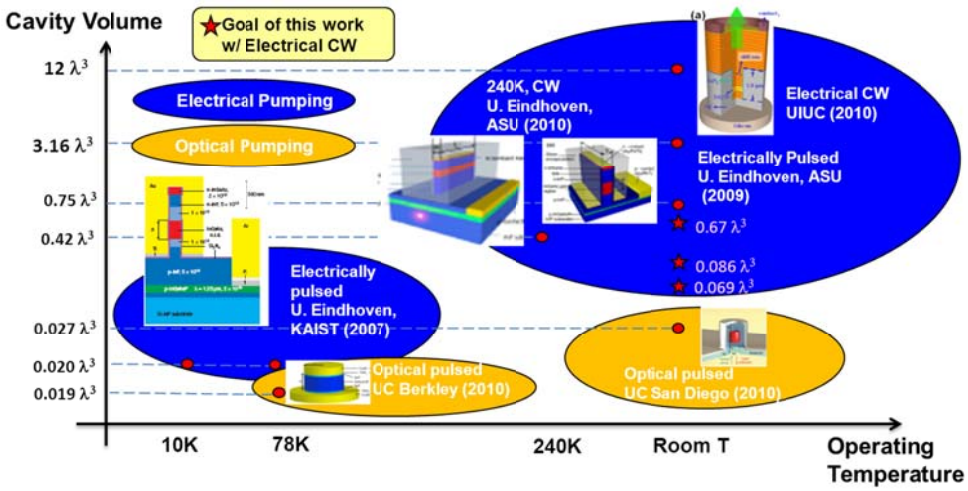

Figure 1.3 Summary of the state-of-the-art metallic semiconductor nanolasers plotted based on the cavity volume size and the operating temperature.

sub-wavelength lasers with surface plasmonic mode are demonstrated because high semiconductor material gain can overcome the low optical loss at low temperature. Another useful approach for nanolasers is using optical pumping. There are two advantages over the laser performances using optical pumping instead of current injection: suppressing excess heat generation, and simpler fabrication steps. Optical pumping can generate electron and hole pairs slightly above the band edge without generating much heat. Without a current bias, it can suppress ohmic heat generation and hot carriers under the biased field. The device fabrication becomes much easier for optical pumping without consideration of electrical isolation between the anode and the cathode and the p-i-n junction doping design. However, electrical injection devices working at room temperature are critical for practical applications. Thus, our research focuses on nano/micro-cavity lasers with electrical injection configuration operating at room temperature.

1.3 Thesis Overview

For practical applications, it is important that nanocavity lasers operate with electrical injection at room temperature. Thus, all our devices are designed and fabricated strictly following these constraints. Figure 1.4 shows the summary of the devices in this thesis. The dissertation first demonstrates metal-cavity quantum-dot (QD) surface-emitting micro-lasers in Chapter 2. The strategy is to reduce the cavity volume of VCSEL both in lateral and vertical direction by using metal for better optical confinement and strong reflection. The QD gain is used in an active layer to suppress the surface recombination and better thermal property. We discuss the cavity design rules, processing steps, and performance of various sizes of lasers. Single mode lasing performances, thermal property, and the cavity volume scaling law are discussed. In Chapter 3, metal-encapsulated cavity light emitters are studied for further cavity volume reduction. We designed, processed and characterized several cavities with different resonant modes. One of the challenges in metal-encapsulated lasers is cleanroom processing for the defect-free cavity and electrical isolation between the anode and cathode contacts. Challenges and improvements of device fabrication are discussed with comparison of device performances. Finally, novel edge-emitting nanocavity lasers are proposed in Chapter 4. The device is designed to overcome the high mirror loss and metallic loss in metal-encapsulated nanocavities. In this device, metal is not used as incident light reflector, but it is used to form the modal cutoff structure for strong feedback without much optical field overlap in metal. The principle of operation, analytical study, and numerical simulation results are

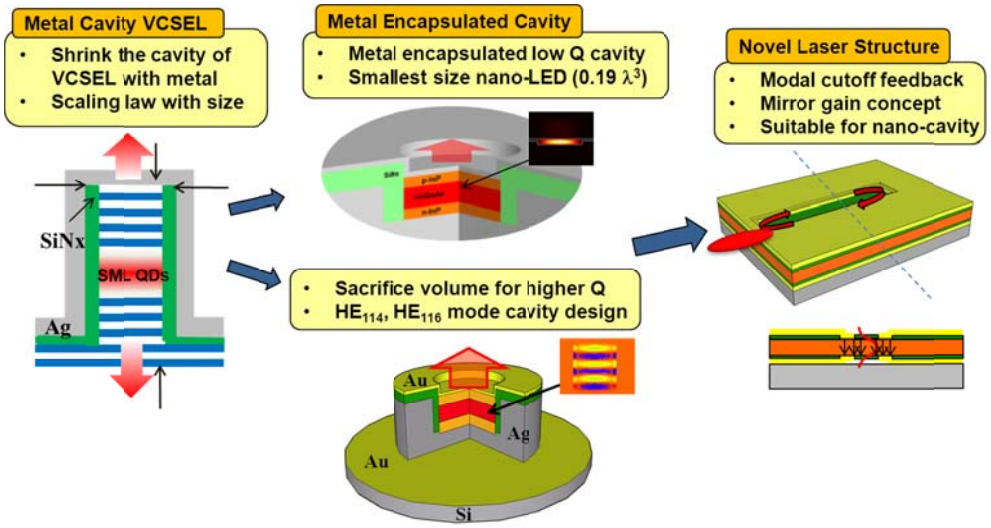

Figure 1.4 Research overview of this thesis. All devices are specifically designed for optimized cavity, processed in cleanroom, and characterized in our laboratory.

presented. The simulated device is fabricated in the cleanroom at MNTL at UIUC. The electrical and optical characterizations are performed in Professor Chuang's laboratory.

1.4 References

[1] D. A. B. Millar, "Rationale and challenges for optical interconnects to electronic chips," *Proc. IEEE*, vol. 88, no. 6, Jun. 2000.

[2] M. J. Kobrinsky, B. A. Block, J. F. Zheng, B. C. Barnet, E. Mohammed, M. Reshotko, F. Robertson, S. List, I. Young, K. Cadien, "On-chip optical interconnects" *Intel Technology Journal*, vol. 8, issue. 2, May 10, 2004.

[3] D. A. B. Millar, "Device requirements for optical interconnects to silicon chips," in *Proc. IEEE*, vol. 97, pp. 1166-1185, Jun. 2009.

[4] A. Alduino et al., "Silicon photonics WDM link with hybrid silicon lasers," in *Integrated Photonic Research, Silicon and Nanophotonics*, OSA technical digest, PDIMI5, 2010.

[5] E. K. Lau, A. Lakhani, R. S. Tucker, and M. C. Wu, "Enhanced modulation bandwidth of nanocavity light emitting devices," *Opt. Expresss*, vol. 17, no. 10, pp. 7790-7799, Apr. 2009.

[6] T. Suhr, N. Gregersen, K. Yvind, and J. Mørk, "Modulation response of nanoLEDs and nanolasers exploiting Purcell enhanced spontaneous emission," *Opt. Expresss*, vol. 18, no. 11, pp. 11230-11241, May 2010.

[7] H. Altug, D. Englund, and J. Vučković, "Ultrafast photonic crystal nanocavity laser," *Nature Physics*, vol. 2, pp. 484-488, Jul. 2006.

[8] E. Yablonovitch, "Metal optics, optical antennas, and spontaneous hyper-emission," Proceedings of 10th IEEE *International Conference on Nanotechnology Joint Symposium with Nano Korea*, Kintex, Korea, Aug. 2010.

[9] J. N. Anker, W. P. Hall, O. Lyandres, N. C. Sham, J. Zhao, and R. P. V. Duuyne, "Biosensing with plasmonic nanosensors", *Nature Materials*, vol. 7, pp.442-453, Jun. 2008.

[10] M. Kajita, K. Tasahara, T. J. Kim, D. T. Neilson, I. Ogura, I. Redmond, and E. Schenfeld, "Wavelength-division multiplexing free-space optical interconnect networks for massively parallel processing systems," *Applied Optics*, vol. 37, no. 17, pp. 3746-3755, 1998.

[11] M. T. Hill, "Micro and nanolasers for digital photonics," *Proceedings of the European Conference on Integrated Optics (ECIO)*, pp. WC0-64/67 April, 2007.

[12] H. G. Park, S. H. Kim, S. H. Kwon, Y. G. Ju, J. K. Yang, J. H. Baek, S. B. Kim, and Y. H. Lee, "Electrically driven single-cell photonic crystal laser," *Science*, vol. 305, pp. 1444-1447, 2004.

[13] A. V. Giannopoulos, Y. Li, C. M. Long, J. Jin, and K. D. Choquette, "Optical properties of photonic crystal heterostructure cavity lasers," *Opt. Express*, vol. 17, no. 7, pp. 5379-5390, 2009.

[14] R. F. Oulton, V. J. Sorger, T. Zentgraf, R. M. Ma, C. Gladden, L. Dai, G. Bartal, and X. Zhang, "Plasmon lasers at deep subwavelength," *Nature* 461, 629-632, 2009.

[15] M. A. Noginov, G. Zhu, A. M. Belgrave, R. Bakker, V. M. Shalaev, E. E. Narimanov, S. Stout, E. Herz, T. Suteewong, and U. Wiesner, "Demonstration of a spaser-based nanolaser," *Nature* 460, 1110-1112, 2009.

[16] M. T. Hill, Y. S. Oei, B. Smalbrugge, Y. Zhu, T. de Vries, P. J. van Veldhoven, F. W. M. van Otten, T. J. Eijkemans, J. P. Turkiewicz, H. de Waardt, E. J. Geluk, S. H. Kwan, Y. H. Lee, R. Notzel, and M. K. Smit, "Lasing in metallic-coated nanocavities," *Nat. Photon.*, vol. 1, pp. 589-594, 2007.

[17] M. T. Hill, M. Marell, E. S. P. Leong, B. Smalbrugge, Y. Zhu, M. Sun, P. J. van Veldhoven, E. J. Geluk, F. Karouta, Y. Oei, R. Notzel, C. Z. Ning, and M. K. Smit, "Lasing in metal-insulator-metal sub-wavelength plasmonic waveguides," *Opt. Express*, vol. 17, pp. 11107-11112, 2009.

[18] M. P. Nezhad, A. Simic, O. Bondarenko, B. Slutsky, A. Mizrahi, L. Feng, V.

Lomakin, and Y. Fainman, “Room temperature subwavelength metallo-dielectric lasers,” *Nat. Photon.*, vol. 4, pp. 395-399, 2010.

[19] C. Y. Lu, S. W. Chang, S. L. Chuang, T. D. Germann, and D. Bimberg, “Metal-cavity surface-emitting microlaser at room temperature,” *Appl. Phys. Lett*., vol. 96, p. 251101, 2010.

[20] C. Y. Lu, S. W. Chang, S. L. Chuang, T. D. Germann, U. W. Pohl, and D. Bimberg, “CW substrate-free metal-cavity surface microemitters at 300 K,” *Semicond. Sci. Technol*., vol. 26, no. 1, pp. 014012-014018, 2011.

[21] C. Y. Lu, S. L. Chuang, A. Mutig, and D. Bimberg, “Metal-cavity surface-emitting microlaser with hybrid metal-DBR reflectors,” *Opt. Lett*., vol. 36, no. 13, pp. 2447-2449, 2011.

[22] K. Yu, A. M. Lakhani, and M. C. Wu, “Subwavelength metal-optic semiconductor nanopatch lasers,” *Opt. Express*, vol. 18, pp. 8790-8799, 2010.

[23] S. H. Kwon, J. H. Kang, C. Seassal, S. K. Kim, P. Regreny, Y. H. Lee, C. M. Lieber, and H. G. Park, “Subwavelength plasmonic lasing from a semiconductor nanodisk with silver nanopan cavity,” *Nano Lett*. vol. 10, pp. 3679-3683, 2010.

CHAPTER 2

METAL-CAVITY QUANTUM-DOT SURFACE EMITTING MICRO LASERS

2.1 Overview

Since the first demonstration of the surface-emitting semiconductor lasers with a pulsed injection at 77K in 1979 [1], vertical cavity surface-emitting lasers (VCSELs) have attracted much research and development effort for various applications. Compared with semiconductor edge-emitting lasers, VCSELs successfully reduced the manufacturing cost largely due to the small footprint of the devices and in-situ device testing during processing. AlGaAs/GaAs semiconductor compound materials offer excellent refractive index contrast without lattice strain, which is suitable for high reflectivity in distributed Bragg reflectors (DBRs). Further, the use of AlAs oxidation allows for a small aperture for carrier and optical confinement of only a few μm diameter devices [2]. Among the commercially available semiconductor lasers, VCSELs have the smallest cavity volume. Due to the small current density and surface emitting geometry with two-dimensional arrays, VCSELs are a promising candidate for high speed optical interconnects in future photonic integrated circuits.

In this chapter, we study metal-cavity surface emitting lasers (MCSELs). For future dense photonic integrated circuit, not only the active area of the lasers, but also the device mesa area, becomes important. In order to increase the integration

density, MCSELs confine the optical mode laterally with sidewall metal coating and vertically with hybrid mirrors which enhance DBR reflectivity with metal [3-6]. Sidewall metal coating can increase the device density by eliminating the mesa structure and suppressing optical crosstalk among the neighboring devices in dense laser arrays. In addition, metal coating close to the active region is expected to remove the heat more effectively [5]. In earlier work on MCSELs, multiple quantum-well (QW) layers are used as the gain material performing electrical injection continuous-wave lasing at room temperature [3-6]. In this work, we used sub-monolayer (SML) quantum dots (QDs) for reducing the surface non-radiative recombination by lateral carrier confinement, for less temperature sensitive gain, and for low chirp in high-speed modulation applications. We show the concept of the design rules, optimization, and scaling laws of MCSEL cavity volume along both lateral and vertical directions. We then demonstrate the device fabrication and characterization of various sizes of MCSELs and show comparison with our theoretical results.

2.2 Device Structures and Design

2.2.1 Device Structure

The device schematic of MCSEL is shown in Fig. 2.1. The epiwafer structure was grown by molecular beam epitaxy (MBE) with an active medium consisting of three groups of InGaAs SML quantum dots spaced by a 13-nm-thick GaAs layer [7-9]. Each group consists of ten layers of stacked SML quantum dots formed by depositing 0.5 monolayer (ML) InAs capped by 2.2 ML GaAs in each layer (Fig. 2.1). The top (bottom) distributed-Bragg reflector mirror consists of

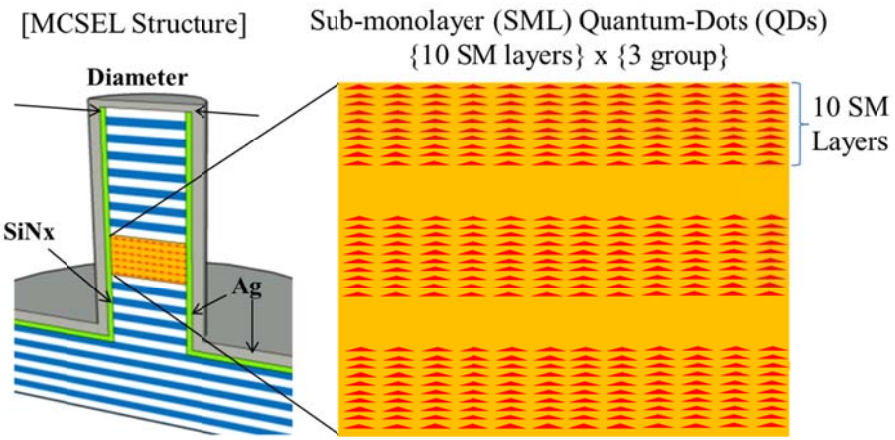

Figure 2.1 Device schematic of metal cavity surface-emitting laser (MCSEL) and active layer quantum dots (QDs).

20-pairs (33-pairs) of *p*-doped (*n*-doped) alternating $Al_{0.9}Ga_{0.1}As$/GaAs quarter-wavelength layers. An optical cavity of a 3/2-wavelength with the QD active region is sandwiched between the top and bottom DBRs.

The micro pillar with the DBRs and the active SML QD region is surrounded by a thin SiN_x layer which serves as an electrical isolator between top anode contact and n-type bottom DBR, an optical cladding layer between pillar and lossy silver layer, and a passivation layer for the semiconductor surface dangling bonds damaged from the dry etching process. Outside of the SiN_x layer is uniform covering of metal (Ag) for optical modal confinement as well as the top electrical contact. Metals, with an excellent thermal conductivity, have been used to conduct and dissipate the heat for many important applications. The free electrons inside the metal not only give rise to its high thermal conductivity but also function as excellent optical confinement in lateral directions. As the pillar diameter becomes small, lateral optical confinement becomes more important. We study the performance of the micro-cavity laser and its scaling law with the cavity volume

in both the lateral direction (diameter of the post) and the vertical direction (number of top DBR pairs). Light output is collected either from the top through the hybrid DBR-metal mirror or from the bottom DBR after substrate removal and flip-chip bonding to silicon substrate.

2.2.2 Quantum-Dot Gain Medium

Quantum dots (QDs), due to their delta-function-like density of state, can realize lasers with temperature-insensitive threshold [10]. Moreover, it has been shown that three-dimensional carrier confinement in semiconductor QDs enables high differential efficiency [11], superior threshold characteristics [12], and small signal modulation bandwidth as high as 11 GHz [13-14]. InAs QD lasers have been extensively studied as a high performance optical source for 1.3 μm optical communication systems. Infinite [15] or negative [16] characteristic temperatures have been demonstrated near room temperature.

In micro- and nanoscale pillar lasers, cavity loss becomes larger as cavity volume shrinks due to optical loss from metal and short cavity radiation. Thus, high gain in active layer is the key to design the micro- and nanopillar MCSEL. In micro- and nano-size etched pillar, dry-etching sidewall surface has many carrier trapping sites due to dangling bonds generated from the dry etching process, and impurity atoms which are embedded from reacting atoms during plasma etching. These undesired sites trap electrons or holes causing non-radiative recombination. In active region, the surface to volume ratio becomes

$$r_{s/v} = \frac{S}{V} = \frac{2\pi\left(D/2\right)t}{\left(D/2\right)^2 \pi t} = \frac{4}{D} \tag{2.1}$$

where t is the active layer thickness and D is the pillar diameter. As the

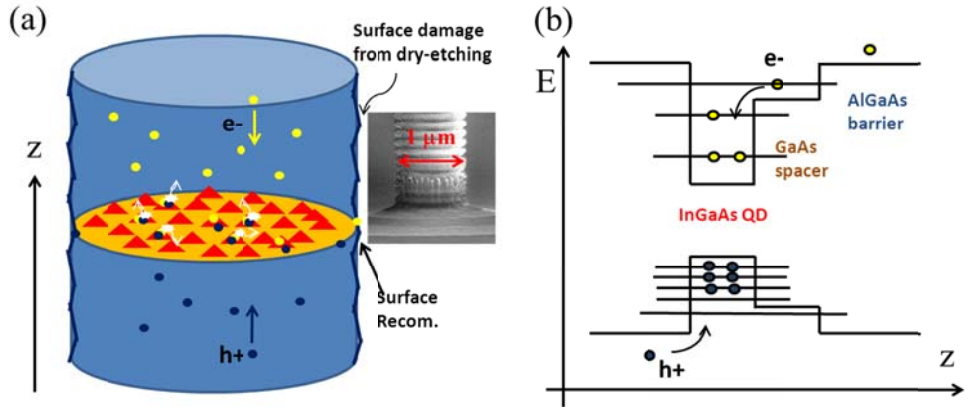

Figure 2.2 (a) Illustration of carrier recombination of quantum dots (QDs) in micro-pillar structure. (b) Energy band diagram of InGaAs QDs with quantum-well like GaAs spacer layer.

diameter of MCSEL becomes smaller, more carriers are consumed in non-radiative surface recombination, which generates heat and does not contribute to an optical gain.

Compared with the bulk or quantum-well (QW) active layer, QDs offer unique advantages. Some of the QD carrier recombination processes are illustrated in Fig. 2.2(a). Due to carrier confinement structure in the lateral direction, carriers in the active layer plane (continuous GaAs spacer layer and islands of InGaAs QDs) rapidly relax into QDs as shown in Fig 2.2(b). This relaxation process is usually on the order of pico-seconds and much faster than surface recombination process. Notice that this is not the case in bulk or QW active layer because there are no carrier confinement structures in lateral dimension. Furthermore, sub-monolayer (SML) QDs can realize a significant lateral compositional modulation with high QD density of the order of 10^{12} cm^{-2} ranges [7-9]. This property can improve better carrier confinement and higher gain.

2.2.3 Cavity Design

The cavity design of MCSEL is similar to traditional VCSEL devices, except that there are some design rules which need special attention. First, metal coating on top of the distributed Bragg reflector (DBR) significantly affects the phase of standing-wave pattern as well as the resonant wavelength. The perturbation becomes especially significant for the short cavity devices with a reduced number of DBR pairs. The second is lateral size reduction of the cavity. As the diameter of the cavity becomes smaller, the effective index becomes smaller due to optical mode penetration into both the SiN_x cladding layer and the metal. The resonant wavelength blue shift needs to be taken into account for small diameter devices. Also, the sidewall metal coating induces additional propagation loss, especially to higher order transverse modes.

To understand the design rule for the metal-cavity VCSEL, we start by reviewing the basics of VCSEL cavity and DBR mirrors. Figure 2.3 shows the refractive index profiles around the cavity of our device with the magnitude of the longitudinal standing-wave pattern of the electrical field calculated by the transfer matrix method. The cavity has cladding materials of $Al_{0.3}Ga_{0.7}As$, three groups of QD active layer, and one oxidation layer for a total length of $3\lambda/(2n)$ with a resonant wavelength 981.5 nm with the large diameter devices. The active QD layers are positioned to the center peak of the standing wave. The AlAs oxidation layer is positioned near the node of standing-wave pattern to minimize the scattering. In the metal-coated VCSEL, the scattering is reduced by the well-defined metal shell.

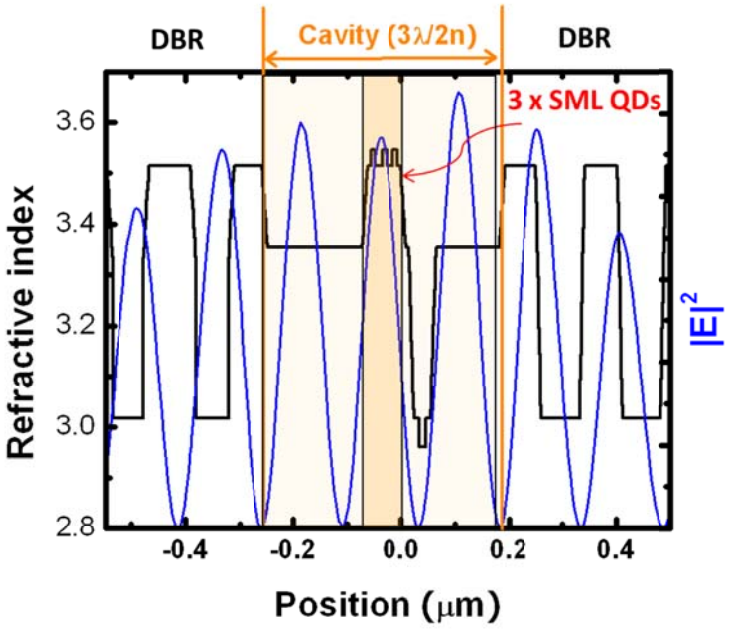

Figure 2.3 Refractive index profiles around the cavity of the device with the longitudinal standing-wave electrical field. The cavity consists of three groups of SML QDs as the active region, a single layer of oxidation layer, and a total length of 3λ/(2n).

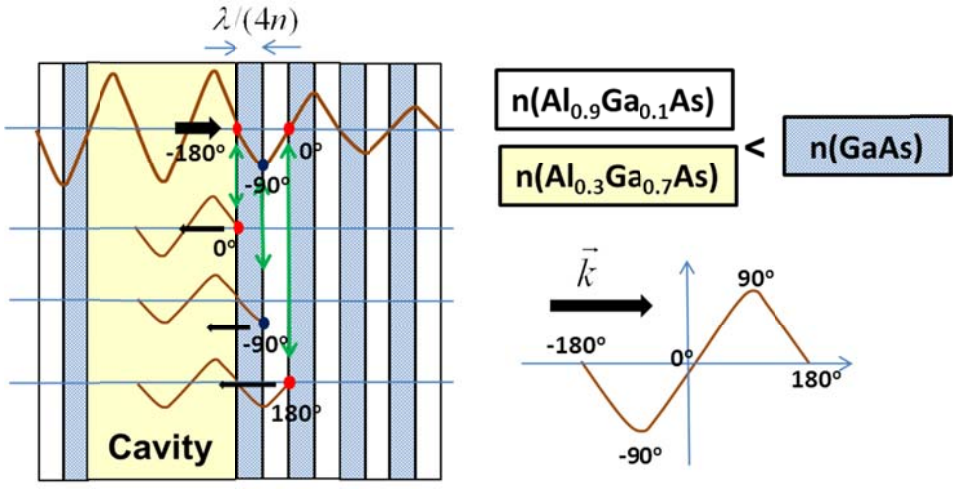

Figure 2.4 Schematic of a distributed Bragg reflector (DBR) illustrating that the partial by reflected light from each layer propagates backward in phase.

Figure 2.4 shows the basic idea of DBR mirrors. The DBR consists of quarter-wavelength alternative layers of different refractive index. Let us consider the incident wave from the cavity (left to right) partially reflected at each interface layer. For a normally incident plane wave, the reflection coefficient from low index to high index (GaAs) is

$$r_{AlGaAs \to GaAs} = \frac{n(AlGaAs) - n(GaAs)}{n(AlGaAs) + n(GaAs)} < 0 \quad . \tag{2.2}$$

The reflection coefficient is negative. Thus, the partial reflection from "cavity to the 1st GaAs layer" and "AlGaAs layer to GaAs layer" in Fig. 2.4 has a 180^o phase shift by reflection. Note that the wave-vector k changes direction by reflection. The phase angle is defined in the right bottom of Fig. 2.4. On the other hand, the reflection coefficient from the high index (GaAs) to the low index (AlGaAs) is

$$r_{AlGaAs \to GaAs} = \frac{n(GaAs) - n(AlGaAs)}{n(GaAs) + n(AlGaAs)} > 0 \quad . \tag{2.3}$$

The reflection coefficient is positive and the wave phase does not change by reflection. Three layers of partial reflections are illustrated in Fig. 2.4 showing all reflected waves are in phase, and a constructive interference to form the resonant standing-wave pattern. An important observation is that the standing wave forms a node when wave is incident from the low index layer to the high index layer while it becomes a peak when the wave is incident from the high index layer to the low index layer.

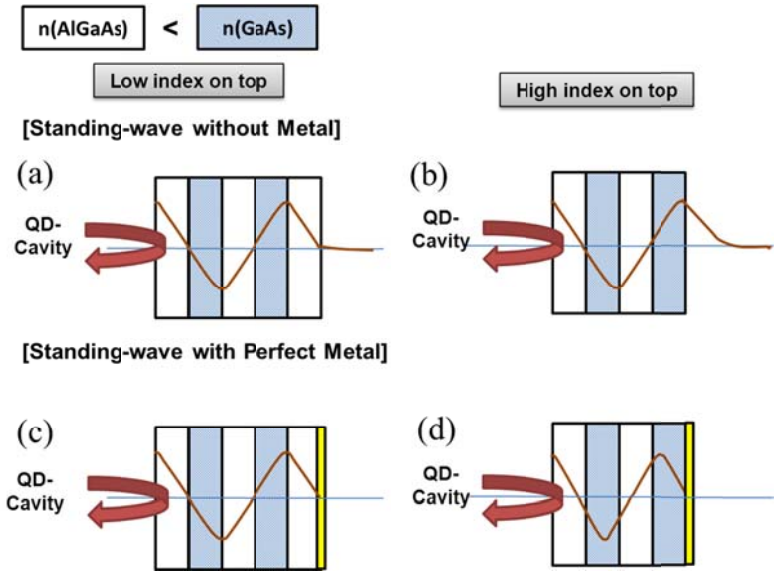

Figure 2.5 Illustration of standing-wave pattern inside the DBR layers with different layers on top. (a) Low index is on the top with an air interface, (b) high index on the top with an air interface, (c) low index on the top with a metal interface, (d) high index on the top with a metal interface.

One of the important design factors of the hybrid DBR-metal mirror is the interface between the top layer of DBR and metal. At the metal interface, the electrical field is defined by the boundary condition of the metal. Figure 2.5 illustrates the standing-wave pattern in the DBR layers with different layers on top. Figure 2.5 (a) and (c) have a low refractive index layer (AlGaAs) on the top whereas (b) and (d) have a high refractive index layer (GaAs) on the top. In a conventional air interface, both cases form the standing-wave peak at high-to-low index interface and node at low-to-high index interface as explained in Fig. 2.4. When a perfect metal conductor is placed on top, the electrical field is forced to zero at the metal interface due to the boundary condition. With a low index interface, the standing wave pattern is not disturbed by metal. On the other hand, a high index interface sets the node at interface and changes the original standing-wave pattern in the DBR layers and shifts the resonant wavelength.

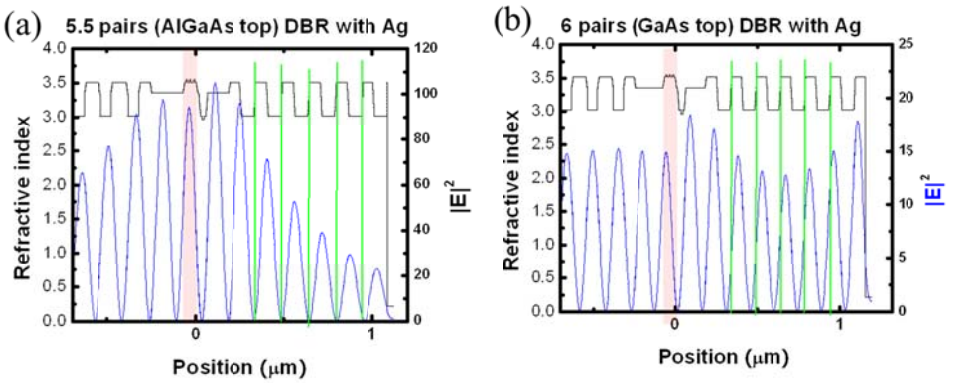

Figure 2.6 The standing-wave profile of the electrical field intensity with the refractive index profile of the layer structure for (a) 5.5 DBR pairs and (b) 6 DBR pairs, both with a 35-nm silver film on top (shown at the position near 1 μm).

We calculated the standing-wave pattern of our layer structures with a silver layer on top using the transfer matrix method [17]. In the numerical calculation, we account for linear composition grading at the GaAs/AlGaAs alternating interface and optical loss from the top metal layer. Figure 2.6 shows the standing-wave pattern for both the 5.5 DBR pairs (low index on top) and 6 DBR pairs (high index on top) with a 35 nm silver cover on top together with the refractive index profile. In this example, we start counting the DBR from the first AlGaAs layer. With a proper design of top layers in the 5.5 DBR pairs, the standing-wave pattern is not disturbed by the silver layer with nodes at low-to-high refractive index interfaces (shown as vertical lines in insets). On the other hand, with 6 DBR pairs, the standing-wave pattern is shifted due to the silver layer and it is not matched with the DBR period anymore. The resonant wavelength is squeezed from 980.6 nm in 5.5 pairs to 971.4 nm in 6 pairs. Also the threshold gain of 6 DBR pairs is increased more than ten times from that of the 5.5 DBR pairs. This is not only from the reduced DBR reflectivity but also from the smaller gain and the standing-wave overlap as shown in Fig. 2.6.

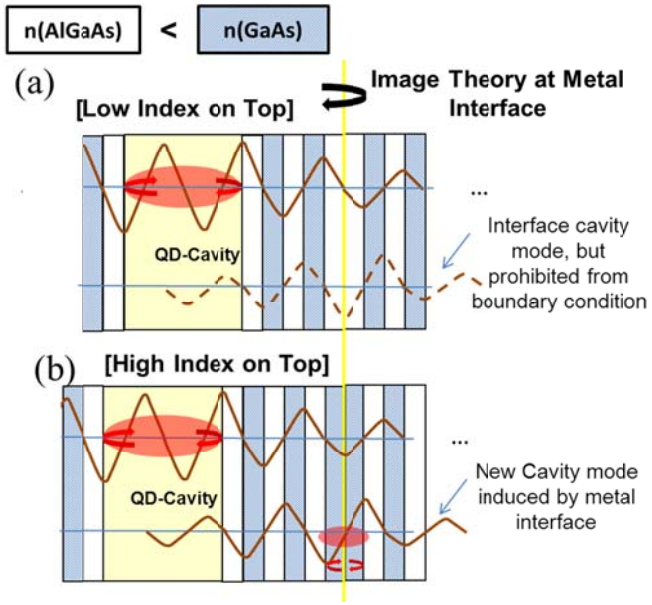

Figure 2.7 Comparing (a) half-integer-pair DBR (top layer is low index) and (b) integer-pair DBR (top layer is high index) for standing wave at resonant wavelength. For both cases, perfect metal is assumed at top interfaces and the image theory is used to find possible resonant modes.

Another interesting observation from the calculation results in Fig. 2.6 is envelope function of the resonant standing wave. The 5.5 DBR case has peak near the active layer cavity and the field decay exponentially on both sides. On the other hand, the 6 DBR case has two peaks: one in the cavity and another near the silver interface on the top. The relative field intensity is also much smaller in the 6.0 DBR pairs. This can be explained using image theory with an approximation that the silver acts as a perfect metal. Figure 2.7 illustrates both low index top (integer plus half DBR) and high index top (integer DBR) cases. By applying image theory at the silver interface, both structures form $\lambda/(2n)$ cavity at the silver interface. The standing-wave pattern seen from this second cavity is drawn for both cases according to the principle depicted in Fig. 2.4. However, the standing-wave pattern in Fig. 2.7(a) is not allowed because image theory prohibits

non-zero field at the mirror axis. On the other hand, the standing-wave pattern in Fig. 2.7(b) has a valid field pattern with a node at the mirror axis. Since the standing wave in the original cavity and the interface cavity has a phase shift of 45^{o}, these two resonant fields interfere with each other and construct an envelope function with two peaks as observed in Fig. 2.6(b).

The metal effects on top of the reduced number of DBR pairs suggest interesting applications other than MCSEL. According to our transfer matrix method calculation, the threshold gain of 5.5-DBR-pairs device is 4,162 cm^{-1}, whereas the 6-DBR-pairs device is 39,235 cm^{-1}, both with the 35 nm top silver layer. This strong contrast of threshold gain is particularly interesting to discriminate the higher order modes in high power single-mode VCSEL applications. Due to strong phase perturbation from the metal, this device may be able to outperform the air interface surface relief method [18].

2.2.4 Size Dependent MCSEL Model

To model the cavity dependence of MCSEL, we separated the problem into two parts; one is a two-dimensional cross-sectional plane and the second part is along the vertical direction propagation. Due to the well-defined circular waveguide cross section with a metallic sidewall, the metal plasmonic effect, modal dispersion, and the effective index can be obtained by solving the Maxwell's equations. Figure 2.8(a) inset shows the cross-sectional view of the metal cavity laser. The refractive index profile contains the radial material distribution information in cylindrical layers. The propagation constant k_z of the vector mode of the Maxwell's equations for a cylindrical waveguide should be solved starting from the wave equation for the longitudinal E_z and H_z components:

$$\left[\nabla_t^2 + (n(\rho))^2 k_0^2\right] E_z = k_z^2 E_z \tag{2.4}$$

where a similar equation holds for the H_z component. The effective index n_{eff} of the guided mode and the modal (intensity) absorption loss α_i are obtained from the propagation constant of the mode: $k_z = k_0 n_{eff} + i \alpha_i /2$, where k_0 is the free space wave number. All other transverse electrical and magnetic field components are obtained from the Maxwell's equations and matching the boundary conditions at each interface. The transfer matrix method is used to design the thickness of the layered structure and to predict the resonance wavelength [19]. To include both the material and modal dispersions, the complex effective index solved from Eq. (2.4) has to be used in the transfer matrix method. The resonance condition occurs when the total round-trip phase condition is satisfied:

$$\Phi(\lambda) = \phi_{DBR}(\lambda) + 2n_{eff,a} k_0 L + \phi_{DBR-Ag}(\lambda) = 2m\pi \tag{2.5}$$

where $\phi_{DBR}(\lambda)$ and $\phi_{DBR\text{-}Ag}(\lambda)$ are the phase of reflection coefficient of the bottom DBR and top hybrid DBR/Ag mirror, respectively; $n_{eff,a}$ is the real part of the averaged effective index in the active region; L is the cavity length; λ is the wavelength; $k_0 = 2\pi/\lambda$ is the wave number in free space; and m is an integer.

For a fixed DBR structure, a strong modal dispersion occurs when the device dimension approaches the wavelength scale. To avoid a large detuning between the peak gain and cavity resonance wavelengths, the stop band of the DBR should be designed to have a reasonable bandwidth. Figure 2.8(a) shows the reflection spectra of the bottom 20.5 DBR pairs as a function of the device diameters. The calculation is based on the HE_{11} mode. The reflection spectra experience a spectral shift toward the shorter wavelength due to the smaller effective refractive index from SiN_x layer and severe modal dispersion at smaller diameters of the

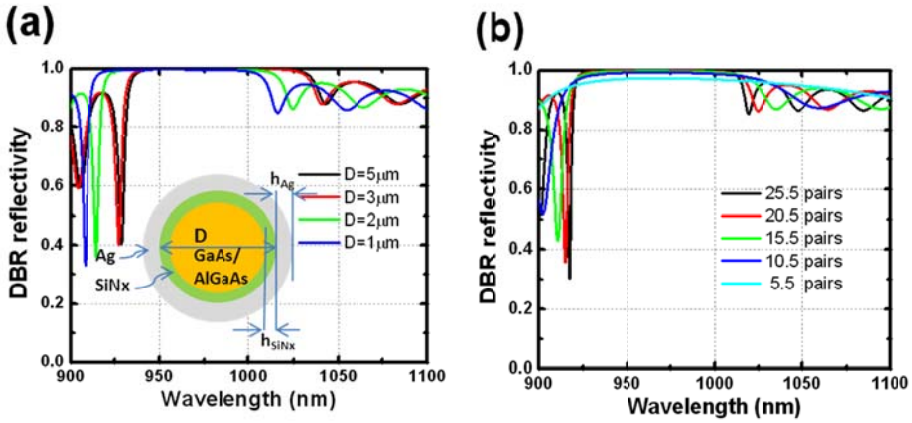

Figure 2.8 (a) Reflection spectra (HE11 mode) of the hybrid 20.5-pairs DBR/silver (35nm) mirror for different device diameters. An clear shift of the stop band occurs for the diameter approaching wavelengths. (b) Reflection spectra (HE11 mode) of the hybrid DBR-metal mirrors of a 2 μm diameter device with different numbers of DBR pairs. A reflectivity of over 99% can be achieved for 10.5 DBR pairs plus silver layer coating.

metal waveguide. Typically, a detuning range of 20-30 nm should be included for red shift arising from current injection heating. The design of the laser around 1.0 μm diameter could still fit the emission spectra of the quantum dots. Figure 2.8(b) shows reflection spectra of the HE_{11} mode for the hybrid mirror of different numbers of DBR pairs for a 2-μm diameter device. The addition of a thin metal (35 nm silver in this case) increases the reflectivity significantly, and, thus, reduces the required number of DBR pairs. Moreover, the application of a hybrid mirror improves the width of the stop band. For example, the stop band increases over 50% for a hybrid 5-pair DBR/metal mirror compared to that of the 20 DBR pairs.

In order to properly include the optical energy associated with dispersive medium with a negative permittivity such as metals, the energy confinement factor which uses electromagnetic energy should be used [19]. The energy confinement factor is defined as:

$$\Gamma_E = \frac{\int_{V_a} \frac{\varepsilon_0}{4} \left\{ \varepsilon_g(\omega, \mathbf{r}) + \mathrm{Re}[\varepsilon(\omega, \mathbf{r})] \right\} |\mathbf{E}(\mathbf{r})|^2 \, d\mathbf{r}}{\int_{V} \frac{\varepsilon_0}{4} \left\{ \varepsilon_g(\omega, \mathbf{r}) + \mathrm{Re}[\varepsilon(\omega, \mathbf{r})] \right\} |\mathbf{E}(\mathbf{r})|^2 \, d\mathbf{r}} \tag{2.6}$$

where **r** is the position vector, V_a is the volume of the active region (three groups of quantum dot stacks in this example) with the subscript *a* representing the active region, $\varepsilon(\omega,\mathbf{r})$ is the relative permittivity, $\varepsilon_g(\omega,\mathbf{r})=\partial \mathrm{Re}[\omega\, \varepsilon(\omega,\mathbf{r})]/\partial\omega$ is the "group permittivity", **E**(**r**) represents the electric field distribution. The threshold material gain (g_{th}) is related to though the following equation,

$$g_{th} = \frac{\omega}{\Gamma_E v_g Q} \tag{2.7}$$

with v_g representing the group velocity and Q as the overall quality factor .

To estimate the number of required DBR pairs for a laser action, the effective threshold material gain of each group (layer) of quantum dots for various numbers of DBR pairs plus 35-nm silver is plotted in Fig. 2.9(a). The threshold material gain decreases dramatically when the number of DBR pairs changes from 5.5 pairs to 10.5 pairs and approaches 1,500 cm^{-1} for larger numbers of DBR pairs. The saturation implies that the major loss comes from the bottom DBR mirror. Decreasing the number of DBR pairs will also improve the energy confinement inside the cavity due to the truncation of the optical field by the highly reflective metal. Figure 2.9(b) shows the wavelength shift and quality factor as a function of the number of DBR pairs. As a result of removing a few pairs of DBR (corresponding to 2mπ round trip-phase), the resonance wavelength has a minimal change. The quality factor decreases significantly when the number of DBR pairs is 5.5.

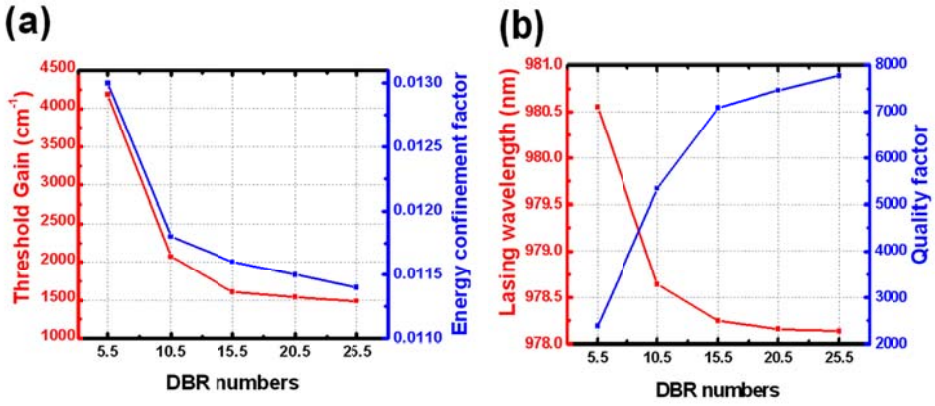

Figure 2.9 (a) Threshold gain and energy confinement factor and (b) quality factor and lasing wavelength changing with DBR numbers of a 2-μm diameter device with hybrid DBR/silver (35 nm) mirrors. The threshold current decreases due to the increase of reflectivity and the energy confinement improves due to the field truncation by metal. The lasing wavelength, however, has a minimal change due to the almost unchanged phase from removing pairs of DBR (except for low numbers 5.5 to 10.5 pairs).

2.3 Device Processing

In this work, we have processed metal cavity surface emitting lasers with various sizes of cavity volume. Figure 2.10 shows the scanning electron microscope (SEM) images of various diameter of QD MCSEL before covering metal. With the contact optical lithography, device diameters of 10, 5, 4, 3, 2, 1.5, and 1 μm are defined.

Before starting any device processing, we have prepared several samples by partially etching away the top DBR pairs to study the cavity reduction in the vertical dimension. Different numbers of top DBR pairs were etched away by inductively coupled plasma reactive-ion etching (ICP-RIE). Etching speed is monitored with the in-situ laser reflectometer in Fig. 2.11 to reach the desired number of remaining DBR pairs. The collimated laser beam is incident from the top reaction chamber window to the sample on the platen. The amplitude of reflected beam is the function of refractive index on the top layer of the sample. In

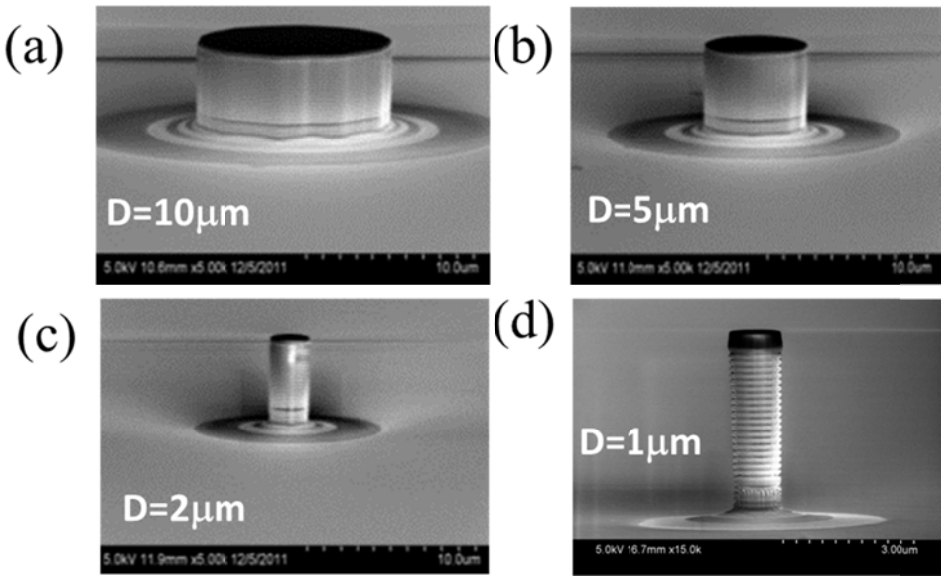

Figure 2.10 Scanning electron microscope (SEM) images of various sizes of QD metal-cavity surface emitting microlasers. The device diameters consist of 10, 5, 4, 3, 2, 1.5, and 1.0 μm.

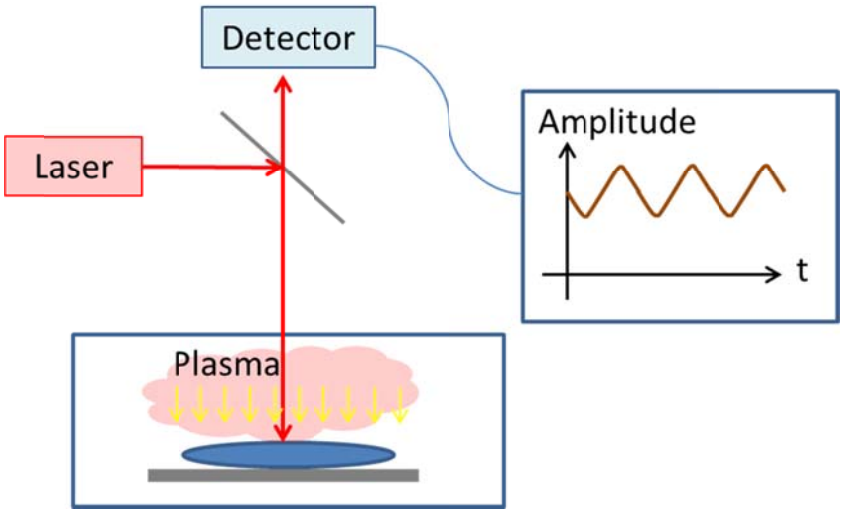

Figure 2.11 Experiment setup of in-situ reflectometer to monitor the etching rate. Collimated laser is incident from the reaction chamber and reflection amplitude is monitored in the time domain. The reflection amplitude oscillates as the refractive index of the top semiconductor layer varies.

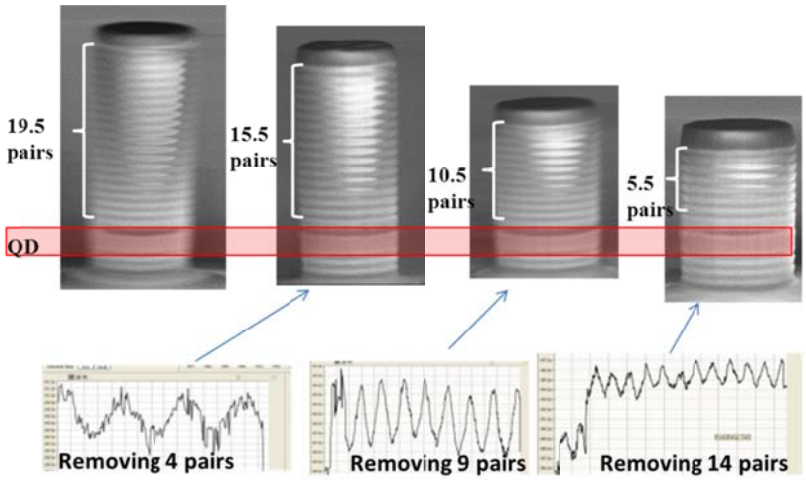

Figure 2.12 SEM images for reduced number of DBR pairs. The top DBR is etched away by in-situ reflectometer before depositing etching mask.

DBR, if the surface is GaAs (high refractive index) the reflected amplitude is considerably stronger than $Al_{0.9}Ga_{0.3}As$ (low refractive index). By monitoring reflected beam in time domain, we can roughly estimate the number of pairs to be etched. The examples of reflectometer for various tall of devices are shown in Fig. 2.12. In this work, we prepared four samples with the final number of the top DBR pairs of 19.5, 15.5, 10.5, and 5.5, respectively. As reported in Section 2.2.3, the top interface has significant impact on the DBR reflectivity, standing-wave phase, and modal confinement factor with the active layer. According to our cavity design in Section 2.2.3, it is necessary to place the metal on the top of the quarter-lambda $Al_{0.9}Ga_{0.3}As$ (low index) layer. Since it is hard to control precise interface from reflectometer, it is simply used to count the number of DBR being etched, and we intentionally stopped etching in the middle of GaAs layer. The precise interface control can be achieved using selective chemical wet etching. The chemical solution of 5:1 citric acid ($C_6H_8O_7$) and hydrogen peroxide (H_2O_2) can be used for high selectivity etching with an etching

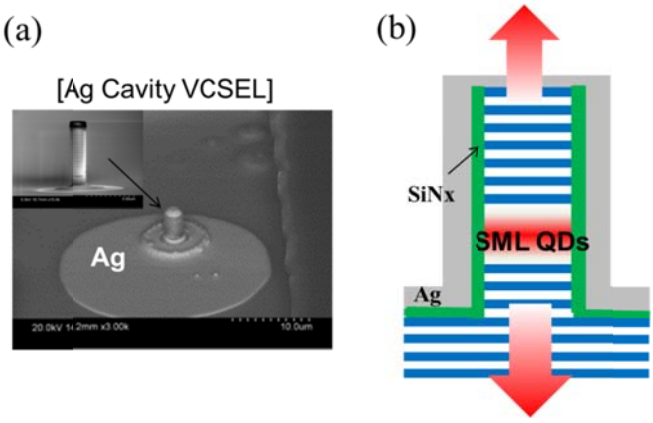

Figure 2.13 (a) SEM images after SiN_x passivation, opening the top current injection window, and conformal silver coverage. (b) Device schematic of the device. The output beam can be collected either from the top side through the silver layer or collect from the substrate.

ratio of approximately 116 between GaAs and $Al_{0.3}Ga_{0.7}As$ [20]. Using this solution in the later processing, the top interface is made exactly to be a layer of $Al_{0.9}Ga_{0.3}As$ (low index).

After samples with different DBR pairs are prepared, a SiN_x layer is deposited by plasma-enhanced chemical vapor deposition (PECVD) for the hard mask to define the micro-post dry-etching. For each sample with a different number of DBR pairs, the micro-posts of various sizes ranging from 1.0 μm to 10 μm were defined by photolithography (Fig. 2.10). The circular cavity was then defined by ICP-RIE with chlorine based reaction gas. To reduce the scattering loss and minimize the mode mismatch, a fine tuning of the reaction mixture was studied to reduce the surface roughness and make the vertical profile. The etching depth of 4 DBR pairs below the active region provides a better carrier and optical confinement. A conformal silicon nitride coating of 200 nm is applied to the sidewall to avoid a short circuit. As shown in Fig. 2.13(b), the top silicon nitride was removed for contact formation by Freon based dry etching. After the top DBR is exposed, a selective wet etching is used to precisely control the interface layer

of DBR with the top silver contact. This wet etching also removes the top surface of the device, which could potentially be damaged from the excessive Freon dry etching. Silver evaporation by e-beam is used to cover the whole structure. The top silver was made thin (~ 35 nm) to allow a reasonable light output. Figure 2.13(a) shows the device after silver coating. In some samples, a back contact is deposited on the substrate and the other samples are flip-chip bonded to gold-plated silicon wafer. On these samples, the GaAs substrate is selectively removed until it reaches bottom part of DBR. Then, the contact metal is deposited with the optical output aperture window pattern.

2.4 Device Performances

2.4.1 Single Mode Lasing

The all devices with various cavity diameters and number of top DBR pairs are characterized. The device is mounted on a copper heat sink to test at different ambient temperatures. A pulsed current source with 10 μA precision was used to drive the devices with continuous wave (CW) and various duty cycles in pulsed mode.

Figure 2.14(a) shows light output vs. current (L-I) curve for CW current injection at room temperature for 10 μm diameter and 19.5-DBR-pairs. The output saturation starts to occur at about twice threshold. This is due to the CW current injection heating, which we discuss in the following section. Figure 2.14(b) is lasing spectrum of the device with bias voltage dependence. Clear single mode lasing has been observed throughout the bias level. The lasing mode shifts toward long wavelength due to thermal heating of the cavity.

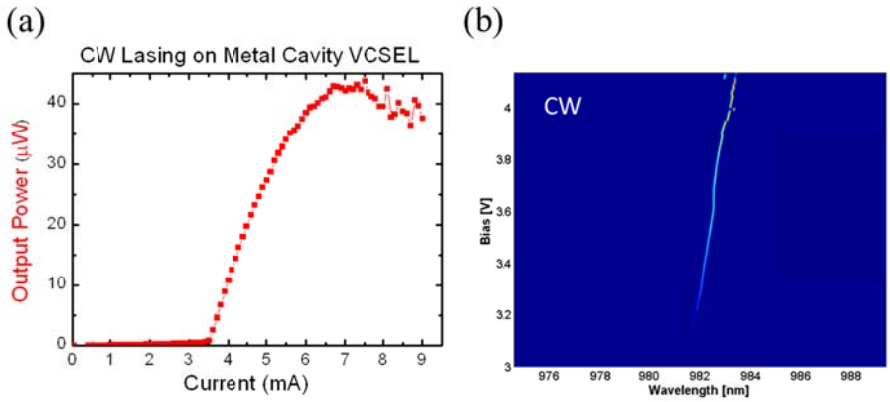

Figure 2.14 (a) Light output vs. current (L-I) for continuous wave (CW) current injection operating at room temperature. (b) Lasing spectrum at each biased voltage. The single mode lasing is observed throughout the bias level.

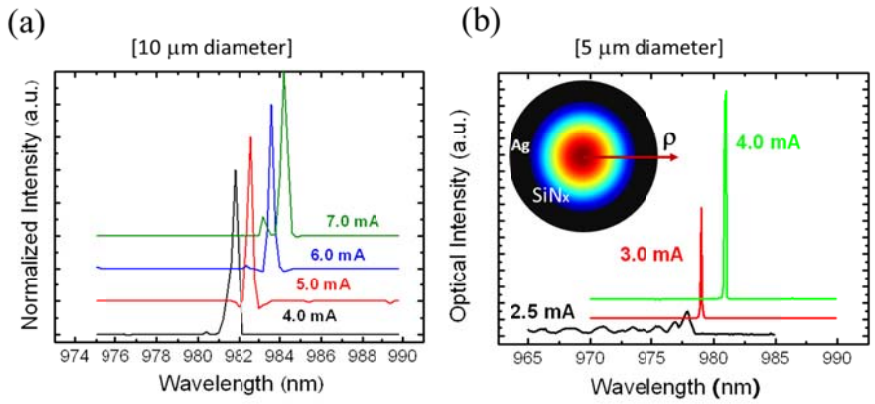

Figure 2.15 (a) Lasing spectrum of 10 μm diameter MCSEL devices and (b) 5 μm devices. The inset shows FEM simulation of cross-sectional view for fundamental HE_{11} mode.

To examine the single mode lasing behavior, the lasing spectrum is compared between different diameters of devices as shown in Fig. 2.15. For the 10-μm device, the lasing spectrum is single mode dominant up until 6.0 mA and the second order mode starts to appear at the shorter wavelength. On the other hand, the 5 μm diameter device demonstrates single mode lasing with full-width half-maximum (FWHM) linewidth less than 0.09 nm. No measurable second mode is observed even at the output saturation injection level. For metal cavity

micro-post, the metal sidewall coating induces the mode dependent propagation loss. The fundamental HE_{11} mode has the lowest loss from metal due to centralized optical field as shown in inset of Fig. 2.15. The higher order mode suffers from higher propagation loss and thus lasing is suppressed.

Another interesting observation is the lasing wavelength for the different diameter of devices. In Fig. 2.15, the lasing wavelength of the 10 μm device around threshold is 982 nm, whereas the 5 μm device starts to lase at about 979 nm. This result is consistent with our analysis. As the diameter of the device becomes smaller, the effective refractive index decreases due to higher field penetration into SiN_x and silver layers. As a result resonant wavelength shifts to the shorter direction.

2.4.2 Thermal Effects

In the previous experimental results, it is seen that thermal rollover occurs at relatively low injection level with CW mode. In this section, the thermal effect of the QD MCSEL device is studied from different duty cycle L-I curves, and cavity mode shifts form ambient temperatures. Then, the cavity temperature of QD MCSEL is estimated at the CW current injection.

Figure 2.16 shows the L-I curves of QD MCSEL at room temperature with different duty cycles. For the 10-μm diameter devices, the light output power is about two orders of magnitude larger than that of the 3-μm diameter devices exceeding over 100 μW before saturation. The threshold current of the 10-μm diameter devices is almost constant independent of the duty cycle. On the other hand, the threshold current of the 3-μm diameter devices increases and the slope

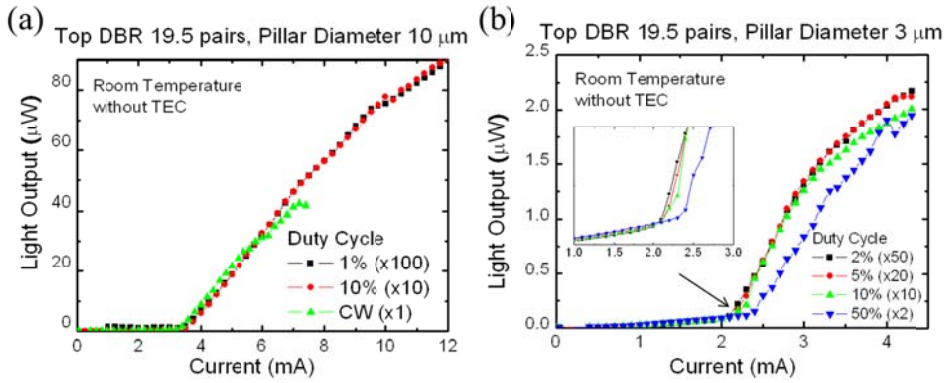

Figure 2.16 (a) L-I curves for different duty cycles for the 10-μm diameter device and (b) the 3-μm diameter device. As the device diameter becomes smaller, the thermal effect becomes more significant.

efficiency drops when the duty cycle exceeds 20%. A similar trend is observed at different diameters. This is due to the fact that self-heating becomes increasingly significant for smaller diameter devices. Among the devices we tested, the smallest laser has a diameter of 1 μm operating with short pulses of 0.1% duty cycle with the output power of the order of a few nW. The self-heating of smaller diameter lasers is mainly attributed to two factors: i) the high series resistance due to the small diameter, and ii) the high current density due to a high threshold gain in small pillar cavity. These two effects are characterized experimentally and explained in Section 2.4.3.

In order to find the actual temperature of the cavity, ambient temperature dependent experiments are conducted. First, the wavelength of the fundamental cavity mode is measured with low injection level at various ambient temperatures. Then, bias dependent lasing wavelengths are measured at room temperature and mapped with wavelength vs. temperature data. Figure 2.17(a) shows the fundamental cavity mode measured at various ambient temperatures around threshold current injection. In order to minimize the cavity heating due to carrier

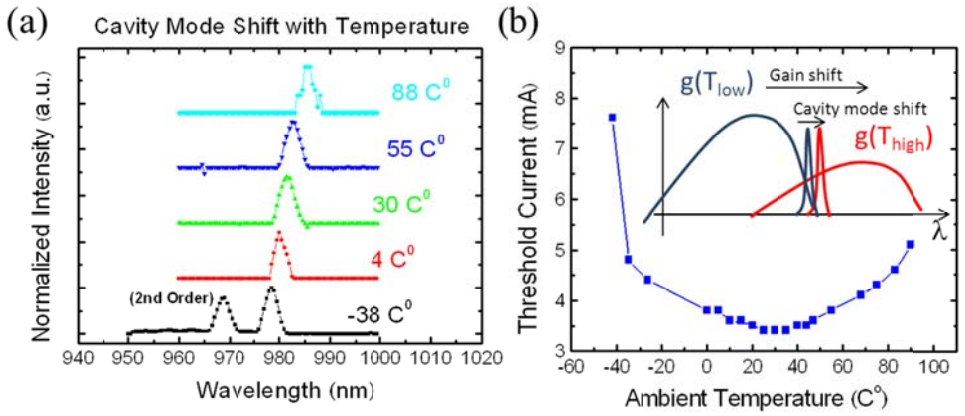

Figure 2.17 Ambient temperature study of metal coated QD MCSEL for (a) fundamental cavity mode with 0.2 % duty cycle current injection around the threshold. (b) Experimentally measured threshold current as a function of ambient temperature. The optimized temperature occurs around 30 ^{o}C.

injection, 0.2 percent duty cycle is injected at around threshold. With this small injection, it is safe to assume that the cavity temperature is the same as the ambient temperature. Similar to conventional VCSELs, both the cavity mode and semiconductor gain spectrum shift toward the long wavelength as temperature increases. However, the rate of shifts of cavity mode and gain are significantly different. The cavity mode is determined by the optical length nL, where n is the refractive index and L is the cavity length. As temperature increases, L increases as a result of thermal expansion of the lattice. In most of semiconductor materials, dn/dT is positive and n increase with temperature as well [21]. Thus, both n and L increase with temperature. The gain peak shifts toward the long wavelength mainly from band gap shrinkage with temperature from lattice constant thermal expansion. The band gap shift with temperature is expressed as

$$E_g(T) = E_g(0) - \frac{\alpha T^2}{\beta + T} \tag{2.8}$$

where $E_g(0)$ is band gap at 0 K and empirical fitting parameters α and β for GaAs are 5.58 x 10^{-4} eV/K and 220 K, respectively [22]. Along with the shift of the gain peak, the gain amplitude also decreases with temperature. The band gap shifts with temperature much faster than the cavity mode as shown in the inset of Fig. 2.17(b). From the experimental data in Fig. 2.17(a), a linear approximation gives cavity mode shift as 0.065 nm/K. At -38 ^{o}C the second order mode is observed because the gain peak is located at shorter wavelength. Even though optical gain is high at low temperature, the gain and cavity mode do not overlap well and threshold current is high as shown in Fig. 2.17(b). As the temperature increases, the threshold current decreases because of the better overlap of the gain spectrum with the cavity mode. The optimal temperature for minimum threshold for this QD MCSEL is around 30 ^{o}C. As temperature increases further, threshold starts to increase again from gain reduction and gain peak shifts to longer wavelengths than the cavity mode.

Using the fundamental cavity mode shift with temperature, the cavity temperature at each CW injection level is calculated and plotted in Fig. 2.18 (right axis). On the same plot, total electrical injection power (product of current and voltage) is plotted. Due to the relatively low electrical to optical conversion efficiency of the QD MCSEL device, the injected power and cavity temperature have a similar trend.

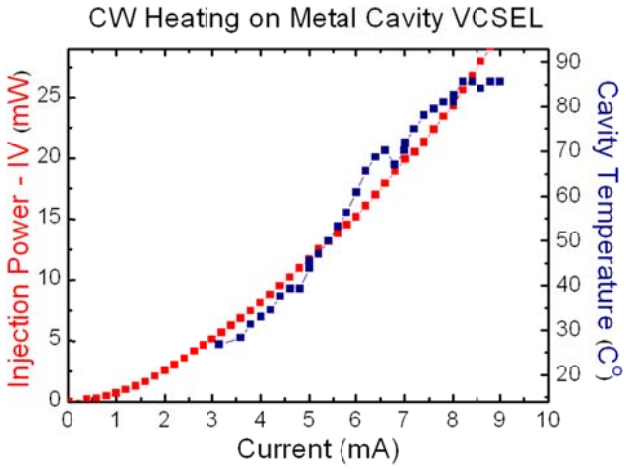

Figure 2.18 Cavity temperature of CW injected MCSEL is extracted experimentally from the lasing wavelength shift (right). The trend is compared with the total injected power into the device (left).

2.4.3 Cavity Volume Scaling Law

In this section, we focus on the scaling law of the laser performance with the cavity volume. Among all the fabricated devices, the yield of lasing devices becomes smaller as the diameter of the micropost and the number of DBR pairs are reduced. With 19.5 DBR pairs, the smallest 1.0-μm diameter lasers still operate with 0.1 % duty cycle at room temperature as shown in Fig. 2.19. With a reduced number of DBR pairs, the minimum diameter of lasing devices increase to 3.0-μm with 15.5-DBR-pairs, and 4.0-μm with 10.5-DBR-pair. As seen from the transfer matrix method analytical study in Section 2.2.4, the DBR reduction from 10.5 pairs to 5.5 pair significantly increases the threshold. A few devices with 10 μm diameter are lasing. The cavity mode around threshold is shown in Fig. 2.19(b) with FWHM linewidth of 0.154 nm. Although this is much larger than 19.5-DBR-pair devices (0.06 nm with monochromator resolution limit), the quality factor is large enough for lasing.

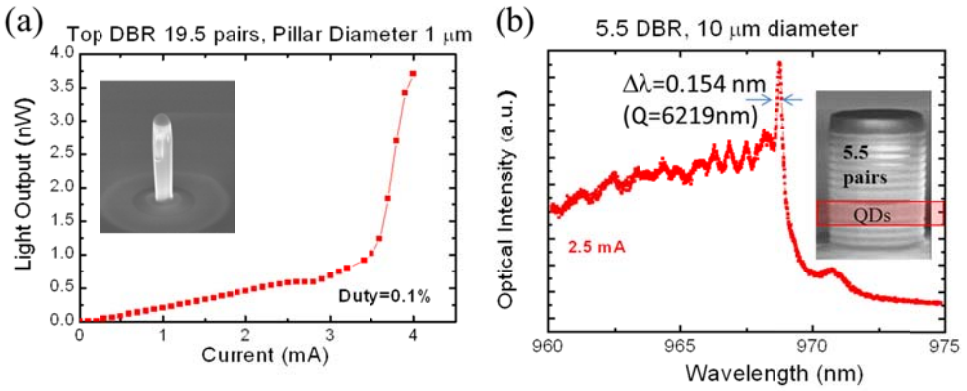

Figure 2.19 (a) The L-I curve of the smallest 1.0-μm diameter device lasing with 0.1 % duty cycle. The inset shows SEM image of the device. (b) The spectrum of 5.5 pair DBR device around threshold.

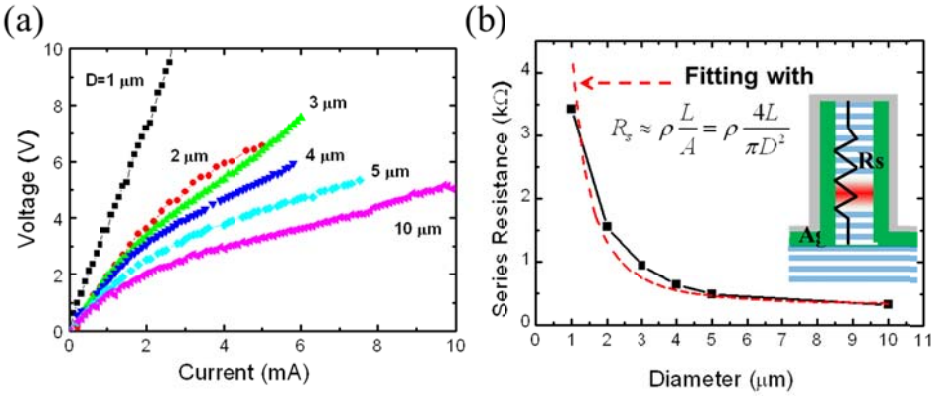

Figure 2.20 (a) Voltage vs. current (IV) curve for different diameter of devices. Large device shows diode curves, but small diameter device is dominated by series resistance. (b) The series resistance extracted from IV curve. The dashed line is fitting with register model for different diameter.

Figure 2.20(a) shows current vs. voltage (I-V) curves of the QD MCSEL devices for different diameters. For the 10-μm diameter devices, the I-V curve shows a typical diode behavior with decreased resistance after turn-on voltage. As the diameter of the devices becomes smaller, the I-V curve becomes more like a resistor. The significant part of high resistance is from the series resistance

through the small diameter post of DBR cavity. The simplest model of series resistance is expressed as

$$R_s \approx \rho \frac{L}{A} = \rho \frac{4L}{\pi D^2} \tag{2.9}$$

where ρ is resistivity, L is electron traveling length, and A is cross-sectional area. Even though this simple model is for linear homogeneous material, the approximation works well with small DBR p-i-n junction in our device due to series-resistance dominant electrical characteristics. The resistance increases approximately proportional to the inverse of the square of the diameter and is proportional to the length of the pillar. Figure 2.20(b) shows series resistance extracted from the experimental data in Fig. 2.20(a). The dashed curve shows series resistance model in Eq. (2.9) with post length L and diameter D measured from SEM. From the fitting, the effective resistivity of DBR is extracted to 7.48 x 10^{-2} Ωcm. With bulk p-GaAs material, this resistivity corresponds to N_A = 3 x 10^{17} cm^{-3}, which is close to the doping level in our design.

Figure 2.21 shows the threshold current density as a function of device cavity diameters for different numbers of the top DBR pairs. In order to obtain reliable data, we measured over 37 lasers with multiple devices for each cavity size located at different positions on the chip. Even though there are small differences from one device to another in the threshold current densities, most devices with the same cavity size fall in the same proximity of values. The line in the figure connects the average value of threshold current density for each cavity size. The threshold current density increases almost exponentially as the diameter of the cavity is reduced. For our smallest 1-μm diameter device with 19.5 DBR pairs, the threshold current density is 445 kA/cm^2 with 0.1% pulse injection (not shown in

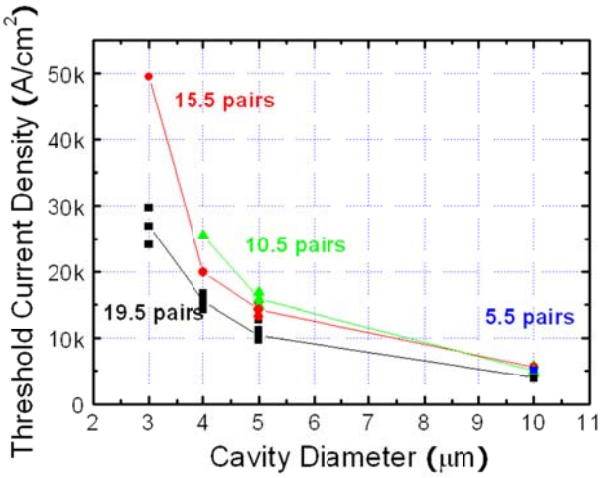

Figure 2.21 Threshold current density as a function of cavity diameter for different numbers of top DBR pairs. For each cavity size, multiple devices are tested and plotted as dots. The line is connecting the average values of each size.

figure). For reduced numbers of DBR pairs, the threshold current decreases in different degrees for each diameter devices. In the 10-μm diameter devices, the threshold current densities vary only a little. For the smaller diameter devices, the threshold current increases more dramatically by reducing the number of DBR pairs. This result is not predicted from the study in Section 2.2.4 because we separated the problem into horizontal effective index calculation and vertical mode propagation from transfer matrix method.

From our transfer matrix method results in Fig. 2.9(a), the threshold gain increases rapidly from 10.5 pairs to 5.5 pairs. Even though a few devices of 5.5 DBR pairs are lasing at room temperature, device yield is smaller than larger number pairs. This is probably due to the deviation between the ideal device structure in the model and actual device structure after processing. As is pointed out in the Section 2.2.3, the precise top interface is very important for standing-wave phase design when the number of DBR pairs is small and metal is

placed on the top. In reality, $Al_{0.9}Ga_{0.3}As$/GaAs interface is linearly graded and selective chemical etching cannot stop at the exact thickness.

2.5 Summary

We have designed, fabricated, and characterized MCSELs with SML QDs in the active region. The QD active layer is expected to reduce the surface recombination rate which is severe when the micro-post diameter becomes small. Different sizes of metal-DBR cavities are fabricated both in the lateral and vertical dimensions following our theoretical design rules to optimize toward a small threshold gain for room temperature operation. Unlike the conventional air interface VCSELs, the metal-semiconductor interface design is important, especially for devices with a reduced number of DBR pairs toward the goal of nanolasers. From our theoretical model using the transfer matrix method, we estimated that lasers using hybrid DBR-metal mirrors with 5.5 and 10.5 DBR pairs operating CW at room temperature are achievable with the 2-μm diameter devices. Among the various sizes of metal-cavity volumes, a few of the smallest devices are 1-μm in diameter with 19.5 top-DBR-pairs lasing in 0.1% pulsed mode, and 5.5 top-DBR-pairs large device can lase with CW both at room temperature. The thermal effects of cavity heating are examined, and it is found that cavity temperature reaches around $80^{o}C$ with high injection. This result raises a question about the effective heat removal from active layer through the metal cavity. Since most effective heat transfer in the crystal is done through photon propagation, etching the micro-post by etching the single crystal bond may prevent the effective photon transfer at the interfaces of semiconductor/SiN_x/Ag.

From the analysis of various sizes of diameter devices, it is found that self-heating is significant in the smaller diameter devices due to both the higher series resistance and higher threshold gain leading to high carrier density. Self-heating causes the decrease of optical gain as well as the shift of the resonant wavelength. The emission spectrum shows a clear single mode lasing.

In conclusion, one of the smallest electrical injection lasers is demonstrated with a minimum diameter of 1-μm and a minimum DBR-Ag hybrid mirror of only 5.5 pairs. However, further reduction of the diameter with a tall post encounters significant problems with high series resistance, which causes severe thermal generation. On the other hand, further reduction of DBR is also challenging because the top interface of only a few DBR with metal perturbs the resonant standing-wave phase reducing the reflectivity, shifting the gain overlap. To solve these problems, we work on the metal-encapsulated micro- and nanocavity lasers without DBR pairs in the next chapter.

2.6 References

[1] H. Soda, K. Iga, C. Kitahara, and Y. Suematsu, "GaInAsP/InP surface emitting injection lasers," *Jpn. J. Appl. Phys*., vol. 18, pp. 2329-2330, 1979.

[2] D. G. Deppe, D. L. Huffaker, J. Shin, and Q. Deng, "Very-low-threshold index-confined planar microcavity lasers," *IEEE Photon. Tech. Lett*., vol. 7, no. 9, pp. 965-967, 1995.

[3] C. Y. Lu, S. W. Chang, S. L. Chuang, T. D. Germann, and D. Bimberg, "Metal-cavity surface-emitting microlaser at room temperature," *Appl. Phys. Lett*., vol. 96, no. 25, p. 251101, 2010.

[4] C. Y. Lu, S. W. Chang, S. L. Chuang, T. D. Germann, U. W. Pohl, and D. Bimberg, "CW substrate-free metal-cavity surface microemitters at 300 K," *Semicond. Sci. Technol*., vol. 26, no. 1, pp. 014012-014018, 2011.

[5] C. Y. Lu, S. W. Chang, S. L. Chuang, T. D. Germann, U. W. Pohl, and D.

Bimberg, “Low thermal impedance of substrate-free metal cavity surface-emitting microlasers,” *IEEE Photonics Technol. Lett*., vol. 23, no. 15, pp. 1031-1033, 2011.

[6] C. Y. Lu, S. L. Chuang, A. Mutig, and D. Bimberg, “Metal-cavity surface-emitting microlaser with hybrid metal-DBR reflectors,” *Opt. Lett*., vol. 36, no. 13, pp. 2447-2449, 2011.

[7] F. Hopfer, A. Mutig, M. Kuntz, G. Fiol, D. Bimberg, N. N. Ledentsov, S. S. Mikhrin, D. A. Livshits, I. L. Krestnikov, A. R. Kovsh, N. D. Zakhorov, and P. Werner, “Single-mode submonolayer quantum-dot vertical-cavity surface-emitting lasers with high modulation bandwidth,” *Appl. Phys. Lett*., vol. 89, p. 141106, 2006.

[8] A. Lenz, H. Eisele, J. Becker, J.-H. Schulze, T. D. Germann, F. Luckert, K. Potschke, E. Lenz, L. Ivanova, A. Strittmatter, D. Bimberg, U. W. Pohl, and M. Dahne, “Atomic structure and optical properties of InAs submonolayer depositions in GaAs,” *J. Vac. Sci. Technol. B*, vol. 29, p. 04D104, 2011.

[9] F. Hopfer, A. Mutig, G. Fiol, M. Kuntz, V. A. Shchukin, V. A. Haisler, T. Warming, E. Stock, S. S. Mikhrin, I. L. Krestnikov, D. A. Livshits, A. R. Kovsh, C. Bornholdt, A. Lenz, H. Eisele, M. Dahne, N. N. Ledentsov, and D. Bimberg, “20 Gb/s 85°C Error-Free Operation of VCSELs Based on Submonolayer Deposition of Quantum Dots,” *IEEE J. Sel. Top. Quantum Electron.*, vol. 13, pp. 1302-1308, 2007.

[10] Y. Arakawa and H. Sasaki, “Multidimensional quantum well laser and temperature dependence of its threshold current,” *Appl. Phys. Lett*., vol. 40, pp. 939-941, 1982.

[11] A. R. Kovsh, N. A. Maleev, A. E. Zhukov, S. S. Mikhrin, A. P. Vasil’ev, Y. M. Shernyakov, M. V. Maximov, D. A. Livshits, V. M. Ustinov, Z. I. Alferov, N. N. Ledentsov, and D. Bimberg, “InAs/InGaAs/GaAs quantum dot lasers of 1.3 μm range with high (88%) differential efficiency,” *Electron. Lett*., vol. 38, pp. 1104-1106, 2002.

[12] D. Bimberg, and N. Ledentsov, “Quantum dots: lasers and amplifiers,” *J. Phys.: Condens. Matter,* vol. 15, p. R1063, 2003.

[13] S. Fathpour, Z. Mi, and P. Bhattacharya, “High-speed quantum dot lasers,” *J. Phys. D*, vol. 38, pp. 2103-2111, 2005.

[14] M. Ishida, M. Sugawara, T. Yamamoto, N. Hatori, H. Ebe, Y. Nakata, and Y. Arakawa, “Theoretical study on high-speed modulation of Fabry-Pérot

and distributed-feedback quantum-dot lasers: K-factor-limited bandwidth and 10 Gbit/s eye diagrams," *J. Appl. Phys*. vol. 101, p. 13108, 2007.

[15] S. Fathpour, Z. Mi, and P. Bhattacharya, "The role of Auger recombination in the temperature-dependent output characteristics ($T_0=\infty$) of p-doped 1.3 μ m quantum dot lasers," *Appl. Phys. Lett*., vol. 85, pp.5164-5166 2004.

[16] T. J. Badcock, R. J. Royce, D. J. Mowbray, M. S. Skolnick, H. Y. Liu, M. Hopkinson, K. M. Groom, and Q. Jiang, "Low threshold current density and negative characteristic temperature 1.3 μm InAs self-assembled quantum dot lasers," *Appl. Phys. Lett.*, vol. 90, p. 111102, 2007.

[17] S. L. Chuang, "Physics of photonic devices," 2nd edition, Chapter 5, New York: Wiley, 2009

[18] A. Haglund, J. S. Gustavsson, J. Vukusic, P. Modh, A. Larsson, "Single fundamental-mode output power exceeding 6 mW from VCSELs with a shallow surface relief," *IEEE Photon. Tech. Lett*., vol. 16, no. 2, pp. 368-370, 2004.

[19] S. W. Chang and S. L. Chuang, "Fundamental formulation for plasmonic nanolasers," *IEEE J. Quantum Electron.*, vol. 45, no. 8, pp.1014-1023, 2009.

[20] G. C. DeSalvo, W. F. Tseng, and J. Comas, "Etch rates and selectivities of citric acid/hydrogen peroxide on GaAs, $Al_{0.3}Ga_{0.7}As$, $In_{0.2}Ga_{0.8}As$, $In_{0.53}Ga_{0.47}As$, $In_{0.52}Al_{0.48}As$, and InP," *J. Electrochem. Soc*., vol. 139, no. 3, pp. 831-835, 1992.

[21] M. Bertolotti, V. Bogdanov, A. Ferrari, A. Jascow, N. Nazorova, A. Pikhtin, and L. Schirone, "Temperature dependence of the refractive index in semiconductors," *J. Opt. Soc. Am. B*, vol. 7, no. 6, pp. 918-922, 1990.

[22] P. Wang, S. Holmes, T. Le, R. Stradling, I. Ferguson, and A. de Oliveira, "Electrical and Magneto-Optical Studies of MBE InAs on GaAs," *Semicond.Sci.Technol*., vol. 7, pp. 767-786, 1992.

CHAPTER 3

METAL-ENCAPSULATED NANOCAVITY LIGHT EMITTERS

3.1 Introduction

In Chapter 2, metal-cavity surface emitting microlasers based on lateral confinement by metal and vertical confinement by hybrid DBR-metal mirrors have been discussed. One of the smallest electrical injection lasers is demonstrated with a diameter of 1 μm and a top hybrid mirror of 5.5 DBR pairs. However, the relatively tall post structure has a significant series resistance when the device diameter approaches 1.0 μm, which generates a large amount of heat corresponding to $P_{heat}=R_sI^2$. On the other hand, further reduction of the DBR pairs has its own challenges because the top interface of a few DBR pairs with metal coating perturbs the resonant standing-wave phase, reduces the reflectivity, and shifts the gain peak overlap with the longitudinal standing-wave pattern. This chapter discusses metal-encapsulated nanocavities for size reduction. In metal-encapsulated lasers, the series resistance is reduced by the shorter carrier traveling length L without a discontinuous energy band of DBR pairs. The broadband mirror reflector is less sensitive to the vertical thickness design because the resonant wavelength can be self-adjusted within the relatively broad semiconductor gain. The real challenges of these devices are fighting with the radiation loss due to small cavity and ohmic metal loss at room temperature.

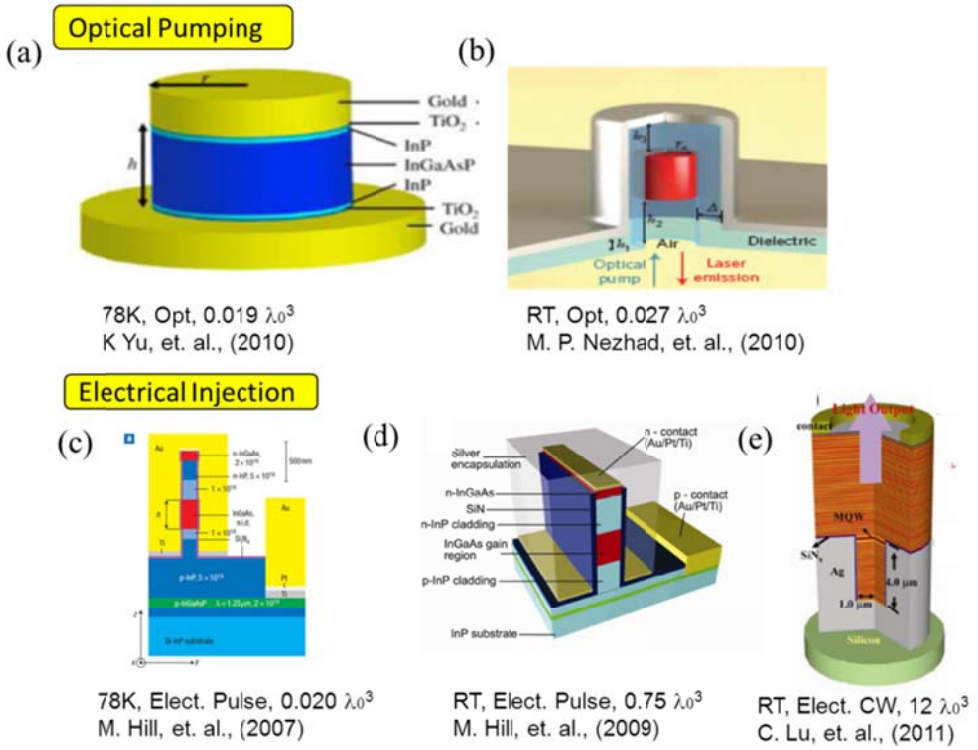

Figure 3.1 The state of the art metal cavity nanolasers. (a) Optical pumping at low temperature with gold on top and bottom [1]. (b) Optical pumping laser at room temperature [2]. (c) Gold finger metal laser with pulsed electrical injection at low temperature [3]. (d) Electrical injection Fabry-Perot type nanolaser at room temperature [4]. (e) DBR-metal hybrid metal coated surface emitting laser with CW electrical injection at room temperature [5].

Fabrication of the metal-encapsulated cavities without electrical shorting also becomes more difficult.

Figure 3.1 shows some of the state-of-the-art nanolasers using a metal cavity. One of the biggest challenges of metal cavity nanolasers is how to minimize the threshold gain of the cavity. One approach is to use optical pumping for population inversion in the gain medium. Unlike the current injection, optical pumping can generate electron and hole pairs slightly above the band edge without generating much heat. Without a current bias, it can suppress ohmic heat generation and hot carriers under the biased field. The device fabrication becomes much easier for optical pumping without consideration of electrical isolation

between the anode and the cathode and the p-i-n junction doping design. The second major approach is cooling the ambient temperature low enough so that the semiconductor gain becomes high and metal loss is reduced. Most of the smallest metal cavity lasers are demonstrated by either or both approaches as shown in Fig. 3.1(a), (b), and (c). Recently, Hill et al. [4] successfully demonstrated Fabry-Perot type sub-wavelength plasmonic waveguide lasers with pulsed electrical injection at room temperature. In this cavity, the lasing mode is confined in a relatively long cavity in one dimension with the sub-wavelength width. Due to lateral optical confinement, the active gain layer and standing-wave overlap can be increased compared with the gold finger nanolaser in Fig. 3.1(c). One of the drawbacks is the optical output coupling. Due to the thick silver coverage in the sidewall, the optical output is collected from the bottom substrate, which is not along the dominant Poyinting's vector direction. Therefore, it is difficult to collect the light output.

For practical applications, we design our metallic nanocavity lasers with the current injection configuration with the cavity resonance wavelength designed at room temperature. Unlike the state-of-the-art lasers in Fig. 3.1, semiconductor cavities are encapsulated by a metal in all three directions. The cavity dimension is designed such that the fundamental HE_{11} mode propagates along the vertical direction for various radius devices. In this way, the devices emit the light output through the top thin metal with a good beam profile. In the following sections, the device design for the optical cavity and electrical doping are calculated and simulated with numerical methods. The detailed device processing recipes are presented, and our fabricated device performances are presented.

3.2 Cavity Design and Simulation

3.2.1 Metal-Encapsulated Cavity Structure

The schematic diagram of metal-encapsulated nanocavity is shown in Fig. 3.2. In previously reported nanolasers, semiconductor cavities are not covered by metal in all directions due to an optical pumping configuration [1-2, 6] or substrate retaining on electrical injection devices [3-4]. In our devices, the original InP substrate is removed, the semiconductor p-i-n junction (p-InP/InGaAs/n-InP) is encapsulated by metal in all directions, and the device is flip-chip bonded to a silicon handling wafer. The typical material gain of a bulk InGaAs semiconductor is of the order or 2000 ~ 3000 cm^{-1} at room temperature. Using a short cavity with a few standing-wave nodes, the high modal overlap with the gain material in bulk is more advantageous than that of QWs or QDs for a higher optical confinement factor [1-4, 6]. The bulk gain is also less sensitive to small resonant wavelength and phase shift arising from the processing discrepancies between the ideal design structure and the real fabricated devices. From the previous studies of the metal coated lasers, silver has a good thermal conductivity, and removes heat from the current injection region quickly compared with air or BCB dielectric coating. This significantly reduces the threshold current at high temperature operation [7]. The optical output is collected from the top surface of the device through the thin gold or silver cap. The active InGaAs bulk material is designed for 1550 to 1600 nm photoluminescence peak emission grown by either metal organic chemical vapor deposition (MOCVD) or molecular beam epitaxy (MBE). The p-side and n-side contacts are isolated by approximately 100 to 200 nm thick silicon nitride layers. which also serve as sidewall passivation and optical

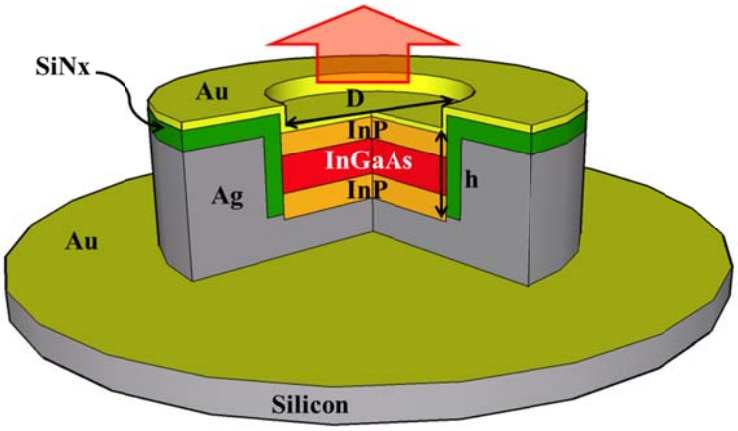

Figure 3.2 The device schematic of the metal-encapsulated nanolasers. The semiconductor p-i-n hetero-junction is covered by metal in all directions. The bottom and sidewall are covered with a thick silver and the top surface is covered by a thin silver or gold to couple the output from the cavity.

cladding in the cavity.

The radius of our fabricated semiconductor disks ranges from 750 nm to 5 μm and the thickness of p-i-n junction has a few designs with 200, 885, and 1599 nm, depending on the cavity modes. The corresponding smallest cavity volume is 0.23 μm^3 or 0.061 λ_0^3 in term of the free space emission wavelength.

3.2.2 Threshold Condition of Metal Cavity Nanolasers

Before discussing the cavity design of metallic nanolaser, let us start with the basic threshold condition of the Fabry-Perot lasers.

$$\Gamma g_{th} = \alpha_i + \frac{1}{2L}\ln\left(\frac{1}{R_1 R_2}\right) \tag{3.1}$$

The left side is the threshold modal gain with Γ as the optical confinement factor, and g_{th} as the required material gain to reach the threshold condition. The right side is the loss in the cavity with α_i as the intrinsic modal loss and the second term the mirror radiation loss (due to transmission output of the cavity), where L is the

longitudinal cavity length, and R_i is the power reflectivity of the i-th side of the mirror. Even though this equation is typically used for a long cavity, it still works well for metal cavity micro- and nanolasers as long as we take into account the modal loss, reflectivity, and the resonance wavelength properly for the lasing guided mode for the designed multi-layered cylindrical cavity structure. This is discussed more in Section 3.2.4. One of the biggest challenges of nanolasers is how to suppress the radiation loss for a small L in Eq. (3.1). For example, L = 300 μm of a stripe as-cleaved Fabry-Perot laser has a mirror loss about 40 cm^{-1}. In order to achieve the same magnitude of loss with L = 1 μm, the optical power reflectivity R needs to be 0.996. The first term α_i on the right-hand side also increases as the lateral dimension shrinks due to the metallic loss. Fortunately, the intrinsic loss α_i is not dominant unless the lateral dimension becomes sub-wavelength scale. It is usually of an order of tens of cm^{-1} for a 500-nm radius device with silver coating. To increase the modal gain for a small cavity, bulk gain is used. An alternative expression for the threshold condition is

$$\Gamma_E g_{th} = \frac{\omega}{v_g Q} = \frac{1}{v_g \tau_p} \tag{3.2}$$

where ω is the angular frequency, v_g is the group velocity, Q is the quality factor of the cavity, and τ_p is the photon lifetime. Again, the left side of equation shows the modal gain. For plasmonic metal nanolasers, the optical energy confinement factor Γ_E has to be used instead of the power confinement factor due to the negative and dispersive nature of the permittivity in metal plasmas [8]. Since ω and v_g cannot be engineered much for a given material, it is desired to increase Q (or photon lifetime τ_p) as much as possible. The quality factor Q is defined as the ratio of energy stored in the cavity to energy dissipation (including radiation loss)

per optical cycle. It can be decomposed to

$$\frac{1}{Q} = \frac{1}{Q_{mat}} + \frac{1}{Q_{rad}} \tag{3.3}$$

where Q_{mat} is related to the energy dissipation due to material loss and Q_{rad} is related to the photon escape from the cavity. In metal-encapsulated nanolasers with the bottom and sidewall covered with a thick metal, Q_{rad} is the inverse of the output photon emission ratio from the top and Q_{mat} is dominated by optical loss by the metal in all directions. At room temperature, the Q factor of a few hundreds is required for realizable threshold gain.

3.2.3 Metal Properties at Near Infrared

For a perfect electrical conductor (PEC), there is no optical loss and the reflectivity is unity. In real metals, there is a finite resistivity causing ohmic loss and the reflection coefficient is always less than unity and the phase deviates from π. As we discussed in the previous section, the important parameter for metal nanocavity is a high reflectivity R for a small radiation loss.

Table 3.1 summarizes important optical parameters for various metals at 1.55 μm wavelength from the literature. Various metals are sorted in the order of optical power reflectivity for a plane wave incident from InP layer to an infinitely thick metal. The highest reflectivity is achieved by Ag or Au depending on the literature, then followed by Cu and Al at 1.55 μm. Notice that these metals have a large absorption coefficient due to the large imaginary part of the refractive index. However, since the real part of the refractive index is small compared with those of semiconductors, a smaller fraction of the incident field is transmitted into the metal. Some metals such as Ni, W, Pt, and Ti have a small reflectivity because the

Table 3.1 Important parameters of various metals at 1.55-μm wavelength

	Re[n]	Im[n]	Bulk α (cm^{-1})	R from InP to thick metal	Power Loss with thick metal	$\Delta\Phi$ from vacuum (degrees)
PEC	0	∞	∞	1.000	0	-180
Ag [9]	0.14	11.37	9.21E+05	0.987	0.013	-169.946
Au [10]	0.55	11.50	9.32E+05	0.952	0.048	-170.083
Ag [10]	0.51	10.80	8.76E+05	0.950	0.050	-169.443
Au [9]	0.52	10.74	8.71E+05	0.949	0.051	-169.388
Cu [9]	0.72	10.66	8.64E+05	0.929	0.071	-169.324
Al [11]	1.58	15.66	1.27E+06	0.925	0.075	-172.765
Cu [10]	0.61	8.92	7.23E+05	0.918	0.082	-167.264
Ta [12]	0.87	8.51	6.90E+05	0.875	0.125	-166.739
Pd [12]	2.95	8.33	6.76E+05	0.650	0.350	-167.807
Ni [10]	3.38	6.82	5.53E+05	0.521	0.479	-166.528
W [10]	2.22	4.85	3.93E+05	0.465	0.535	-160.539
Pt [10]	5.31	7.04	5.71E+05	0.446	0.554	-169.606
Ti*[12]	3.62	3.52	2.85E+05	0.215	0.785	-163.965

*Ti parameters are at 1.24 μm wavelength

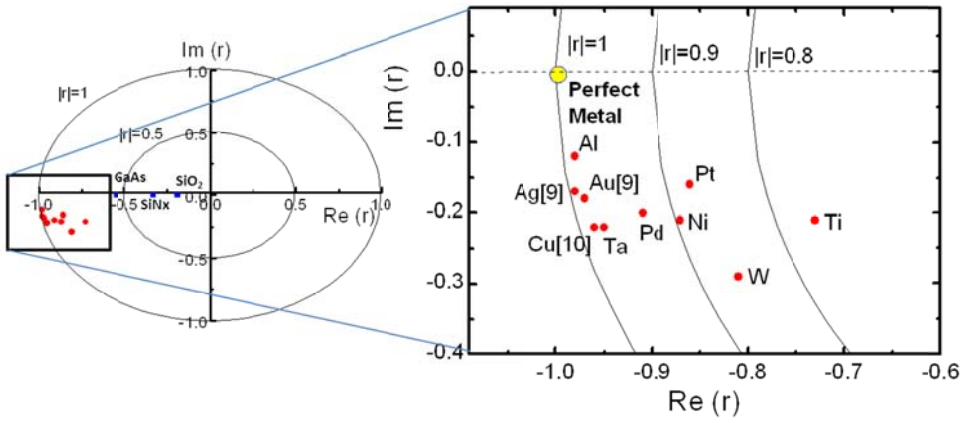

Figure 3.3 The complex field reflection coefficients (r) of various metals are plotted in the complex plane together with a few dielectric materials. The reflection coefficient is calculated for a plane wave incident from vacuum to an infinitely thick metal or dielectric layer using the optical parameters in Table 3.1.

real part of the refractive index is close to that of the semiconductor. As a result, a large fraction of the optical field is transmitted to the metals and absorbed.

To compare with reflection property of the metals with a PEC, the complex reflection coefficient *r* of the optical field is plotted in the complex plane in Fig. 3.3. The reflection coefficient is calculated for a plane wave normally incident from vacuum to an infinitely thick metal using the optical parameters in Table 3.1. The distance from the origin expresses the magnitude of the reflection coefficient and the angle from the positive x-axis represents the phase shift of the reflected wave from the normal incident wave. A PEC has a unity magnitude and a phase shift of π. Among various metals, Al has the closest point to PEC because the reflection phase shift is close to π among all metals here. In the later section, this non-ideal phase shift is taken into account to calculate the resonant condition in the metal cavity.

From the magnitude of the power reflection between InP and a thick metal, Ag or Au is the best choice to form a low loss cavity at 1.55 μm. In the following section, we used Ag for most of our designs and fabrications. After fabrication of the first device, we have found that a thin Ag layer is easier to oxidize or bind with sulfide atoms to form Ag_2O or Ag_2S at elevated temperature, which degrades the optical properties as well as electrical conduction. For this reason, a thick Ag is used for the sidewall and bottom mirrors, but a thin top mirror is covered with Au as shown in Fig. 3.1.

3.2.4 Cavity Design for Optical Resonance

For nanocavities with a size approaching the order of a wavelength, a careful design of the cavity dimension is critical so that the target resonant wavelength

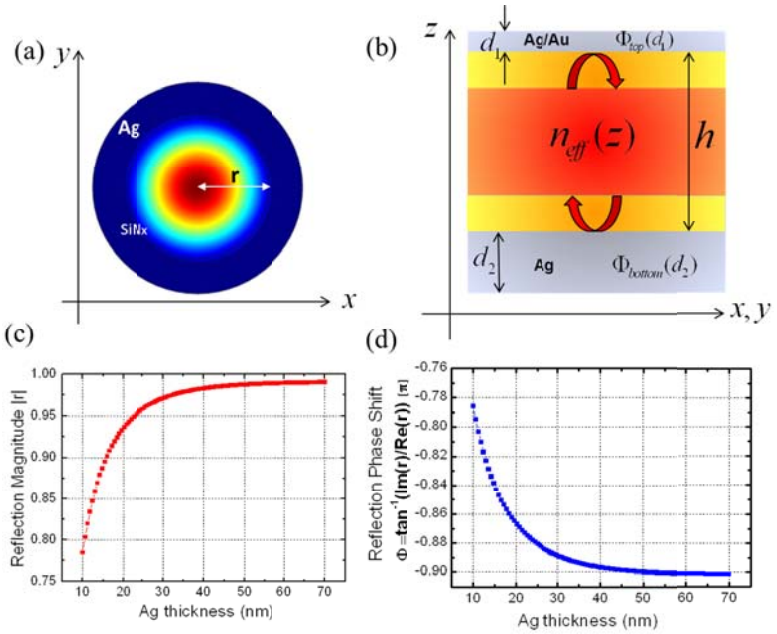

Figure 3.4 (a) Top cross sectional view (horizontal cut) of the device with the fundamental HE_{11} mode simulated from the FEM method. (b) Side cross sectional view (vertical cut) of the device to design the thickness for the round trip resonance phase condition. (c) Magnitude of the optical field reflectivity |r| of silver as a function of the silver thickness. (d) The phase shift of a normally incident optical field from the semiconductor/Ag/air interface as a function of the silver thickness.

falls within the semiconductor gain spectral width. This is different from conventional DFB lasers because the resonant wavelength can be determined from the stop band of the periodic dielectric mirrors. In our work, we choose the HE_{11x} fundamental mode because it has the best transverse optical confinement factor as well as an excellent beam shape and optical output coupling for surface emission.

Figure 3.4 shows the fundamental rule to design the cavity dimension such that the resonant wavelength overlaps with semiconductor gain bandwidth. The general approach is the same as the metal-cavity surface emitting microlasers explained in Chapter 2. The three-dimensional problem is decomposed to a waveguide program as shown in the cross-section in Fig. 3.4(a) for each vertical z position. We calculated the effective refractive index (n_{eff}) of the fundamental

HE_{11} mode from the finite-element method (FEM), which includes the ohmic loss, material dispersion, and waveguide dispersion from the metal layer. As the radius of the device shrinks, n_{eff} decreases because more optical mode overlaps with the SiN_x layer and the imaginary part of n_{eff} increases due to more ohmic loss from the metal. Next, we designed the top and bottom silver thickness. The top silver thickness is carefully designed for optimizing between output light transmission and the cavity quality factor from Fig. 3.4 (c). Once silver thicknesses are determined, the p-i-n junction height is determined so that the resonant wavelength overlaps with the semiconductor gain peak at room temperature using the round-trip condition as shown in Fig. 3(b). The resonance phase condition is given by

$$2n_{eff}\left(\frac{2\pi}{\lambda_0}\right)h + \Phi_{top}(d_1) + \Phi_{bottom}(d_2) = 2m\pi\,. \tag{3.4}$$

The phase shift of electrical field reflection coefficient at the bottom and top of the InP/Ag/air interface is calculated using the complex permittivity of silver. As is discussed in an earlier section, the phase-shift of a practical metal is less than π and is a function of the thickness as shown in Fig. 3.4(d).

Metal-encapsulated nanolasers have a small cavity volume compared with the minimum feature of the device structure. This allows us to simulate the 3-dimensional device using the finite-difference time-domain (FDTD) simulation to compare the results of the transfer-matrix methods. Fig. 3.5 shows our comparison between the transfer matrix method and the FDTD simulation for the cavity dimension optimized for the HE_{116} mode with a resonant wavelength at 1550 nm. Six peaks of the $\lambda_0/(2n_{eff})$ standing-wave shows an excellent agreement

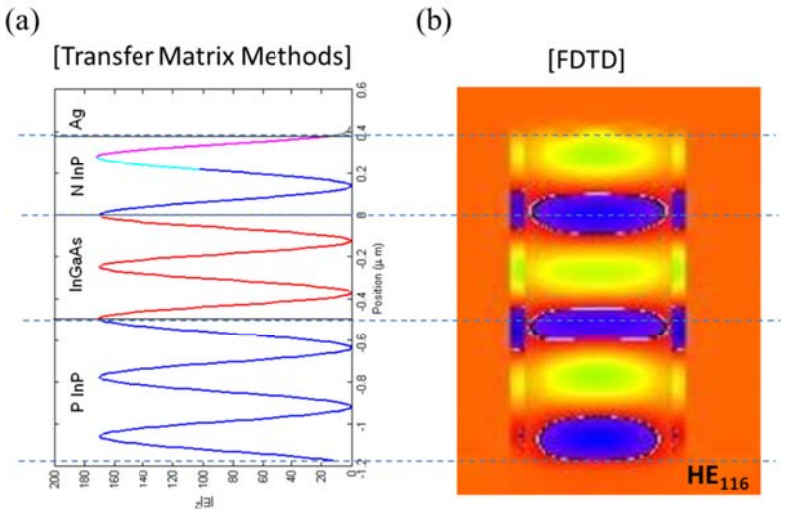

Figure 3.5 (a) Standing-wave for the cavity design optimized for HE_{116} with resonant wavelength of 1550 nm. Electrical field is calculated from the propagation matrix method using the fundamental design rule. (b) Cavity mode numerically calculated by finite-difference time-domain (FDTD) for the same cavity structure as (a). The field amplitude agrees well between two different methods.

between the two different methods. Even though the transfer matrix method is the first order approximation in the cavity design, it can estimate almost the same values for the resonant wavelength and the field pattern as the FDTD method. Since the transfer-matrix method requires a much smaller computational power, it allows us to optimize the cavity dimension and each layer thickness much faster than the FDTD (numerical) calculation. Using Eq. (3.2.2), the threshold material gain with a device diameter of only 660 nm is about 1,338 cm^{-1}, which is still achievable with bulk InGaAs semiconductors at room temperature.

Besides the HE_{116} mode shown earlier, we have designed a few other structures including the HE_{114} and HE_{111} modes. Figure 3.6 shows the simulation results for the cavity optimized to the HE_{114} mode at 1530 nm with a radius of 750 nm. The electric field is Er dominant with the maximum amplitude at the center of the cylinder (Fig. 3.6(a)). The InP cladding layer and InGaAs bulk gain layer

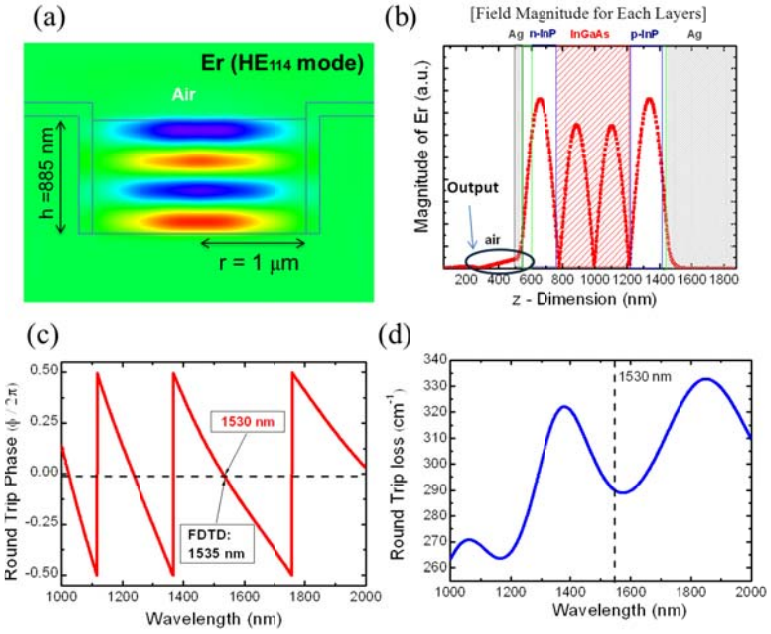

Figure 3.6 Design and simulation for the cavity with the fundamental HE_{114} mode. (a) The FDTD simulation result showing Er dominant mode with four peaks along the vertical direction. (b) The field magnitude in the vertical direction with the layer structures. It is seen that the output field can be collected through a thin metal layer on the top. (c) Round trip phase is calculated from the transfer matrix method for the same structure. The resonant wavelength is calculated as 1530 nm, which is close to the FDTD result of 1535 nm. (d) Round tip loss as a function of the wavelength.

thicknesses are designed according to the standing-wave pattern. In order to suppress the scattering loss at the InP/InGaAs interface layer, the active region thickness is designed such that the interface is located at the node of the fundamental mode as shown in Fig. 3.6 (b). It is seen that optical output can be coupled outside of the cavity through the optimized thickness of the metal on top. Figures 3.6 (c) and (d) show the round trip phase and loss with different wavelengths calculated using the transfer matrix method. The resonant wavelength is 1530 nm, which is in excellent agreement with that of the FDTD result of 1535 nm. The round trip loss has a local minimum around the resonant phase condition. As the wavelength becomes longer, the round trip loss increases

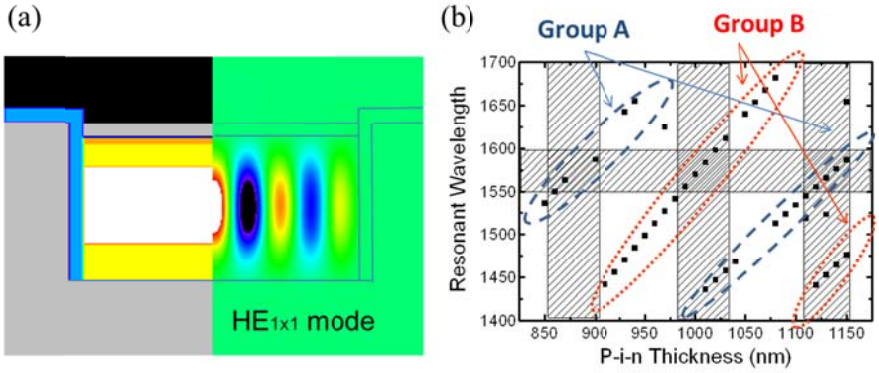

Figure 3.7 (a) Lateral confinement modes with the source of vertical polarization excitation. for the same structure as in Fig. 3.6. (b) Varying the p-i-n thickness to find the resonant wavelength shift for highest Q mode using the FDTD simulation.

because fewer nodes of the standing wave are formed in the cavity with an increased radiation loss (Fig. 3.6 (d)). When Eq. (3.2) is used for a large diameter of a 2-μm device, the quality factor in Fig. 3.6 (a) is 722 and the corresponding threshold material gain is 389 cm^{-1} for the HE_{114} mode with resonant wavelength of 1535 nm.

So far, only the fundamental HE_{11x} modes (k_z dominant) have been discussed in the metal-encapsulated lasers. However, as the vertical dimension shrinks and becomes comparable with the lateral dimension, other k_ρ or k_ϕ dominant modes start to come in. Figure 3.7 (a) shows one of the modes forming a standing wave in the lateral dimension. Figure 3.7 (b) illustrates the resonant wavelength as a function of the hetero-junction height with a fixed device radius 1.0 μm calculated from the FDTD method including all modes besides the HE_{11x} modes. There are a few groups of points, which increase the resonant wavelength linearly with the p-i-n thickness. The group A in the figure will be the HE_{11x} modes. The shorter p-i-n thickness side is HE_{114} and the longer side is HE_{115} modes. At the same resonant wavelength, the difference of the p-i-n thickness is about $\lambda/(2n)$ which

corresponds to adding one extra node in the standing wave. The group B will be considered to be other modes, which increase the resonant wavelength at a different rate. From this plot, we can see that the HE_{11x} mode does not necessarily have the highest quality factor depending on the p-i-n thickness and the target wavelength of the gain. The shadowed region in Fig. 3.7(b) is the gain bandwidth of our design at room temperature. The actual p-i-n height is decided to be 885 nm. A more detailed study of the metal-encapsulated cavity design for an ultimately small cavity volume has also been conducted [13].

The electrical design is as important as the optical design in the cavity for the maximum gain. Since the p-i-n junction height and the layer thickness are fixed from the resonant condition of the cavity, the optimization parameter in the electrical design is the doping concentration for each layer. For the MOCVD samples, due to the p-doping acceptor diffusion into an active layer at high temperature growth condition, the p-substrate is used and the n-type cladding layers are grown on the top of the active layer. The carrier concentration and the band structures are solved using a one-dimensional numerical simulation tool, which uses the finite element analysis to solve for the carrier Poisson equations and the rate equations. The simulation results after the optimized doping concentration are shown in Fig. 3.8. Our design consists of p-InGaAsP/p-InP/i-InGaAs/n-InP/n-InGaAsP hetero-junction for the MBE grown sample (for MOCVD sample, n and p are reversed). The top and bottom InGaAsP layers are highly doped for the electrical contact layer and serve as an etch stop for the substrate removal process. InP layers have a step graded doping concentration decreasing toward the i-InGaAs layer to prevent doping diffusion and minimize the depletion width.

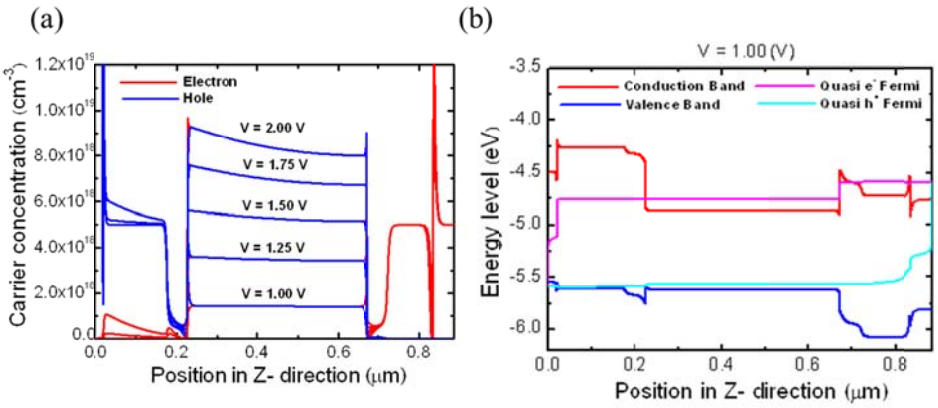

Figure 3.8 (a) Electron and hole concentration for an optimized hetero-junction at different applied biases. The x-axis represents the position from the top of the device. (b) Energy band diagram showing the conduction, valence band, and quasi-Fermi levels for electron and holes.

3.3 Device Processing

The device processing of a metal-encapsulated nanolaser is quite challenging. First, a quality factor and threshold gain calculation in Section 3.2 are from the ideal structure. In reality, crystal growth can contain defects and doping diffusion, which reduce the optical gain, and the cavity sidewall is not perfectly vertical and becomes rough from the dry etching process. The top layer of the semiconductor is not perfectly flat, causing scattered light by reflection. The metal deposition has a finite size of non-uniform grains, which reduce the reflectivity from the perfect crystalized metals. Secondly, some of processing recipes need to be newly developed because they have not been studied in the previous works. One of the challenges is the electrical isolation of a small cavity, which is enclosed by metal in all directions. As shown in the device schematics in Fig. 3.2, only a thin SiN_x layer is separating anode and cathode. When opening the current injection window, too short an etching time can cause open circuit of the device and a slight overetching immediately results in short circuit for the finished samples. In this

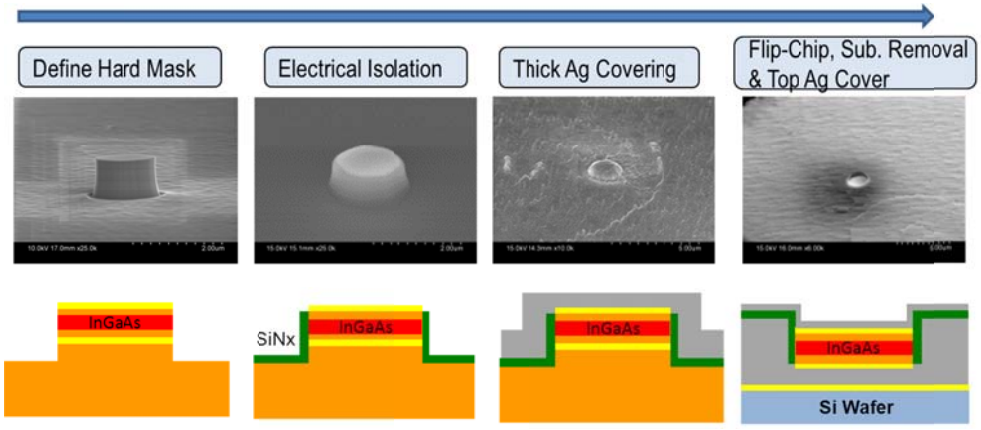

Figure 3.9 Overview of processing procedures of metal-encapsulated nanolasers showing scanning electron microscopic (SEM) images and schematic diagram for corresponding steps.

work, the majority of time has been spent on the trial and error to improve processing devices in the cleanroom. Thus, a considerable number of details in processing are discussed this section to explain the challenges and improvements for a better performance of the devices.

Figure 3.9 shows an overview of the processing procedures with the scanning electron microscopic (SEM) images and the schematic diagrams of the major steps. In short, the cylindrical cavity is formed by dry etching as shown in the leftmost pictures in Fig. 3.9. Then, a SiN_x layer is formed for electrical isolation, but only the top of the cavity is removed for current injection. After a thick silver layer is deposited to form a metal cavity, the sample is flip-chip bonded to another wafer and the original substrate is removed. Finally, a top thin metal reflector is deposited and the contact pad is defined for characterization. The details of the challenges and improvement of the processing recipes are discussed in the following.

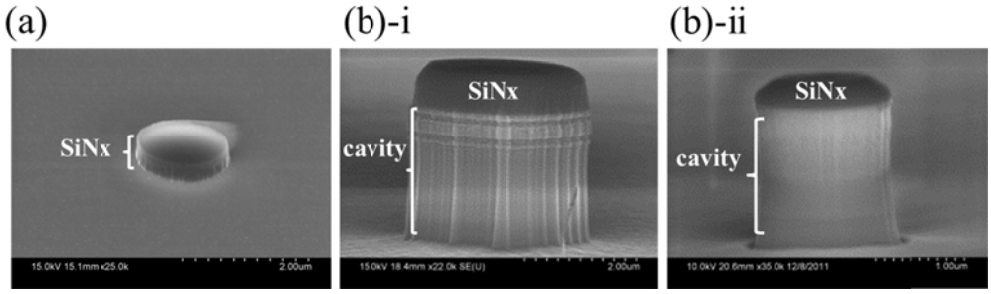

Figure 3.10 (a) SiNx mask used as a hard mask of etching the cavity. (b)-i Dry etching result using the SiNx mask defined by (photo-resist) PR mask. The zigzag peripheral SiNx mask pattern is transferred to the unsmooth cavity sidewall. (b)-ii Dry etching result using the SiN_x mask defined by a Ni hard mask followed by PR lift-off procedure. Due to the smooth edge of the SiNx mask, the sidewall of the cavity is much smoother.

After chemical cleaning of the sample, the first process is depositing the SiN_x film which serves as a hard mask to define the cavity. Patterning of this SiN_x mask is very important because it directly defines the cavity shape. Figure 3.10 (a) shows SiN_x mask pattern where (b)-i and (b)-ii compare the etching results for the cavity using the different methods to define the mask patterning. Figure 3.10 (b)-i is using the photoresist (PR) as a mask to etch and define the SiN_x. This recipe is widely used for various device processing. However, when PR is developed after optical lithography, the edge of PR has a thinner resist by negative slope (for negative resist) or positive slope (for positive resist). Since the selectivity of SiN_x and PR is not good for Freon etching, this thinner PR causes a zigzag peripheral pattern on the SiN_x mask. This zigzag pattern directly transfers to the cavity sidewall roughness as shown in the SEM picture. This is not a big problem in large size devices, but it is critical for nanolasers because it causes undesired scattering loss. To solve this problem, we added an extra step to deposit nickel (Ni) for a hard mask to etch SiN_x. Because Ni is patterned by lift-off of PR, the PR thickness slope is not transferred to Ni pattern. SiN_x and Ni have excellent

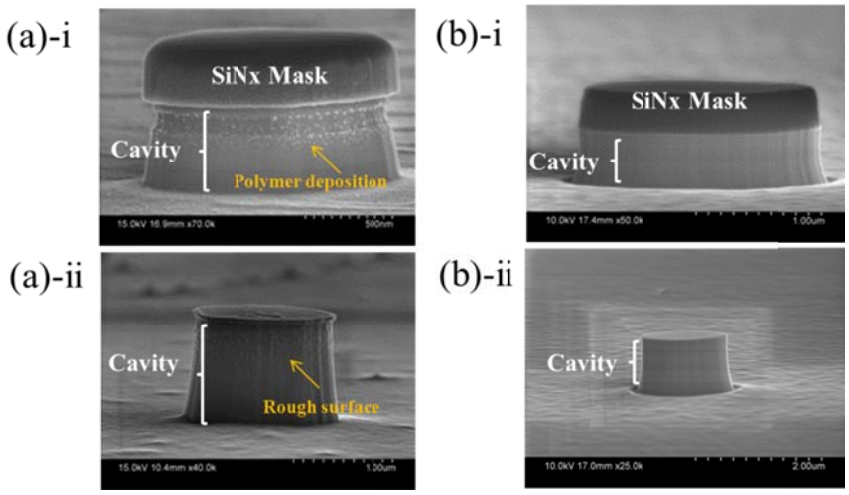

Figure 3.11 (a)-i Dry etching using methane (CH_4) and hydrogen (H_2) based plasma at room temperature. Polymer bi-product is deposited on the sidewall. (a)-ii After SiN_x mask is removed and polymer is cleaned for CH_4 and H_2 based plasma etching. (b)-i Dry etching using silicon tetrachloride ($SiCl_4$) and argon (Ar) based plasma at 200 ^oC. (a)-ii After SiN_x mask is removed $SiCl_4$ and Ar based plasma etching.

selectivity by Freon etching. As a result, a smooth circular cavity is shown in Fig. 3.10 (b)-ii.

Besides smoothness of the SiN_x mask to etch the cavity, the etching recipe itself is very important. Etching InP materials is more challenging compared with GaAs material in previous QD MCSEL devices due to relatively involatile nature of the heavy indium atoms. Some of the nanocavity design (HE_{111}) requires a shallow etching of the InP materials of the order of 200 nm. Many processing recipes do not work with shallow etching because the etching floor is rough and cannot continue to the next SiN_x passivation process. The vertical sidewall and similar etching rate of InGaAsP, InP, and InGaAs layers are required for a continuous cavity wall. In an early generation of devices, we used reactive ion etching (RIE) with methane (CH_4) and hydrogen (H_2) based plasma at room temperature. This recipe has the advantage of a very slow etching rate, which is good for shallow etching and a precise control of the etching depth. However,

CH_4 and H_2 based plasma etching causes polymer byproduct deposition as shown in Fig. 3.11 (a)-i. Even though polymer deposition can be removed from the hydrogen fluoride (HF) wet process, the rough sidewall is translated to the sidewall as shown in Fig. 3.11 (a)-ii. The chlorine (Cl_2) gas etching at elevated temperature has no polymer deposition problem, but it was difficult to develop etching recipes for shallow etching. After several rounds of trial and error, we developed etching recipes with induced coupled plasma reactive-ion etching (ICP-RIE) using silicon tetrachloride ($SiCl_4$) and argon (Ar) mixture gases with substrate temperature heating to 200 ^oC. Even though the etching rate is rapid, smooth sidewall and floor can be achieved at optimized gas ratio between $SiCl_4$ and Ar. The etching profile is shown in Fig. 3.11 (b)-i and (b)-ii. The change of recipe from CH_4 + H_2 to $SiCl_4$ + Ar significantly improved the device performances.

As mentioned earlier, one of the difficult processings is electrical isolation of the p-i-n hetero-junction with the metal covered in all direction. Figure 3.12 illustrates the basic procedures to form the electrical isolation layer and current injection window on the top. First, a SiN_x film is uniformly deposited on the cleaned device surface by plasma-enhanced chemical vapor deposition (PECVD). The material property of SiN_x depends on the plasma frequency. In our device, it is required that SiN_x has no leakage current (high density) and a small film stress for device stability. For this purpose, we used mixed frequency (13.56 MHz and 380 kHz) plasma deposition. After the SiN_x film deposition, the key process is removing SiN_x on the top of cavity but keeping the sidewall and floor. This process is quite challenging when the device height is short for the HE_{111} design (200 nm). We developed recipes using the PR spin coating following the

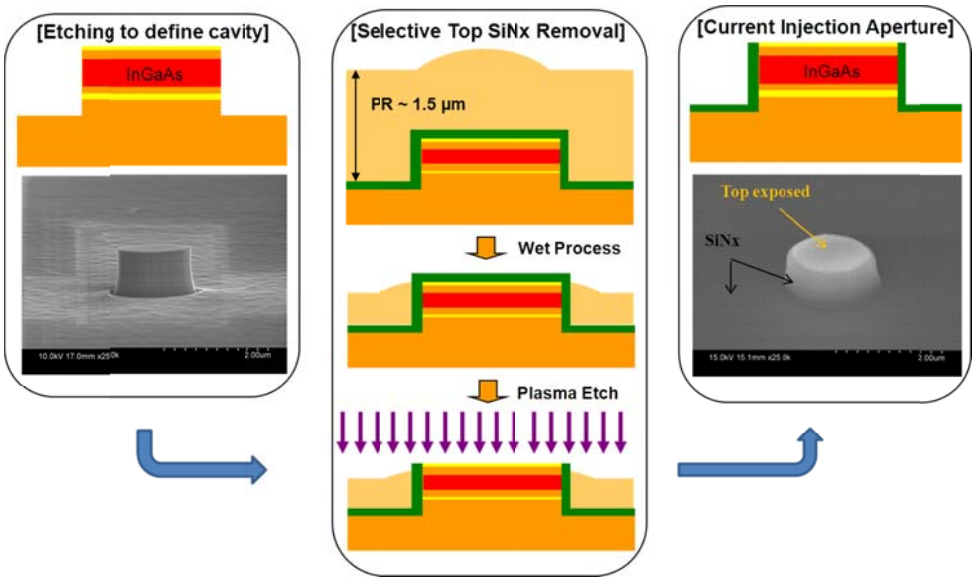

Figure 3.12 The key steps to form the electrical isolation layer with only the top part of SiN_x removed. Extremely precise wet process control is necessary when the cavity height is small (the smallest feature is the HE_{111} cavity design with a height of 200 nm).

partial development. By adjusting the PR bake time, ultra-violet (UV) exposure dose, and development solutions, it is possible to expose only the top of the cavity even when the device height is as small as a few hundreds nm. As seen from Fig. 3.12, when PR after wet process is too thick, the top window of the nanocavity cannot be opened and the devices become open circuits. When PR is too thin, the SiN_x floor will have holes in the later process resulting in short circuit devices. Our optimized recipe can reproduce almost identical results with a large tolerance in the wet process time. Then, the top SiN_x layer is dry etched by anisotropic plasma etching at low pressure, and PR is removed from the surface of the sample as shown in the last picture in Fig. 3.12.

Figure 3.13 illustrates the processing from the thick silver coverage to the finished device. A thick silver layer is deposited by electron-beam evaporation method with a tilted sample, then rotated to cover silver in all directions. Plasma

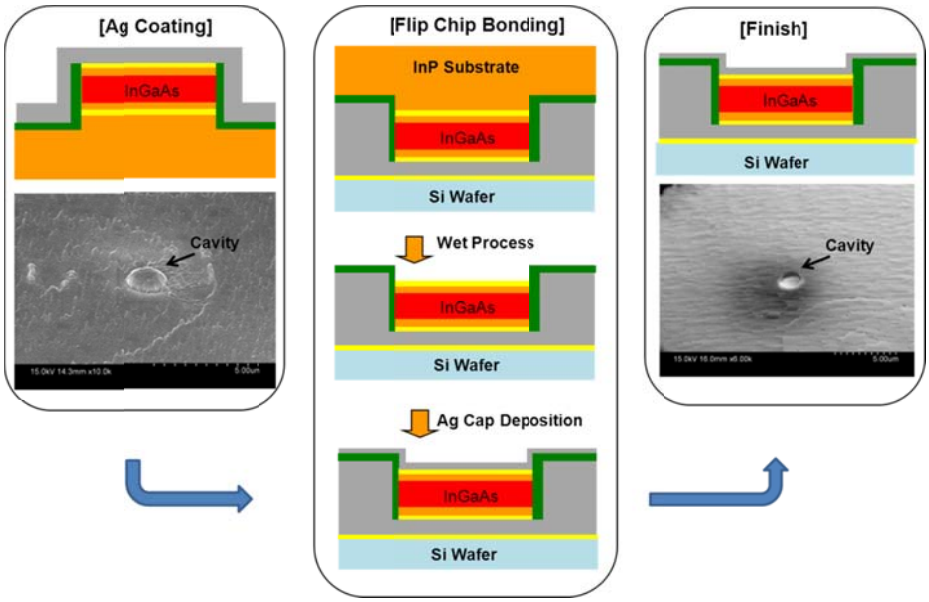

Figure 3.13 The key steps for flip-chip bonding and substrate removal. Several methods of flip-chip bonding are examined including conductive epoxy bonding with heat annealing, metal atomic diffusion bonding, and eutectic bonding methods. The device yield is strongly affected by the wafer bonding stability.

sputtering may be a good alternative method because it can give a conformal silver cover and a higher energy of metal particle improves adhesion to the sample surface better. Because silver is not adhering to the sample surface well, photo-lithography is done so that silver is deposited only around the cavity. Several methods of flip-chip bonding are examined including conductive epoxy bonding with thermal cure, metal diffusion bonding with gold, and eutectic bonding using gold and tin or indium alloys. In all recipes, it is important to keep the substrate temperature below 300 ^{o}C and guarantee the bonding interface is stable to the exposure of solvent and acid, which is necessary in the later processing. In some samples, the epoxy based photoresist is patterned and thermally cured to form a mechanical support to protect the cavity. The substrate removal is done by InP etching by HCl with InGaAsP etching stop at the bottom

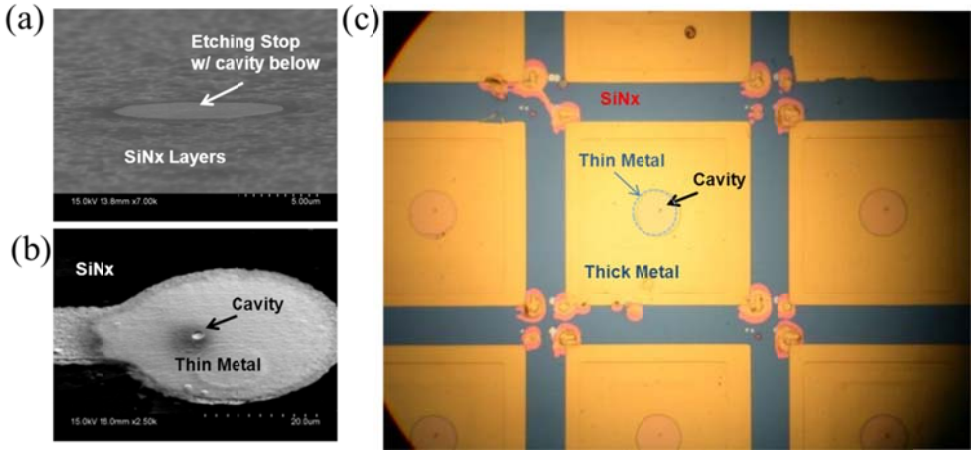

Figure 3.14 (a) SEM image after substrate removal. InGaAsP etching stops can give smooth surface on the device surface, which is important for good reflectivity. (b) SEM image after depositing a thin metal layer on top of the device as a reflector. (c) Microscope image of the finished device. Thin metal is deposited around the cavity and a much thicker metal is deposited as stable electrical contact pad for probing.

of p-i-n junction. Finally, a thin metal (silver or gold) is deposited on top of the device as a reflector.

Figure 3.14 (a) shows an SEM image after substrate removal. It is seen that the InGaAsP etching stop can give a smooth surface on the device, which is important for good reflectivity. We have deposited 30 nm ~ 50 nm of either silver or gold as a top reflector (Fig. 3.14 (b)). Since this is too thin as a contact pad for electrical testing, thick titanium (Ti) and gold (Au) are deposited as shown in Fig. 3.14 (c). The mask consists of 15 by 15 arrayed devices with device diameters ranging from 1.0 to 10 μm.

3.4 Device Characterization

3.4.1 Characterization of HE_{111} Cavity Design

The device performance is measured at room temperature with electrical injection. Figure 3.15 (a) shows the device schematic of the smallest metal nanocavity light emitters designed for the fundamental mode of HE_{111}. The inset of magnified cavity image is FDTD simulation result. Among the different sizes of devices, radius 0.75 μm device is the smallest device working as nanocavity diode emitter. The voltage vs. current (I-V) and light output vs. current (L-I) curves at two different temperatures are shown in Fig. 3.15 (b). The I-V curves indicate a good electrical isolation between the anode and the cathode by a thin 100 nm SiN_x layer. It shows diode turn-on voltage at 1.06 V. From the I-V curve, it is observed that the series resistance is about 640 Ω, which is less than half of the metal-cavity VCSEL series resistance in Chapter 2 for the same diameter (1.555 kΩ). One reason for the smaller series resistance is the shorter cavity height, although other factors such as doping concentration of each layer material or metal contact affect this value. The smaller series resistance suppresses heat because ohmic heat generation scales with the square of resistance. The two L-I curves show that increased temperature decreases the slope efficiency. The slope efficiency is 0.31 and 0.27 mW/A at 15 °C and 28 °C, respectively. The output increases almost linearly without saturation. The device becomes electrically unstable when injection current exceeds 1.0 mA. The electroluminescence spectrum of our processed device and photoluminescence (PL) spectrum of epiwafer are shown in Fig. 3.15(b), both measured at room temperature (28 °C). In this smallest fabricated device, we have

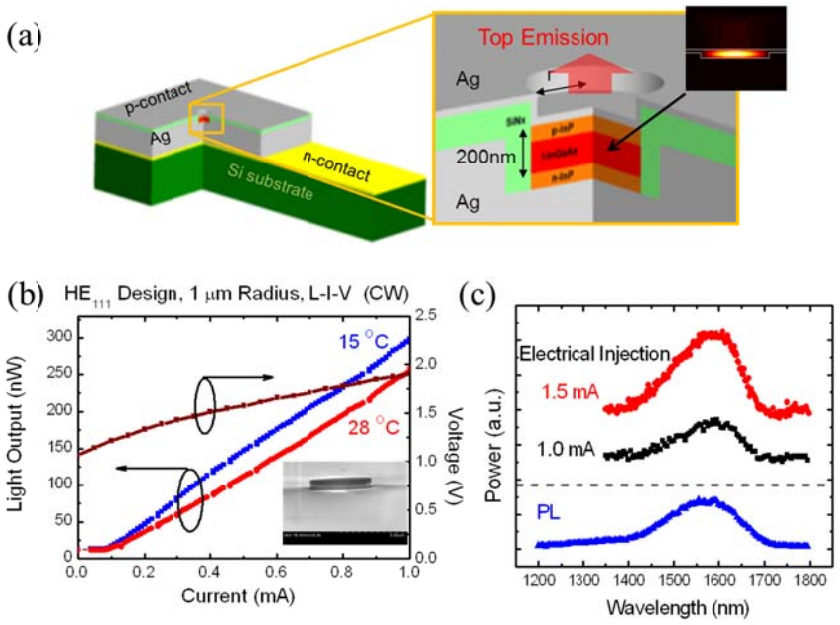

Figure 3.15 (a) Device schematic of the smallest cavity design HE_{111}. The cavity height is 200 nm with the smallest light emitting device of radius 1.0 μm. The inset of magnified image shows the FDTD simulation result of HE_{111} modes. (b) Light output and voltage vs. current (L-V-I) near room temperature. The inset figure shows etching profile of the device. (c) Electroluminescence spectra after processing and photoluminescence on the epi wafer before processing [14].

not observed lasing or cavity mode so far. Since the optical output is dominated by spontaneous emission and 40 nm top silver has transmission of only about 2 %, the slope efficiency in the L-I curve is very low. It has been observed that small deviation of the substrate temperature changes the light output power more than expected from the gain model, indicating that metal loss significantly increases with temperature. This is why most nanolasers are demonstrated at cryogenic temperature. The cavity quality factor is too low to reach the threshold condition for such a small metal-cavity at room temperature. Due to the processing difficulties for the short cavity, 36 devices out of 202 tested devices show good I-V diode curve and the others show short or open circuits. Among 36 good electrical devices, 4 devices show measurable light emission. Yet, this is one of

the smallest nanocavity light emitting diodes ever reported. The device cavity volume encapsulated by metal is 0.35 μm^3, which corresponds to 0.086 λ_0^3 in terms of emitting wavelength. Although the processed nanocavity emitter has a miniature active volume, it does not show any degradation in the optical spectrum.

3.4.2 Characterization of HE_{114} Cavity Design

In our research, we designed a few different cavity dimensions such as the HE_{111}, HE_{114}, and HE_{116} modes. Each design has a different thickness of the epi-wafer and the crystal is grown by different methods such as MBE or MOCVD from different institutions or venders outside of UIUC. The crystal growth quality is as critical as the cavity design and device processing for nanolasers. For the best results, the feedback and iteration between crystal grower and device engineer are absolutely necessary to make the fabricated device as close as possible to the ideal device structure. Figure 3.16 shows the device performance of the HE_{114} fundamental mode design. The device schematic with the FDTD simulation result is shown in Fig 3.16 (a). From the I-V curves in Fig. 3.16(b), there is no clear turn-on voltage as in Fig. 3.15(b) or 3.19(b). Even though the contact potentials of all designs are almost the same, this epi-wafer has significant forward current at low bias like 0.5 V, whereas other epi-wafers have a negligible forward current at the same bias. We suspect that there are deviations in the doping profile from the ideal case shown in Fig. 3.8. The L-I curve is shown for the 1.5-μm diameter device in Fig. 3.8 (d) and 2.0-μm diameter device in (d). The cavity volume is 0.39 and 0.68 λ_0^3, respectively, in terms of the emission wavelength. The output power is much weaker than those from other epi-wafers.

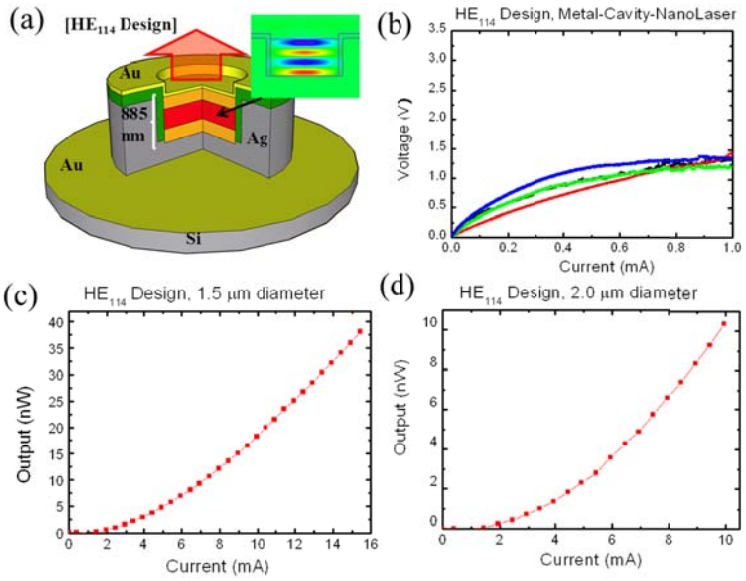

Figure 3.16 (a) Device schematic of the HE_{114} cavity design with inset showing the FDTD result of cavity mode. (b) The I-V curves for several devices at the different locations on the chip. (c) The L-I curve for 1.5 μm diameter device. (d) The L-I curve for 2.0-μm diameter device.

The radiative carrier recombination in the active bulk layer is not efficient and most samples even do not emit measurable light output. This is also observed by processing a large device from this wafer giving poor L-I-V characteristics. More iterations between crystal growers are necessary.

3.4.3 Characterization of the HE_{116} Cavity Design

Figure 3.17 shows performances of nanocavity light emitters designed for the HE_{116} fundamental cavity with a volume (radius = 1 μm, height = 1.599 μm, and a cavity volume of 1.23 λ_0^3) with CW current injection at room temperature. In this device, the maximum light output was almost 10 times larger than that of our previous smallest HE_{111} cavity design sample. The processing yield is much better than the small HE_{111} cavity design with 160 devices out of 225 emitting light. The

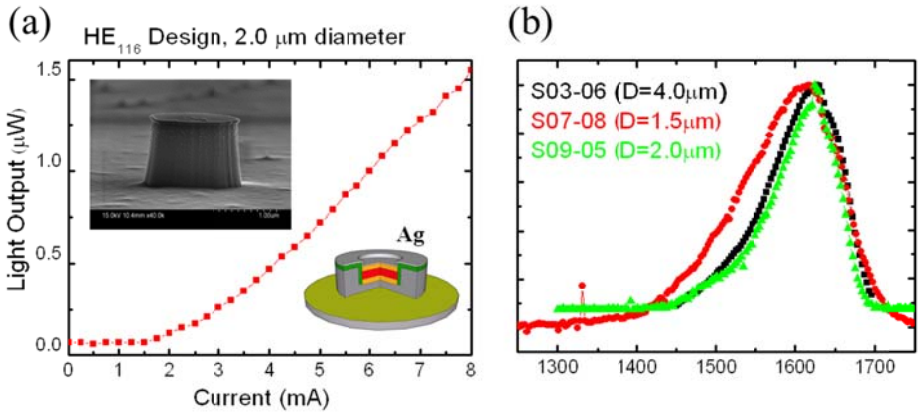

Figure 3.17 (a) The L-I curve for the cavity design for the HE_{116} mode. The device is fabricated with CH_4 and H_2 based dry etching and a 40 nm silver layer is used on the top reflector. (b) Optical spectra for various sizes of diameter at room temperature. The linewidth of spectrum varies among the different devices.

spectra of different devices in Fig 3.17(b) show different linedwidth for each device. In general, the larger diameter has a narrower linewidth compared with the small device. Since this device is fabricated in an early stage using CH_4 and H_2 based plasma etching, the cavity sidewall is not very smooth as shown in Fig. 3.17(a) inset (see Fig 3.11 for the impact of dry etching method).

Figure 3.18 (a) shows one of the narrowest linewidth spectra of the HE_{116} cavity design devices in the early stage of device fabrication. The epi wafer photoluminescence (PL) spectrum is compared in Fig. 3.18(b) in the same x-axis scaling. The PL spectrum is about $\Delta\lambda$ = 200 nm whereas the processed 2.0 μm device with electrical injection has a full-width half-maximum less than 80 nm. Above the current injection of 5.0 mA, sharp peaks with linewidth of 8.3 nm are observed. This could be the potential cavity mode of the metal cavity. As the current injection is increased further, the device dies from too high current density. In this early stage of fabricated devices, a 40 nm silver film is used as a top

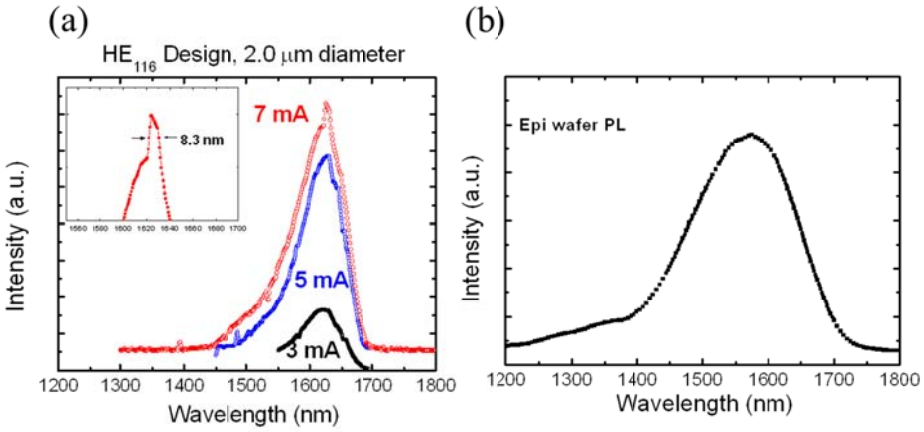

Figure 3.18 (a) Current injection optical spectra for HE_{116} design cavity. As current exceeds 5 mA, small peak is observed before the device dies from overinjection. (b) Epi-wafer photoluminescence without any processing.

reflector because of the small optical losses at 1.55 μm. During measurement, it is observed that the top silver contact has changed color under the microscope after high driving current density. This is probably due to the oxidation of silver with high temperature by injection. In the later processing recipes, this is improved by using other metal deposition.

Since the HE_{116} cavity design shows promising results in the optical spectrum as shown in Fig. 3.18(a), we further investigate the processing recipes and deposition materials for better performance. Fig. 3.19 shows the characterization of newly processed devices with the improved processing. First, the high temperature dry etching with $SiCl_4$ and Ar gases is used for a much smoother sidewall profile (Fig. 3.11), which will reduce the scattering loss especially for the small diameter cavities. Also after opening the SiN_x top window by Freon dry etching, a single layer of thin InP is removed by wet etching to remove the damaged semiconductor crystals and improve the metal mirror interface.

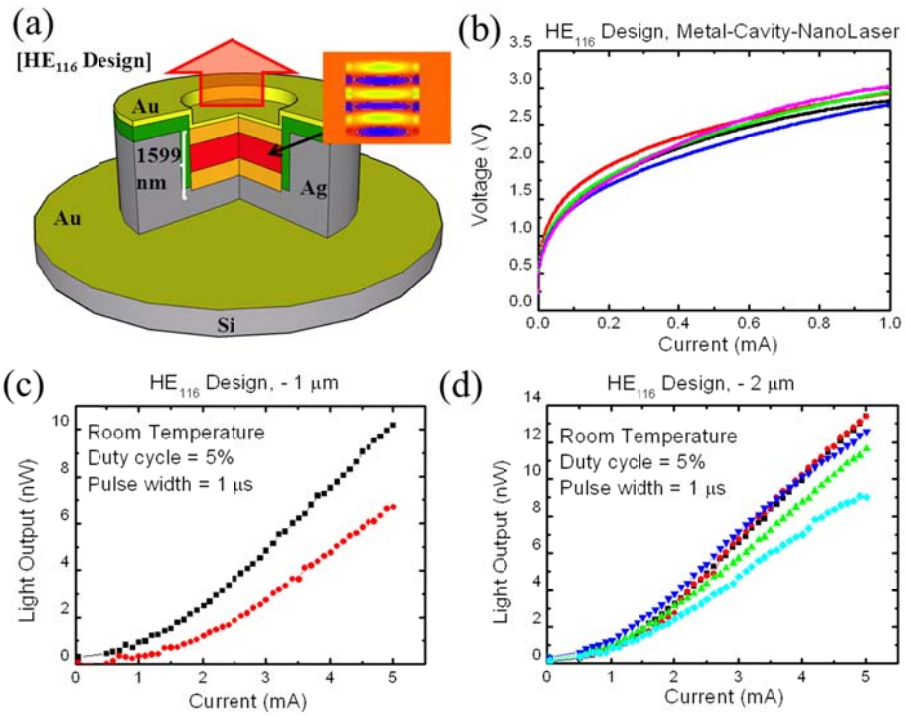

Figure 3.19 (a) Device schematic of the HE_{116} cavity design with inset showing the FDTD result of the fundamental cavity mode. Gold is used for the top reflector and dry etching method is improved from earlier processing recipe. (b) The I-V curves for several devices at the different location on the chip. (c) The L-I curves for the 1.0-um diameter devices. (d) The L-I curves for the 2.0-μm diameter devices.

Further, wafer bonding method is improved by lowering bonding temperature, but increasing the bonding mechanical pressure for a better binding interface. The top reflector is changed from a 40 nm silver to a 50 nm gold for higher reflectivity and less reactive metals for device stability. Finally, the contact pad has thicker titanium and gold layers to prevent the scratching damage from the probe during measurement. The I-V curve shown in Fig. 3.19(b) shows very good electrical characteristics where most devices on the same size had similar curves indicating high reliability of the devices. Figures 3.19(c) and (d) show the L-I curves for 1-μm and 2-μm diameter devices at room temperature. The super-linear output,

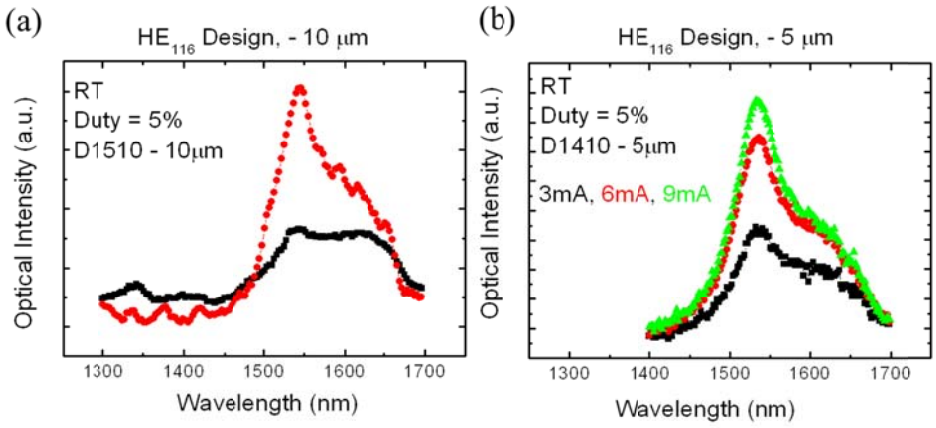

Figure 3.20 Optical spectra of (a) 10 μm and (b) 5 μm devices for improved processing device with a thicker 50 nm gold layer on top of the metal reflector. The cavity mode is observed for these devices.

which is different from the typical light emitting diodes (LEDs), is observed from most devices. However, the optical output is much weaker than the previous design due to the thicker gold reflector on the top.

The optical spectra of the improved HE_{116} cavity design are shown in Fig. 3.20 for different diameters. With improved design, we observe clear cavity modes from most of the devices. The cavity mode has a shorter wavelength than that of the design because the top InP layer is chemically etched away to remove the dry etching damage as mentioned earlier. As the injection current increases, the relative amplitude of narrow cavity mode increases compared with the background spontaneous emission indicating that the stimulated emission rates at these wavelengths are more dominated by the cavity feedback. At this moment, the cavity mode output eventually saturates with increasing the carrier pumping. It is believed that high carrier density heats the sample, reducing the material gain and increasing ohmic loss of metals, which prevents reaching the threshold condition.

3.5 Summary

In the previous chapter, we identified two challenges in the metal coated VCSEL for further cavity volume reduction: i) Lateral size reduction is difficult due to significant heat generation from the high series resistances through micro-pillar DBR. ii) Vertical size reduction (removing pairs of DBRs) is difficult because the top metal interface can easily disturb the phase of the standing-wave, significantly reducing reflectivity and shifting the gain peak. To solve this problem, we have designed, fabricated, and characterized metal-encapsulated nano-light-emitters with bulk in the active region. The first principal design rule is used to calculate the three-dimensional problem decomposed into micro metal-coated waveguide problem and the transfer matrix methods to estimate the fundamental mode resonance and threshold condition. The result based on this design rule agrees very well with the numerical three-dimensional calculation using the FDTD methods. The device recipes have been developed by multiple iterations from the device characterization. Many recipe improvements developed here can be applied in the other device processing as well. The smallest metal cavity diode emitter with electrical injection is 0.086 λ_0^3 in terms of emitting wavelength working at room temperature. It is shown that the series resistance of metal-encapsulated nanocavities is much smaller than the metal coated VCSEL, suppressing heat generation for the small diameter devices. Even though the cavity mode of metal nanocavity devices had not been observed in the earlier stage of processed devices, the fabrication improvement shows a narrow cavity mode in the metal nanocavity with a volume of 1.23 λ_0^3 at room temperature.

In conclusion, one of the smallest electrical injection light emitters is demonstrated with the nanocavity completely encapsulated by metal. For the appropriate cavity mode design and processing recipes, narrow cavity modes can be observed in several devices. However, cavity mode magnitude saturates with high current density by gain reduction and increase of metal loss, making it hard to reach the threshold condition. The dominant factor of high threshold gain for this device is radiation loss in the dominant wave-vector direction (vertical direction) because cavity length L in this direction is so small. Thus, it is most important to figure out how to reduce the radiation loss in the wave propagating direction. In the next chapter, we propose a novel device, which has game-changing potential in the nanocavity design with the concept of mirror gain, which not only solves the high radiation loss problem but also suggests better performance in smaller cavities.

3.6 References

[1] K. Yu, A. M. Lakhani, and M. C. Wu, "Subwavelength metal-optic semiconductor nanopatch lasers," *Opt. Express*, vol. 18, pp. 8790-8799, 2010.

[2] M. P. Nezhad, A. Simic, O. Bondarenko, B. Slutsky, A. Mizrahi, L. Feng, V. Lomakin, and Y. Fainman, "Room temperature subwavelength metallo-dielectric lasers," *Nat. Photon.*, vol. 4, pp. 395-399, 2010.

[3] M. T. Hill, Y. S. Oei, B. Smalbrugge, Y. Zhu, T. de Vries, P. J. van Veldhoven, F. W. M. van Otten, T. J. Eijkemans, J. P. Turkiewicz, H. de Waardt, E. J. Geluk, S. H. Kwan, Y. H. Lee, R. Notzel, and M. K. Smit, "Lasing in metallic-coated nanocavities," *Nat. Photon.*, vol. 1, pp. 589-594, 2007.

[4] M. T. Hill, M. Marell, E. S. P. Leong, B. Smalbrugge, Y. Zhu, M. Sun, P. J. van Veldhoven, E. J. Geluk, F. Karouta, Y. Oei, R. Notzel, C. Z. Ning, and M. K. Smit, "Lasing in metal-insulator-metal sub-wavelength plasmonic waveguides," *Opt. Express*, vol. 17, pp. 11107-11112, 2009.

[5] C. Y. Lu, S. L. Chuang, A. Mutig, and D. Bimberg, "Metal-cavity surface-emitting microlaser with hybrid metal-DBR reflectors," *Opt. Lett*., vol. 36, no. 13, pp. 2447-2449, 2011.

[6] S. H. Kwon, J. H. Kang, C. Seassal, S. K. Kim, P. Regreny, Y. H. Lee, C. M. Lieber, and H. G. Park, "Subwavelength plasmonic lasing from a semiconductor nanodisk with silver nanopan cavity," *Nano Lett*., vol. 10, pp. 3679-3683, 2010.

[7] A. Matsudaira, C. Y. Lu, A. Millard, and S. L. Chuang, "Metal-coated quantum-dot lasers," *International Nano-Optoelectronic Workshop*, Beijing, China, 2010.

[8] S. W. Chang and S. L. Chuang, "Fundamental formulation for plasmonic nanolasers," *IEEE J. Quantum Electron.*, vol. 45, no. 8, pp.1014-1023, Aug. 2009.

[9] P. B. Johnson and R. W. Christy, "Optical constants of the noble metals," *Phys. Rev*. B 6, pp. 4370-4379, 1972.

[10] E. D. Palik, *Handbook of Optical Constants of Solids*, Academic Press, Boston, 1985.

[11] A.D. Rakić, "Algorithm for the determination of intrinsic optical constants of metal films: application to aluminum," *Appl. Opt*. 34, pp. 4755-4767, 1995.

[12] SOPRA N&K Database, (2012, Mar.) [Online]. Available: http://www.sopra-sa.com/index2.php?goto=dl&rub=4

[13] C. Y. Lu, S. L. Chuang, "A surface-emitting 3D metal-nanocavity laser: proposal and theory," *Opt. Express*, vol. 19, no. 14, pp. 13225-13224, 2011.

[14] A. Matsudaira, C. Y. Lu, S. L. Chuang, and L. Zhang, "Demonstration of metallic nano-cavity light emitters with electrical injection," CLEO:2011 - Laser Applications to Photonic Applications, OSA Technical Digest (CD) (Optical Society of America, 2011), paper JMA5.

CHAPTER 4

NANOLASERS USING METAL-SEMICONDUCTOR-METAL STRUCTURE FOR CUTOFF REFLECTION FEEDBACK

4.1 Motivation

4.1.1 Introduction

Recently, intense study has been devoted to metal for nanoscale optical confinement [1-4] and sub-wavelength optical mode propagation [5-7]. Even though metal is an excellent candidate for nanophotonic devices, high optical loss is makes it challenging to realize room temperature operating devices. Most previous works use metal as a reflector by coating the cavity [1, 4] or as a surface plasmonic waveguide to confine the light at the metal-semiconductor interfaces [2-3, 8]. In the previous chapters, metal coating is used as a reflector of the cavity. Even though the metal has a high optical reflectivity, there is a finite transmission into the metal. For a short cavity, distributed radiation loss is very sensitive to the mirror reflectivity and is critical for the threshold gain condition.

Table 4.1 shows typical values of reflectivity and mirror length for different laser structures. The cleaved Fabry-Perot laser has a small reflectivity, but radiation loss is small because of the long cavity. The state-of-the-art GaAs/AlGaAs distributed-Bragg reflector (DBR) in vertical-cavity surface-emitting lasers (VCSELs) can achieve high reflectivity of an order of 0.99

Table 4.1 Typical values for various cavity mirrors

	Reflectivity	Mirror Length	Cavity Length	Radiation Loss α_m (cm-1)	Emission
Cleave	0.3	0	500 μm	24.08	Edge
VCSEL	0.99~0.999	3 ~ 5 μm	~ 1 μm	50.13	Surface
Metal	0.987	~ 30 nm	~ 1 μm	130.85	Surface
Cutoff*	0.995	~ 500nm	~ 1 μm	50.13	Edge
Cutoff w/ gain*	1.005	~ 500nm	~ 1 μm	-49.94	Edge

*Theoretical values calculated

~ 0.999 with 20 ~ 35 DBR pairs. For an ultra-high reflectivity DBR, the mirror length extends to 3 ~ 5 μm, increasing the total cavity volume. In Chapter 2, we demonstrated hybrid metal-DBR mirror lasers with 5.5-DBR-pairs, which correspond to about 850 nm mirror length. Further reduction of mirror size is challenging due to precise phase matching condition of DBR-metal interface. On the other hand, metal can be used as a high reflectivity mirror with a negligible mirror thickness. From the previous chapter, we found that silver (Ag) or gold (Au) has the highest reflectivity at near-infrared wavelength. However, the reflectivity of the mirror saturates to 0.950 ~ 0.987 (for Au and Ag) even with the thick metal layers (see Section 3.2.3). This is due to the finite transmission of the incident light and ohmic loss inside the metals. As shown in Table 4.1, the radiation loss of metal cavities is relatively large.

In this chapter, we study a novel mirror structure using modal cutoff feedback. Figure 4.1 shows the device schematics of our proposed modal cutoff laser and its cross-sectional view. This laser utilizes the following principles to effectively confine optical modes in a given geometry. It is well known that the transverse electric (TE) mode has no cutoff on a symmetric dielectric

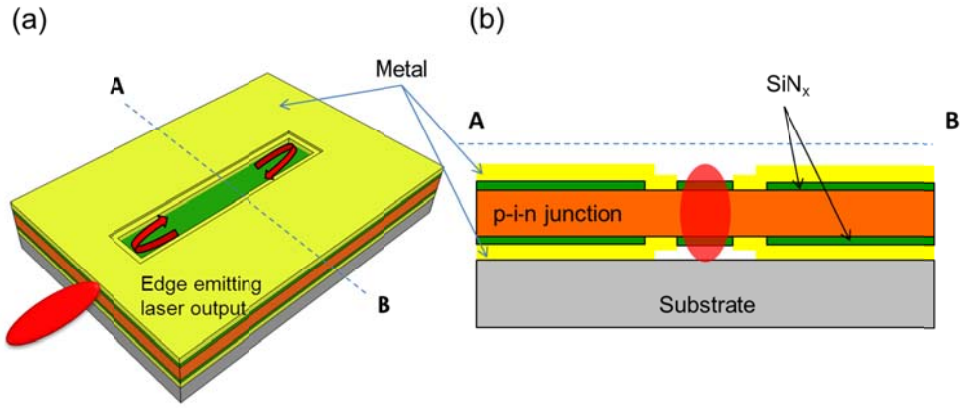

Figure 4.1 Edge-emitting semiconductor laser using modal cutoff on MSM structure as an optical feedback. (a) Schematic of device and (b) cross-sectional view between A and B on the left figure.

(semiconductor) waveguide, which means that the wave can propagate even within a thin semiconductor layer. However, when a metal layer is placed on the top and the bottom of the semiconductor (a metal-semiconductor-metal (MSM) structure), TE modes start to reach the cutoff condition as the semiconductor layer becomes thinner. When the TE modes reach cutoff, the majority of optical power is reflected back to the opposite direction. The modal cutoff confinement cavity uses this strong feedback of the MSM structure for nano/micro cavity lasers. The details of the operation principle are explained in Section 4.2.1. The semiconductor hetero-junction thickness is carefully designed such that the fundamental TE mode becomes cutoff in the MSM region. Thus, an optical mode is strongly confined in the middle stripe region, where no metal is placed on top and bottom of the semiconductor layer. By adjusting the MSM region length on one side of the device, we can extract edge emitting laser output from desired side. In this device, the top and bottom metals not only serve as modal cutoff confinement, but also provide the electrode for current injection. Carrier diffusion into the cavity area can be enhanced by high doping on the top and bottom

semiconductor layers.

4.1.2 Advantages Compared with Previous Nanolasers

There are several advantages for nanolasers to use the lateral cutoff mirror compared with the previously reported nanolasers.

i) High reflectivity comparable with a large number of DBR pairs can be achieved with about 500 nm total thickness of mirror length.

ii) Metal loss can be minimized due to a small field overlap with metal.

iii) Edge emission coupling suitable for planar light-wave circuit.

iv) It is possible to achieve reflectivity more than unity by placing gain in the mirror region.

v) Easier and potentially cheaper fabrication.

Especially, the concept of mirror gain is advantageous for the short cavity nanolasers. In the following, we discuss examples to observe the advantages of modal cutoff lasers.

One of the similar device structures is using a metal-semiconductor-metal patch to confine the light using plasmonic mode [8]. In this approach, optical confinement in the lateral direction is weak due to the radiation loss between semiconductor and air. Furthermore, the optical loss is considerably large due to a large overlap of the mode profile with the metal. Compared with this approach, our device confines light within the dielectric semiconductor layer, and the metal loss is minimized due to the small overlap of modes with metal.

Another approach is to use a metal-coated semiconductor nanopillar [1]. This approach uses the metal to confine the light in the lateral direction and uses mode cutoff reflection in the vertical direction. Compared with this approach, our device

can improve several aspects for practical application. 1) Our device emits light from the side and light can be more easily coupled to a planar waveguide, while the pillar structure collects the light output from the bottom substrate, which decreases the collection efficiency and makes it difficult to integrate with planar waveguides. 2) Our device has a smaller field overlap with the metal, minimizing optical loss, while the pillar structure suffers a high metallic loss from the sidewall due to the large overlap of mode. 3) Our device uses cutoff in the lateral confinement. Thus, instead of relying on a precise processing, the key design parameter of semiconductor thickness is controlled during wafer crystal growth. Unlike lithography processing, controlling sizes on the order of angstroms is easily done with today's technology. On the other hand, the nanopillar requires extremely precise processing control for the pillar radius to achieve vertical cutoff on the InP cladding region, yet allowing the center InGaAs region to be not in the cutoff regime. Leading into production, this becomes a big concern for cost and yield. 4) Our device can achieve gain in the cutoff region, leading to a novel concept of mirror gain, which is completely changing the disadvantage of a large mirror loss in nanocavity to an advantage. On the other hand, in the nanopillar (InP/InGaAs/InP) structure, the cutoff reflection is achieved in the InP cladding in the vertical direction. Thus, the cutoff region cannot have gain because the electron-hole recombination occurs only in the InGaAs region. Our laser has no semiconductor active layer etching to form a cavity, which eliminates undesired surface recombination at the etching sidewall and improves heat dissipation from the active layer through single crystal phonon propagation in the lateral direction. On the other hand, all previous laser structures have semiconductor materials being etched to form the cavity. Etched surface traps electron for non-radiative

recombination and prevent lateral heat dissipation by phonons from the active layer.

In addition, our device allows for the fabrication of semiconductor lasers without dry etching semiconductor layers, which usually requires expensive equipment and environmentally toxic chemicals. This simpler processing will cut down the cost of the device fabrication.

4.2 Device Design and Analysis

4.2.1 Principle of Operation

The key physics of the cavity design is strong reflection between a dielectric waveguide and a MSM waveguide with an appropriately designed dielectric thickness. This section describes the principle of operation explaining the physics of the waveguide mode theory.

Figure 4.2 shows (a) a slab dielectric waveguide and (b) a MSM waveguide. The guiding condition of both waveguides can be solved exactly using Maxwell's equations [9]. Figure 4.3(a) represents the guiding conditions of the TE and TM modes. The guiding condition of each mode exists if it intercepts with circular curve given equation by

$$X^2 + Y^2 = R^2 \tag{4.1}$$

where R is given by

$$R = k_0 \frac{d}{2}\left(n_{core}^2 - n_{clad}^2\right)^{\frac{1}{2}} \tag{4.2}$$

and k_0 is free space wavenumber, d is dielectric thickness, and n_{core} and n_{clad} are refractive index. Since k_0, n_{core}, and n_{clad} are constants for given

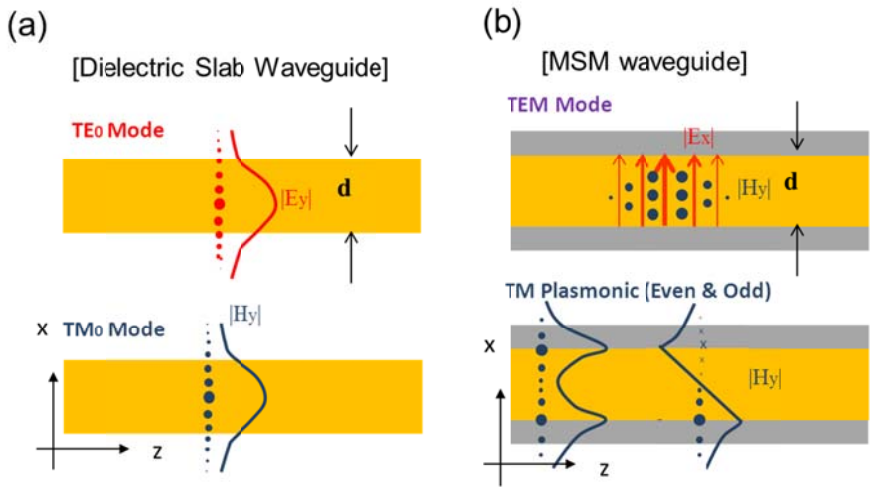

Figure 4.2 Non cutoff modes when a semiconductor thickness *d* becomes smaller for (a) a dielectric waveguide without metal, and (b) the metal-semiconductor-metal (MSM) waveguide.

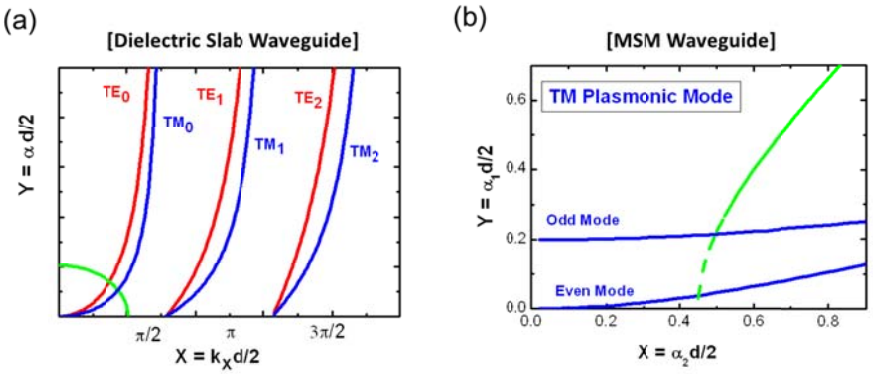

Figure 4.3 The guidance condition of (a) a dielectric slab waveguide for TE and TM modes and (b) a MSM waveguide for plasmonic TM modes.

materials and wavelength, the radius *R* decreases as the dielectric thickness *d* decreases. Eventually, all higher modes become cut off and only the TE_0 and TM_0 mode survive for a thin layer of slab waveguide. Both modes are illustrated on Fig. 4.2(a) showing the direction of field (into a paper) and the magnitude of field (cosine like modes).

In a MSM waveguide, the TE and TM modal dispersion are given in the following equations

$$k_x = \frac{\pi}{d} m \quad (m = 1, 2, ...)$$
$$k_z = \sqrt{\omega^2 \mu\varepsilon - \left(\frac{\pi}{d} m\right)^2} = \sqrt{\left(\frac{2\pi}{\lambda} n\right)^2 - \left(\frac{\pi}{d} m\right)^2} \tag{4.3}$$

where k_z is the wave number of the guided mode in the propagating direction. The cutoff condition occurs when k_z becomes imaginary number. For the lowest order of mode (m = 1), cutoff occurs when

$$d < \frac{\lambda}{2n} \tag{4.4}$$

where λ is the free space wavelength and n is refractive index of dielectric layer. This is an important design parameter. In a MSM waveguide thinner than this, no TE or TM modes are allowed to propagate. As the thickness d of MSM waveguide decreases, eventually only three modes can exist. Figure 4.3(b) illustrates the plasmonic modes, which are propagating along the interface between the metal and dielectric. As explained earlier, there is no cutoff on these modes even the thickness d approaches to zero. Together with the TEM mode, which is unique to the MSM waveguide, all three surviving modes are depicted on Fig. 4.2(b) with the field directions.

One of the most important questions is what happens when two waveguides are laterally joined together. When the thickness d is smaller than $\lambda/2n$, no TE or TM mode (except TM plasmonic and TEM modes) can exist on a MSM waveguide. If the TE or TM modes are propagating from dielectric waveguide to a MSM waveguide, they are either reflected back, or coupled to different modes, which are allowed in a MSM waveguide. The coupling strength can be described

as the integration of the mode overlap across the interface. It is seen that the TM_0 mode on the dielectric waveguide has a dominant H_y with peak at the center. This is similar to the TEM mode in a MSM waveguide indicating strong coupling between the two modes. The H_y dominant field also suggests partial coupling to two TM plasmonic modes. On the other hand, the TE_0 mode on dielectric waveguide is E_y dominant, which is orthogonal to both the TEM and the plasmonic modes (E_x dominant). Thus, coupling of the TE_0 mode into the other three modes on a MSM waveguide is negligible and most of the power is reflected back. A more rigorous and quantitative analysis of reflection is described in the following section from our theoretical analysis as well as numerical simulations.

4.2.2 Theoretical Study with Analytical Solutions

In this section, we examine the reflection strength of the fundamental TE mode between the cavity region and the cut-off region. To study the first order calculation for the magnitude of the reflection coefficient, we solved the exact solution of a pseudo structure as shown in Fig. 4.4(a). The structure consists of a hollow rectangular perfect metal filled with semiconductor material. The center region consists of the typical refractive index of InP $n_1 = 3.17$ surrounded by the different dielectric material with a refractive index n_2. In this study, we vary the refractive index of n_2 such that the lowest TE_{10} mode on this structure becomes cutoff and the excited field in the cavity has a strong reflection at the interfaces. Even though this structure is different from the real structure in Fig. 4.1, the physical principal is the same. By solving the exact analytical solution, we can obtain important insight into the physics and reach a useful optimization for the device performances.

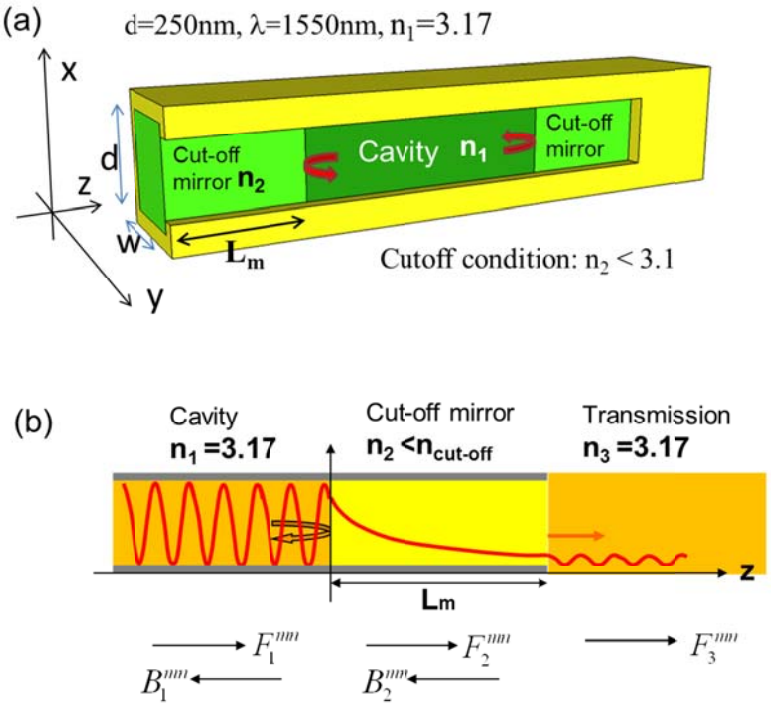

Figure 4.4 (a) Schematic of pseudo problem to calculate the reflection coefficient of the fundamental TE mode between the cavity (no cutoff) and the cutoff mirror region. (b) The electrical and magnetic field are obtainedfor each region by solving the Maxwell equations. The reflection and transmission coefficients are obtained in analytical expressions.

In this section, we solve the exact solution of three sections in the metallic rectangular waveguide as shown in Fig 4.4(b). Region 1 is the cavity with a forward wave in +z direction and a reflected wave in –z direction. Region 2 has the same dimension, but has a smaller refractive index such that the fundamental TE_{10} mode has a cutoff. In this region, the wave vector is imaginary and the field decays exponentially for both the forward and backward directions. Finally, region 3 is designed such that the refractive index is large enough so that it is not cutoff. The light transmission is coupled from this region. In this simplified problem, the electrical and magnetic fields can be solved exactly using Maxwell's equations. The general form of the TE_{mn} mode in region 1 can be written in the

following expression [10]:

$$\begin{cases} E_{1x} = \dfrac{\beta_{1y}^{n}}{\varepsilon_1}\cos\left(\beta_{1x}^{m}x\right)\sin\left(\beta_{1y}^{n}y\right)\left[F_1^{mn}e^{-j\beta_{1z}^{mn}z} + B_1^{mn}e^{j\beta_{1z}^{mn}z}\right] \\ E_{1y} = -\dfrac{\beta_{1x}^{m}}{\varepsilon_1}\sin\left(\beta_{1x}^{m}x\right)\cos\left(\beta_{1y}^{n}y\right)\left[F_1^{mn}e^{-j\beta_{1z}^{mn}z} + B_1^{mn}e^{j\beta_{1z}^{mn}z}\right] \\ E_{1z} = 0 \\ H_{1x} = \dfrac{\beta_{1x}^{m}\beta_{1z}^{mn}}{\omega\mu_1\varepsilon_1}\sin\left(\beta_{1x}^{m}x\right)\cos\left(\beta_{1y}^{n}y\right)\left[F_1^{mn}e^{-j\beta_{1z}^{mn}z} - B_1^{mn}e^{j\beta_{1z}^{mn}z}\right] \\ H_{1y} = \dfrac{\beta_{1y}^{n}\beta_{1z}^{mn}}{\omega\mu_1\varepsilon_1}\cos\left(\beta_{1x}^{m}x\right)\sin\left(\beta_{1y}^{n}y\right)\left[F_1^{mn}e^{-j\beta_{1z}^{mn}z} - B_1^{mn}e^{j\beta_{1z}^{mn}z}\right] \\ H_{1z} = -j\dfrac{\left(\beta_{1x}^{m2} + \beta_{1y}^{n2}\right)}{\omega\mu_1\varepsilon_1}\cos\left(\beta_{1x}^{m}x\right)\cos\left(\beta_{1y}^{n}y\right)\left[F_1^{mn}e^{-j\beta_{1z}^{mn}z} + B_1^{mn}e^{j\beta_{1z}^{mn}z}\right] \end{cases} \tag{4.5}$$

where ω is angular frequency, ε_1 and μ_1 are permittivity and permeability of the material, which are directly related with the refractive index n_1. The propagation constants $\beta_{1x}{}^{m}$, $\beta_{1y}{}^{n}$, and $\beta_{1z}{}^{mn}$ are determined by the boundary conditions of the rectangular waveguide as

$$\begin{aligned} \beta_{1x}^{m} &= \frac{m\pi}{d} \\ \beta_{1y}^{n} &= \frac{n\pi}{w} \\ \beta_{1z}^{mn} &= \sqrt{\beta_1^2 - \beta_{1x}^{m} - \beta_{1y}^{n}} = \sqrt{\left(\frac{2\pi}{\lambda}n_1\right)^2 - \left(\frac{m\pi}{d}\right)^2 - \left(\frac{n\pi}{w}\right)^2} \end{aligned} \tag{4.6}$$

where d and w are the dimensions in Fig. 4.4(a). Integer m and n are the mode index of the TE_{mn} mode in the x and y directions; both start from zero but cannot be simultaneously zero. $F_1{}^{mn}$ and $B_1{}^{mn}$ are the amplitudes of the forward and backward propagating waves for the TE_{mn} mode. If we assume the waveguide width w is smaller than the thickness d, the fundamental mode with the smallest cutoff frequency is the TE_{10} mode, which is what we focus on in the following analysis. The E and H fields in Regions 2 and 3 can be written by expressions

similar to Eq. (4.5). In this simplified waveguide structure, the phase matching conditions at the interfaces guarantee $\beta_{1x} = \beta_{2x} = \beta_{3x}$ and $\beta_{1y} = \beta_{2y} = \beta_{3y}$. With gain in Region 2, we can use a complex refractive index as

$$\begin{aligned} \tilde{n}_2 &= n_2 + j\kappa_2 \\ \kappa_2 &= \frac{\lambda}{4\pi} g_2 \quad . \end{aligned} \tag{4.7}$$

The tilde over n_2 indicates it is a complex number. κ is the complex part of the refractive index and it is related to the gain coefficient g as shown above. The z-directional propagation constants in three regions are, respectively,

$$\begin{aligned} \beta_{1z} &= \sqrt{\left(\frac{2\pi}{\lambda} n_1\right)^2 - \left(\frac{\pi}{d}\right)^2} \\ \tilde{\beta}_{2z} &= \sqrt{\left[\left(\frac{2\pi}{\lambda} n_2\right)^2 - \left(\frac{g_2}{2}\right)^2 - \left(\frac{\pi}{d}\right)^2\right] + j\left[\left(\frac{2\pi}{\lambda} n_2 g_2\right)\right]}. \\ \beta_{3z} &= \sqrt{\left(\frac{2\pi}{\lambda} n_3\right)^2 - \left(\frac{\pi}{d}\right)^2} \end{aligned} \tag{4.8}$$

Without gain ($g_2 = 0$), the cutoff condition is defined when propagation becomes imaginary number. In this analysis, we used $\lambda = 1550$ nm, $n_1 = n_3 = 3.17$, and $d = 250$ nm. With these values, inside of square root β_{1z} and β_{3z} are positive and the TE_{10} mode exists. When the refractive index of region n_2 falls below 3.1, β_{2z} becomes an imaginary number indicating exponential decay of the field in Region 2. By solving the continuity boundary conditions at each interface, the reflection coefficient of the cavity can be calculated from the ratio of forward and backward propagation amplitudes,

$$r = \frac{B_1}{F_1} = \frac{\left(\frac{\beta_{1z} - \tilde{\beta}_{2z}}{\beta_{1z} + \tilde{\beta}_{2z}}\right) + \left(\frac{\tilde{\beta}_{2z} - \beta_{3z}}{\tilde{\beta}_{2z} + \beta_{3z}}\right) e^{-j2\tilde{\beta}_{2z}L}}{1 + \left(\frac{\beta_{1z} - \tilde{\beta}_{2z}}{\beta_{1z} + \tilde{\beta}_{2z}}\right)\left(\frac{\tilde{\beta}_{2z} - \beta_{3z}}{\tilde{\beta}_{2z} + \beta_{3z}}\right) e^{-j2\tilde{\beta}_{2z}L}} \quad . \tag{4.9}$$

where L is the length of the cutoff region two and β_{2z} is a complex number.

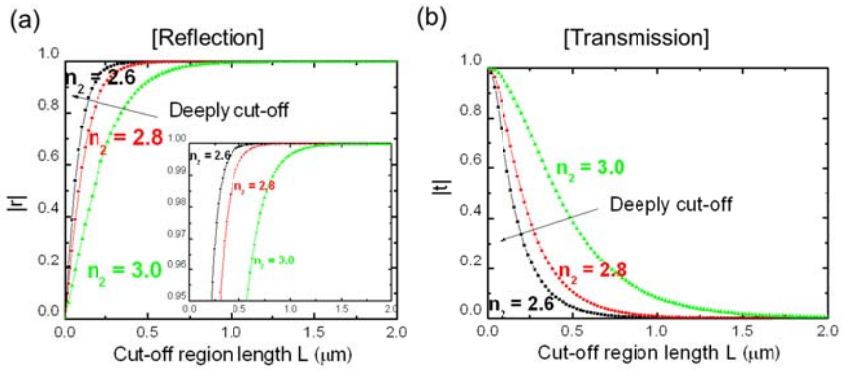

Figure 4.5 (a) Reflection coefficient and (b) transmission coefficient of the TE_{10} mode between the cavity and cutoff region as a function of the cutoff mirror length. Three curves are generated with different refractive indices in the cut-off region. There is no gain in the mirror region.

Figure 4.5(a) shows our calculated magnitude of the reflection coefficient as a function of different lengths of the cutoff region for the different refractive indices in the cutoff mirror region. No gain is placed in either the cavity or the mirror region in this calculation. For this geometry and wavelength, a TE_{10} mode becomes cutoff when n_2 become less than 3.1. The reflection coefficient approaches unity even with a 1 μm of the cutoff length. Even though this analysis is the ideal case without the metal loss and radiation loss in real devices, it is shown that the cutoff region has a very high reflectivity. When the refractive index n_2 is further reduced to deep cutoff, the reflection coefficient increases more rapidly due to the faster exponential decay of the field in the cutoff region. The transmission coefficient can be calculated in a similar manner by taking the ratio of the forward propagation amplitude in Region 3 to an amplitude of the forward propagation in Region 1 ($t = F_3/F_1$). Figure 4.5(b) shows the magnitude of the transmission coefficient into Region 3.

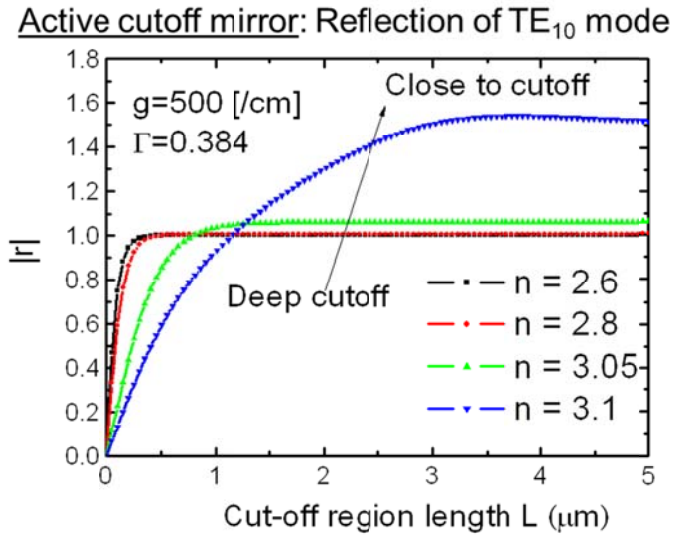

Figure 4.6 Reflection coefficient of the fundamental TE_{10} mode between the cavity and the cutoff region when gain is added to the cutoff region. The different curves are for different refractive indices in the cutoff mirror region. A material gain of 500 cm^{-1} and an optical confinement factor of 0.384 are assumed in this calculation.

One of the interesting features of the proposed device is current injection in the cutoff mirror region. Placing gain in the cutoff region is studied by adding an imaginary part of the refractive index as in Eq. (4.7). Figure 4.6 shows the reflection coefficient when gain g = 500/cm is added to the cutoff region. For the deep cutoff case with a small n_2, the result is similar to the passive cutoff mirror case. When n_2 approaches the cutoff condition, the reflection coefficient increases slowly with the mirror length L as in Fig. 4.5(a). After an enough mirror gain length is obtained, the reflection coefficient exceeds the value of the deep cutoff case and saturates above unity. With gain in the mirror, a shallow cutoff has a larger reflectivity in a long cavity because of the larger field penetration into the gain region. This suggests the novel concept of mirror gain in the semiconductor cavities. In laser theory, mirror loss at single interface is expressed as

$$\alpha_m = \frac{1}{L}\ln\left(\frac{1}{R}\right). \tag{4.10}$$

where L is the cavity length and R is the power reflection. Mirror loss represents distributed loss of electrical field as it propagates the round trip in the cavity. It affects the threshold condition of the lasers. One of the biggest challenges in the small cavity laser is the high mirror loss due to a small cavity length L. If R can be greater than unity even by a small amount, Eq. (4.10) becomes

$$R=1+\Delta$$
$$\alpha_m = \frac{1}{L}\ln\left(\frac{1}{R}\right) = -\frac{1}{L}\ln(1+\Delta) \approx -\frac{\Delta}{L}. \quad (4.11)$$

Thus, the mirror loss becomes mirror gain. As photons travel back and forth in the cavity, the magnitude is amplified each time when they are reflected. Theoretically, this gain becomes larger for a small cavity due to the more frequent amplification on the mirror, therefore, it is suitable for micro/nano-cavity small lasers.

4.2.3 Numerical Simulations

In the previous section, a theoretical study is demonstrated with a simplified structure to give the first order approximation. In this section, we show numerical simulations with two and three dimensional models using real device dimensions, refractive index, and dispersion of the semiconductor and metals. In this study, radiation losses from the top of cavity as well as metallic loss in the MSM region are taken into account. Figure 4.7 shows the (a) simulated device cross section and (b) the fundamental TE mode propagation at different thicknesses of a

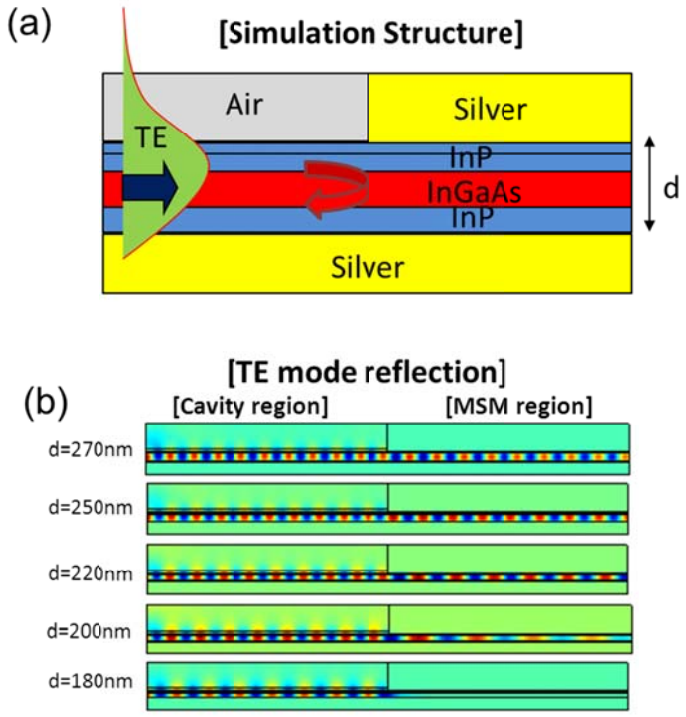

Figure 4.7 (a) Schematic of our simulation structure for the fundamental TE mode reflection between the top air (no cutoff) waveguide and MSM (cutoff) waveguide. (b) The fundamental TE mode propagation (incident from left to right) with 1.55-μm wavelength for different thickness of dielectric layers.

semiconductor layer using the finite element method (FEM). With the incidental wavelength of 1550 nm, the cutoff condition is calculated with d = 237 nm using the assumption of a perfect metal. In our numerical calculation using the real metal, a strong reflection starts to occur from around d = 190 nm, which is smaller than the calculation because there is a field penetration into the silver with a finite skin depth. In real metals, the cutoff condition cannot be exactly defined due to the strong dispersion term in the metal causing the complex wave vector. From the numerical calculation taking into account all these effects, a strong reflection of the fundamental TE mode at the interface is clearly observed when d = 180 nm.

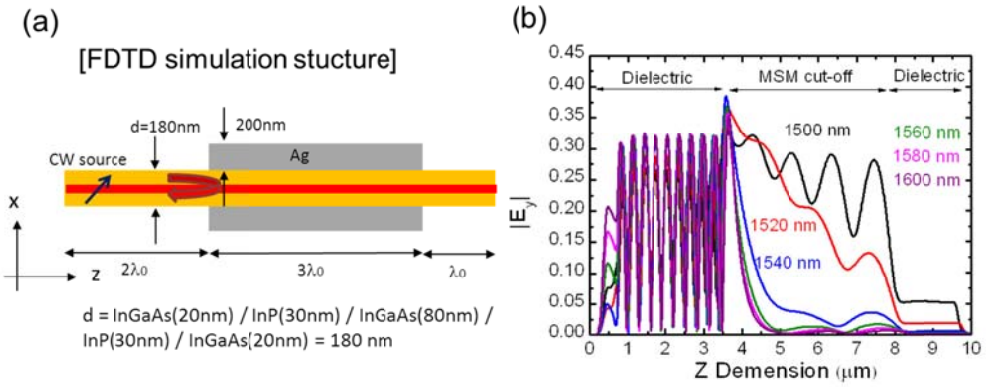

Figure 4.8 Numerical calculation of the fundamental TE mode reflection between the dielectric waveguide and MSM waveguide for different wavelengths of light.

Figure 4.8 shows our simulation results using a different (numerical) method, the finite-difference time-domain (FDTD) method, for the similar structure. In this case, the semiconductor thickness is fixed to 180 nm and the exciting wavelength is varied. As in the previous case, radiation loss in the vertical direction and the metallic loss from the silver are taken into account. Figure 4.8(b) shows the magnitude of E_y component (TE mode) on a dielectric waveguide and the MSM waveguide. Due to cutoff condition of $d < \lambda/(2n)$, shorter wavelengths penetrate more into MSM region. As the wavelength becomes longer, it becomes more deeply cutoff and the field decays more quickly. The simulation results show a clear standing-wave pattern in the cavity region showing the strong field reflection. The effective wavelength of the MSM cutoff region is much larger due to the small real part of wavenumber in the propagation direction (k_z)

$$\lambda = \frac{\lambda_0}{n_{eff}} = \frac{2\pi}{k_z}. \tag{4.12}$$

Around the cutoff condition, the propagation constant is a complex number with

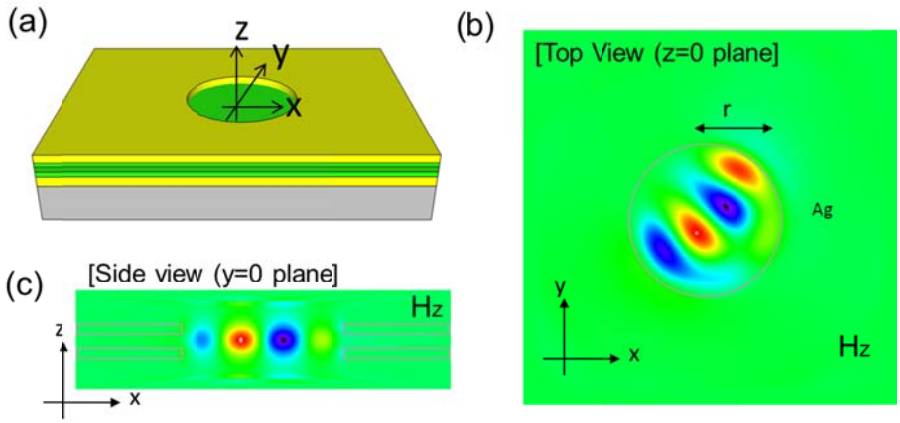

Figure 4.9 Three-dimensional numerical calculation in the circular cavity device. There is no metal in the circular region both on the top and bottom forming the cavity. The redius of the cavity is 750 nm and the semiconductor thickness is 180 nm.

the real part and the imaginary part comparable to each other. This is seen from the oscillating function with a long effective wavelength, which has a decaying envelope as in 1500 nm case in Fig. 4.8(b). As the wavelength becomes longer and the waveguide geometry gives a deep cutoff, the imaginary part of propagation constant dominates the real part, and the signal decays quickly in the mirror region.

So far, the fundamental TE mode confinement within the semiconductor waveguide is demonstrated in 2D model showing a strong reflection with the carefully engineered wavelength and semiconductor layer thickness. Now, we demonstrate our numerical simulation in the 3D model with the structure, which we actually fabricated in the cleanroom at UIUC. Figure 4.9 shows the FDTD simulation of the circular cavity with a radius of 750 nm and semiconductor thickness of 180 nm. In this model, the metallic loss from the silver and the radiation loss from the top surface are taken into account. From the side and top view of the field pattern, it is clear that the H_z dominant TE like mode (E_ϕ dominant) has strong confinement in a circular cavity. From the cavity photon

lifetime, the quality factor Q is calculated as 629, which will be enough to reach the laser threshold. The resonant wavelength of this structure is 1662 nm with a cavity volume of 0.069 λ_0^3 in terms of the vacuum wavelength. The threshold material gain is calculated from,

$$g_{th} = \frac{\omega}{\Gamma_E v_g Q} = \frac{1}{\Gamma_E v_g \tau_p}. \tag{4.13}$$

With an optical confinement factor of 0.2, the threshold gain is 1141 cm^{-1}, which is small for a nanocavity volume of the size 0.069 λ_0^3. This estimation is based on a passive cavity without gain in the cavity and mirror regions. If gain is included in the mirror region, the threshold gain can be significantly reduced by the mirror gain, as discussed earlier.

The stripe cavity as shown in Fig. 4.1 is also numerically simulated using the FEM method. Figure 4.10 shows the stripe cavity device schematics with the coordinate definition and cross-sectional views of all electrical field components. The cavity dimension is 180 nm in semiconductor thickness with a stripe width of 300 nm and a length of 1350 nm. The cavity is designed for the E_y dominant TE_{511} mode with a resonant wavelength 1585 nm and a cavity volume of only 0.018 λ_0^3. Clearly, the dominant E_y fields are strongly confined in the stripe cavity region. From the top view of E_y, there are five peaks in the x-direction and one peak in the y-direction. From the side view, there is one peak in the z-direction. One of the interesting applications of this laser includes fabrication of the multi-wavelength laser sources on a single chip. Notice that resonance wavelength is determined by the cavity length of the stripe, which is defined by the mask pattern. Since the cavity is so short and the free spectral range is very large, we can fabricate

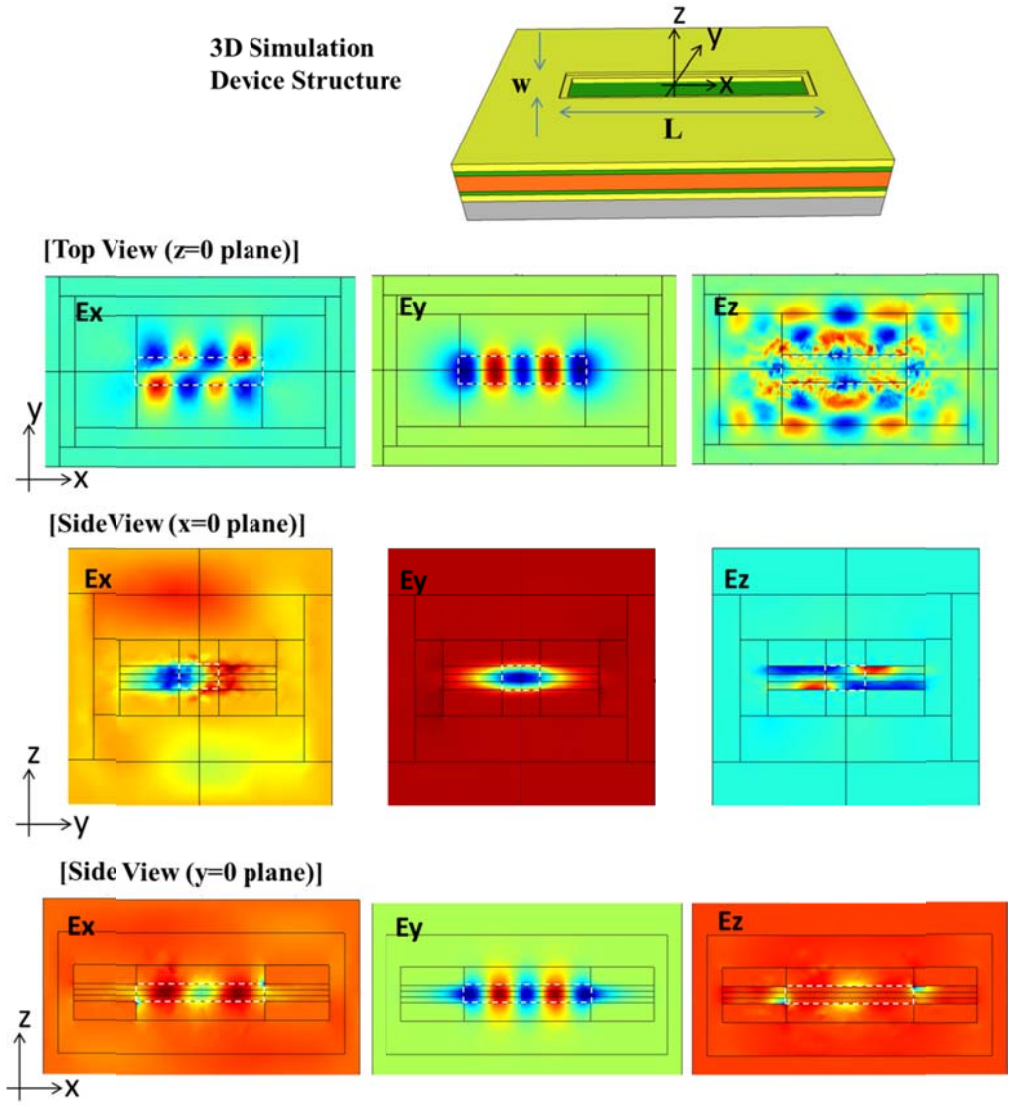

Figure 4.10 Three-dimensional numerical simulation results for the stripe cavity. The cross-sectional views for all electrical field components are shown. The cavity dimensions are: a semiconductor thickness of 180 nm, a cavity width of 300 nm, and a cavity length of 1350 nm. The cavity resonance is designed for the k_x dominant TE_{511} mode.

different lengths of cavities for different resonant wavelengths on the same wafer. This wavelength tunability by the cavity patterning has significant advantage for wavelength-division multiplexing applications in high bandwidth optical-interconnect applications.

In this simulation, all the *x*, *y*, and *z* polarization sources are used to imitate the

spontaneous emission of semiconductor. As a result, the simulation result shows several modes other than the TE_{511} mode. For example, the E_z field forms a weak standing wave in the MSM region because of the plasmonic excited electronic field, which is perpendicular to the metal-semiconductor interface.

Even though the modal cutoff provides an excellent optical confinement, one of the drawbacks of this proposed device will be a small optical confinement factor from a thin semiconductor thickness. Significant evanescent field leakage to the top and bottom of the semiconductor layer can be seen from the E_y plot on the cross-sectional view with $y = 0$ plane in Fig. 4.10. The energy confinement factor is calculated using the following equation

$$\Gamma_E = \frac{\int_{V_a} \frac{\varepsilon_0}{4} \left\{ \varepsilon_g(\omega, \mathbf{r}) + \mathrm{Re}[\varepsilon(\omega, \mathbf{r})] \right\} |\mathbf{E}(\mathbf{r})|^2 \, d\mathbf{r}^3}{\int_V \frac{\varepsilon_0}{4} \left\{ \varepsilon_g(\omega, \mathbf{r}) + \mathrm{Re}[\varepsilon(\omega, \mathbf{r})] \right\} |\mathbf{E}(\mathbf{r})|^2 \, d\mathbf{r}^3} \tag{4.14}$$

where $\varepsilon_g(\omega, \mathbf{r})$ is group permittivity. The 3D energy confinement factor of this simulated device is 0.105, which is relatively high due to the bulk active layer and is comparable with that of the conventional lasers. With a quality factor of Q = 750, the threshold material gain is 1782 cm^{-1} for a passive cavity without gain in the MSM region.

4.3 Device Fabrication

Compared with the metal-encapsulated nanolasers in the previous chapters, the fabrication of modal cutoff lasers is easier. Figure 4.11 shows the first part of the processing procedure. Since our goal is a current injection nanolaser, the wafer is grown with a thin p-i-n hetero-junction. First, a thin electrically insulating

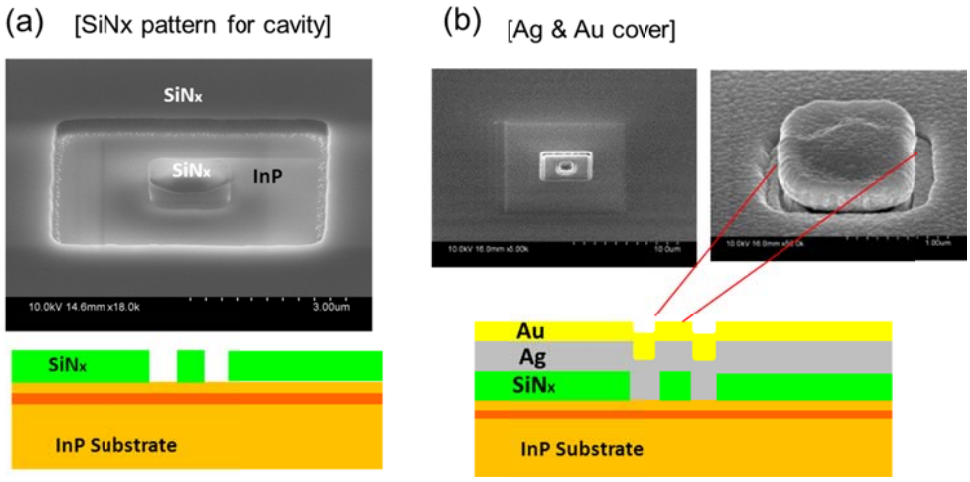

Figure 4.11 Processing procedure of a modal cutoff confinement laser: (a) cavity definition by patterning SiN_x on the top of the wafer. (b) Metal coverage to form the electrical contact as well as part of the MSM structure.

silicon nitride (SiN_x) layer is deposited on the top of the wafer. Then, the SiN_x layer is patterned with the optical lithography and partially etched away by dry etching using a nickel hard mask as shown in Fig. 4.11(a). A SiN_x island at the center serves as the cavity optical cladding layer. The outer layer of SiN_x serves as an insulator of the current injection aperture. The donut shaped InP exposed part becomes the cutoff mirror region by depositing metal on top as shown in Fig. 4.12(b). A thick silver (Ag) layer forms the MSM region as well as the contact for current injection. The SiN_x height is calculated to be thick enough such that the fundamental TE mode does not become cutoff with Ag on top of the cavity SiN_x island. Then, a thick gold (Au) layer is deposited everywhere for the wafer bonding purposes.

Figure 4.12 shows the later part of the processing procedures. The device is flip-chip bonded to any supporting substrate and the original epi-wafer substrate is removed from the top by selective chemical etching. Then, a SiN_x layer is

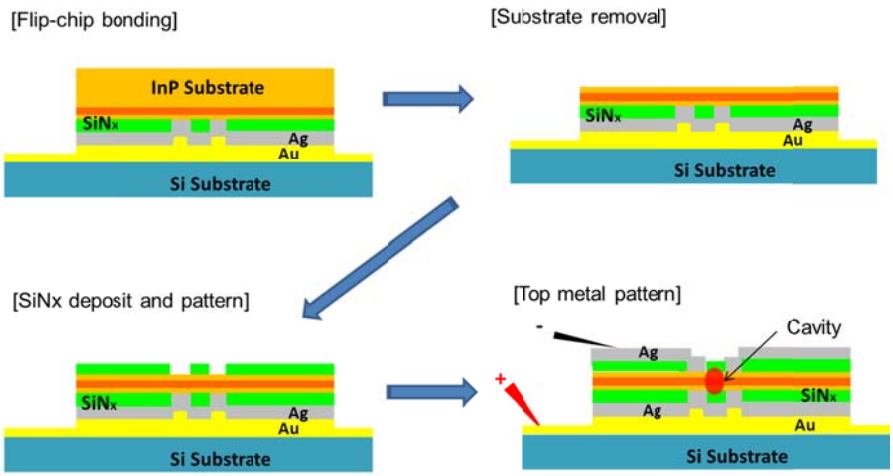

Figure 4.12 Schematic of processing for flip-chip bonding, selective substrate removal, SiNx patterning for carrier injection window, and top contact metal deposition.

deposited and patterned by the same way as the other side. Finally, the top metal (either silver of gold) is deposited with liftoff at the cavity region to form the MSM structure as well as the current injection contact. Notice the symmetric structure on the top and bottom of the semiconductor layer. This will improve the beam quality of the edge emission. The SiN_x layers on the top and bottom serve as cladding layers of the cavity in the vertical direction. Compared with air cladding, radiation leakage is suppressed and the optical confinement factor can be improved. The cross sectional schematic shows the dielectric cavity region at the center and surrounding MSM cutoff region with the electrical injection to provide a mirror gain. Figure 4.13 shows the SEM pictures of the various sizes of cavities we fabricated. Both circular and stripe cavities are fabricated with different diameters, stripe widths and lengths. As mentioned earlier, this processing is unique because it does not require etching any part of semiconductor materials. This has a significant impact on the production cost as well as the environmental safety by avoiding using toxic chemicals.

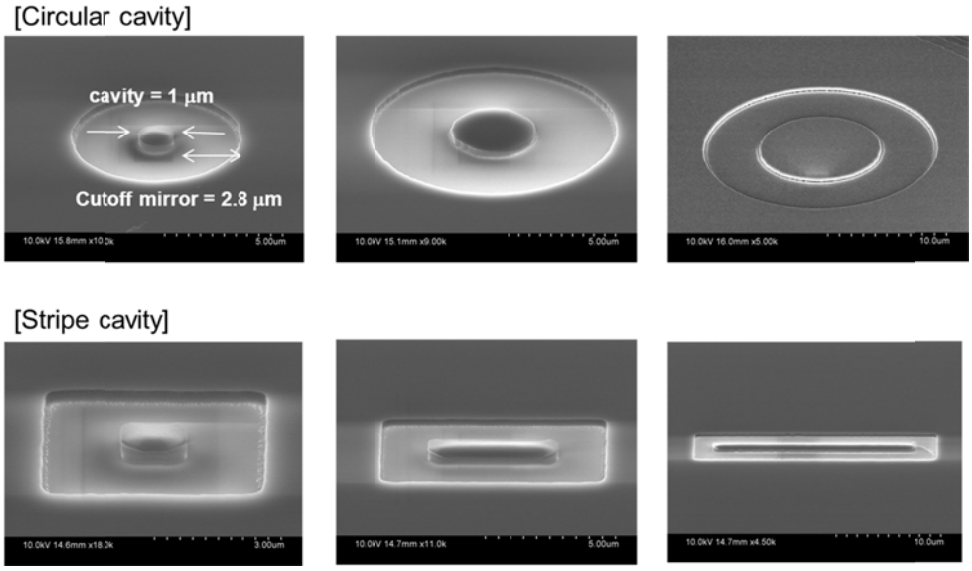

Figure 4.13 SEM pictures of various sizes of cavities. Top row pictures show circular cavity with a diameter ranging from 1.0 μm to 10 μm. Bottom row pictures show stripe cavities with various widths and lengths.

4.4 Device Characterization

One of the challenges for fabricating the active cavity devices is forming the thin p-i-n semiconductor hetero-junction with efficient carrier recombination and good optical confinement in the active layer. With the telecommunication wavelength (1.55 to 1.60 μm) using InP-based semiconductor layers (n ~ 3.17), the designed semiconductor thickness should be less than 200 nm, which already takes into account the penetration depth of optical mode into the silver layers. This is much thinner than the conventional hetero-junction thickness used in the semiconductor lasers and LEDs. We have carefully designed the epi-wafer for optimized layer thickness, material composition, and doping level to maximize the carrier recombination in the active region as well as an optical confinement factor

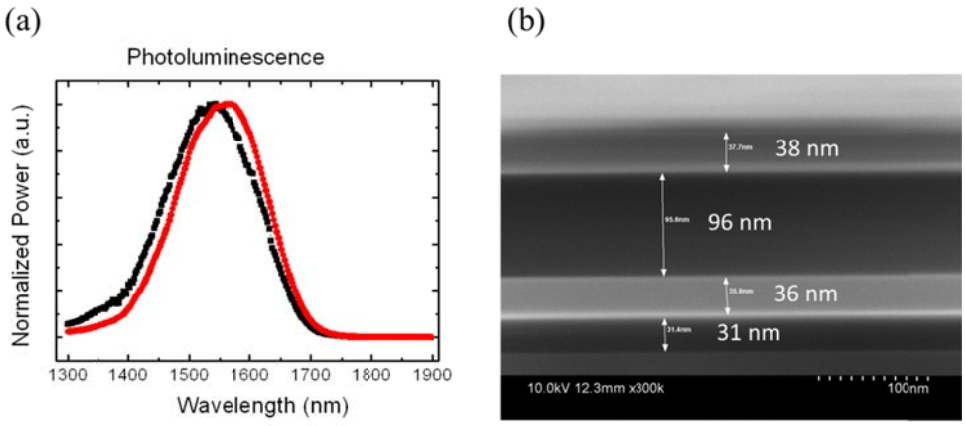

Figure 4.14 (a) Photoluminescence spectrum of our designed wafer grown by MBE with different pump powers. (b) The SEM image of the cross section of the hetero-junction. The active layer is 96-nm bulk InGaAs lattice matched to the InP cladding.

with a gain layer. Figure 4.14(a) shows the photoluminescence spectrum of designed wafer grown by MBE. From optical pumping excitation, spontaneous emission wavelength centers around 1550 nm with a small red shift with increasing pump power. Figure 4.14(b) shows the SEM cross sectional view of the sample. Cladding p-InP and n-InP layers (~ 35 nm) are kept as thin as possible to allow the thick 100 nm of bulk InGaAs in order to maximize the optical confinement factor within the design constraint.

Figure 4.15 shows the electrical and optical performance of our designed devices. The total hetero-junction thickness is only 180 nm and device is fabricated with large mesas and no cavity structure. The experiment is conducted with continuous current injection (CW) at room temperature. Three devices are randomly chosen from the different locations of the chip to compare the uniformity of the device performance. Figure 4.15(a) shows a hetero-junction diode with turn-on voltage around 0.6 V. Figure 4.15(b) shows

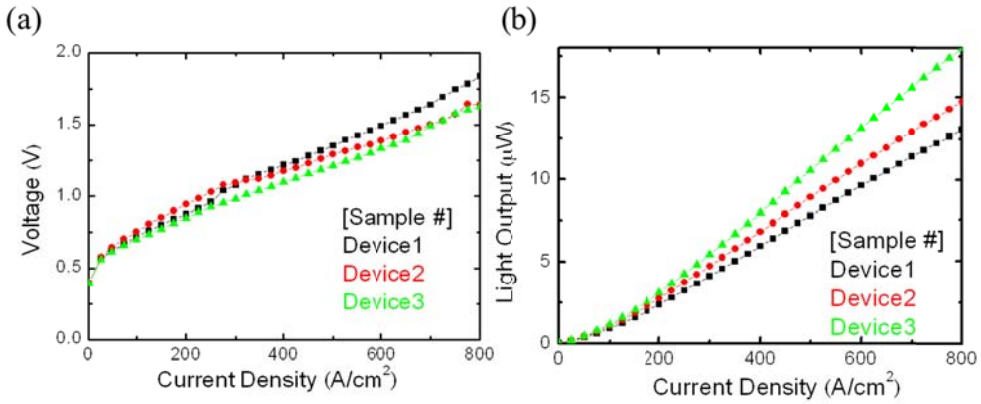

Figure 4.15 (a) Voltage vs. current density and (b) light output vs current density characterization for 180 nm thickness hetero-junction devices measured at continuous current injection (CW) at room temperature.

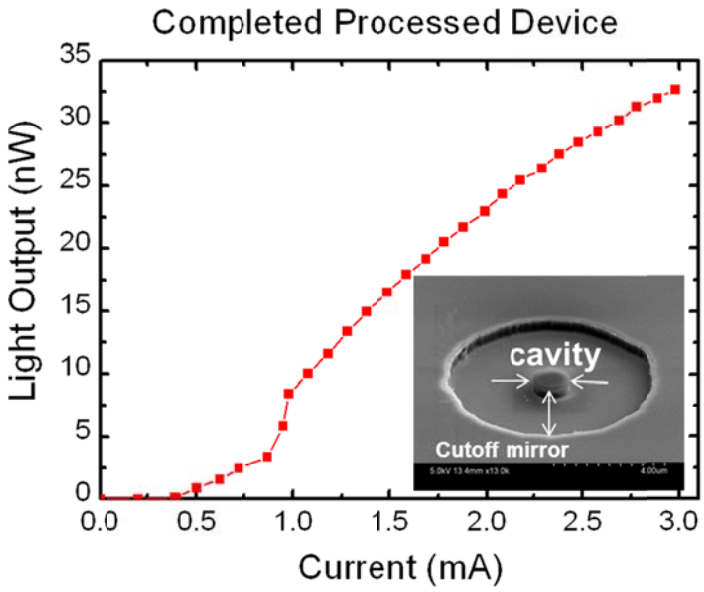

Figure 4.16 Light output vs. current for circular cavity devices. The central cavity radius is 2.5 μm. The inset SEM picture shows the cavity and cutoff mirror regions of the device.

good light output indicating effective photon generation is possible even in a thin layer of semiconductor hetero-junction.

Next, we have measured actual devices fabricated according to the processing procedures described in Section 4.3. Figure 4.16 shows the light output vs. current curve with CW injection at room temperature. The circular cavity has a radius of 2.5 μm with 200 nm silver deposited to form an MSM structure around the cavity. The cavity volume corresponds to 0.95 λ_0^3 with λ_0 the emission vacuum wavelength. A good nonlinear light output power is observed indicating potential lasing. At this stage of development, light collection efficiency is not optimized due to the geometry of circular cavity. Even though the dominant wave vector is in lateral direction, we can collect the light output only from the top of the device. As a consequence, the optical output is too weak for spectrometry characterization. We have been working to improve the processing recipes for higher yield, and a better light coupling with various stripe cavities.

4.5 Summary and Future Directions

In summary, we proposed novel nano/micro-cavity lasers using cutoff reflection of the fundamental TE mode from an MSM region. The devices are examined by multiple aspects for their function qualitatively from the principal of operation, quantitatively from the analytical study of reflection coefficient and numerical simulations by 2D and 3D models for practically designed devices. All results are consistent and they support the performance of the proposed devices. The numerical simulations including the metal loss suggest that room temperature lasing with a reasonable threshold material gain is achievable. We have also

developed processing recipes to fabricate the device without any semiconductor dry-etching process. The preliminary electrical and optical characterizations of the proposed devices are performed showing excellent I-V characteristics with a thin hetero-junction diode. The light output curve shows super-linear behavior suggesting possible lasing in the cavity volume less than λ^3. However, light output coupling and efficient current injection need to be developed.

For future directions, lateral optical output coupling needs to be improved for a better optical output collection. For example, evanescent light output coupling to a curved fiber on top of the device is a promising approach [11]. Another approach is monolithically fabricating a passive waveguide next to the edge emitting cutoff lasers for better optical output coupling as has been done in planar light-wave circuit. One of the challenges of this cutoff confinement laser is carrier injection into the cavity. As shown in the cross-sectional view of the processed device in Fig. 4.12, current is mainly injected in MSM mirror region and carrier in the cavity region might be too small to reach population inversion. The possible improvement can be made by proton implantation in MSM region using SiN_x layer as a mask. This will form the electrically insulating layer in MSM region and confine carriers in cavity region for the better gain.

Another interesting study is micro- or nanobending optical waveguide using cutoff confinement idea. Conventional semiconductor waveguides use ridge waveguide structures with cladding layers. Optical leakage at the sharp bending on the ridge waveguide is one of the important problems to solve. The photonic crystal waveguide was previously proposed for small radiation loss in a sharp bending waveguide using the photonic bandgap to confine the propagating mode in the lateral direction [12]. Cutoff optical confinement can use prohibited

propagation due to modal cutoff in the MSM region. Using cutoff confinement, which requires simply the metal patterning and the flip-chip bonding, can reduce the processing cost compared with other lasers such as photonic crystal fabrication.

4.6 References

[1] M. T. Hill, Y. S. Oei, B. Smalbrugge, Y. Zhu, T. de Vries, P. J. van Veldhoven, F. W. M. van Otten, T. J. Eijkemans, J. P. Turkiewicz, H. de Waardt, E. J. Geluk, S. H. Kwan, Y. H. Lee, R. Notzel, and M. K. Smit, "Lasing in metallic-coated nanocavities," *Nat. Photon.*, vol. 1, pp. 589-594, 2007.

[2] R. F. Oulton, V. J. Sorger, T. Zentgraf, R. Ma, C. Gladden, L. Dai, G. Bartal, and X. Xhang, "Plasmonic lasers at deep subwavelength scale," *Nature*, vol. 461, pp. 629-632, 2009.

[3] K. Yu, A. M. Lakhani, and M. C. Wu, "Subwavelength metal-optic semiconductor nanopatch lasers," *Opt. Express*, vol. 18, pp. 8790-8799, 2010.

[4] M. P. Nezhad, A. Simic, O. Bondarenko, B. Slutsky, A. Mizrahi, L. Feng, V. Lomakin, and Y. Fainman, "Room temperature subwavelength metallo-dielectric lasers," *Nat. Photon.*, vol. 4, pp. 395-399, 2010.

[5] J. Takahara, S. Yamagishi, H. Taki, A. Morimoto, and T. Kobayashi, "Guiding of a one-dimensional optical beam with nanometer diameter," *Opt. Lett*., vol. 22, pp. 475-477, 1997.

[6] L. Novotny and C. Hafner, "Light propagation in a cylindrical waveguide with a complex, metallic, dielectric function," *Phys. Rev. E*. vol. 50, pp. 4094-4106, 1994.

[7] R. F. Oulton, V. J. Sorger, D. A. Genov, D. F. P. Pile, and X. Zhang, "A hybrid plasmonic waveguide for subwavelength confinement and long-range propagation," *Nat. Photon*., vol. 2, pp. 496-500, 2008.

[8] C. Manolatou, and F. Rana, "Subwavelength nanopatch cavities for semiconductor plasmon lasers*," IEEE J. Quantum Electronics*, vol. 44, no. 5, pp. 435-447, 2008.

[9] S. L. Chuang, *Physics of photonic devices*, 2nd edition, Chapter 7, New York: Wiley, 2009.

[10] C. A. Balanis, *Advanced engineering electromagnetics*, Chapter 8, New York: Wiley, 1989.

[11] I. Hwang, S. Kim, J. Yang, S. Kim, S. H. Lee, and Y. Lee, "Curved-microfiber

photon coupling for photonic crystal light emitter," *Appl. Phys. Lett*. vol. 87, p. 131107, 2005.

[12] A. Mekis, J. C. Chen, I. Kurland, S. Fan, P. R. Villeneuve, and J. D. Joannopoulos, "High transmission through sharp bends in photonic crystal waveguides," *Phys. Rev. Lett*., vol. 77, no. 18, pp. 3787-3790, 1996.

CHAPTER 5

CONCLUSION

5.1 Summary of Key Results

In this dissertation we have examined semiconductor nanolasers and nano-light-emitters using a metal as a part of the resonant cavity. Several different cavity structures are designed, processed, and characterized for performance. Since the focus has been on an optical interconnect solution for future dense photonic integrated circuits, all devices are designed such that they can operate with electrical injection at room temperature.

We first presented metal-cavity quantum-dot surface-emitting microlasers in Chapter 2. The QD active layer is used to reduce the surface recombination rate which is severe when the micro-post diameter becomes small. Different sizes of metal-DBR cavities are fabricated with cavity volume reduction both in the lateral and vertical dimensions following our theoretical design rules to optimize the performance. Unlike the conventional air interface VCSELs, the metal-semiconductor interface design is important, especially for devices with a reduced number of DBR pairs. Among the various sizes of metal-cavity volumes, a few of the smallest devices are 1-μm in diameter with 19.5 top-DBR-pairs lasing in 0.1% pulsed mode, and 5.5 top-DBR-pairs large device can lase with CW both at room temperature. From the analysis of various sizes of diameter devices, we have found that further reduction of the diameter with a tall post encounters

significant problems with high series resistance and further reduction of DBR is also challenging because the top interface of only a few DBR with metal perturbs the resonant standing-wave phase reducing the reflectivity, and shifting the gain overlap.

To solve this problem, we have designed, fabricated, and characterized metal-encapsulated nano-light-emitters with bulk semiconductor in the active region. The first principle design rule is used to calculate the three-dimensional problem decomposed into a metal-coated waveguide problem, and we use the transfer matrix method to estimate the fundamental mode resonance and threshold conditions. The result based on this design rule agrees very well with the numerical three-dimensional calculation using the FDTD method. The device recipes have been developed by multiple iterations from the device characterization. Many improvements of the recipes developed here can be applied in the other device processing as well. The smallest metal cavity diode emitter with electrical injection is 0.086 λ_0^3 in terms of emitting wavelength at room temperature. It is shown that the series resistances of metal-encapsulated nanocavities are much smaller than the metal coated VCSEL, suppressing the heat generation for the small diameter devices. Even though the cavity mode of metal nanocavity had not been observed in the earlier stage of processed devices, the fabrication improvement shows a narrow cavity mode in the metal nanocavity with a volume of 1.23 λ_0^3 at room temperature. The cavity mode magnitude saturates with high current density by gain reduction and increase of metal loss, making it hard to reach the threshold condition. The dominant factor of high threshold gain for this device is radiation loss in the dominant wave-vector direction (vertical direction) because cavity length 'L' in this direction is so small.

Thus, it is the most important to figure out how to reduce the radiation loss in the wave propagating direction.

In practical applications, the edge-emitting nanolaser is desired for cost-effective light output coupling to planar lightwave circuit. From examining metal-encapsulated nanocavities, we have found that reflectivity saturates even with a thick layer of metal. This is due to partial transmission of field into a metal from the finite real part of the refractive index in the metal. To solve high radiation loss of the metal mirror, we propose novel nano/micro-cavity edge-emitting lasers using cutoff reflection of the fundamental TE mode from an MSM region. The devices are examined from multiple aspects for their function: qualitatively from the principle of operation, and quantitatively by the analytical study of reflection coefficient and numerical simulations by 2D and 3D models for practically designed devices. The numerical simulations including the metal loss suggest that room temperature lasing with a reasonable threshold material gain is achievable. We have also developed processing recipes to fabricate the device without any semiconductor dry-etching process. The preliminary electrical and optical characterizations of the proposed devices are performed showing excellent I-V characteristics with a thin hetero-junction diode. The light output curve shows super-linear behavior suggesting possible lasing in the cavity volume less than λ_0^3.

5.2 Future Prospects

To move forward with practical nanolasers, there are still many avenues of investigation. For metal-encapsulated nanocavity emitters, our electrical injection

spectra at room temperature show clear cavity modes, but do not reach the threshold condition. One of the potential reasons can be lack of material gain in the active layer. The device performances seem to be heavily variable from one wafer to another. This can be improved by wafer level performance evaluation to assist the quality of crystal growth. Another idea is using multiple QW active layers for better carrier confinement and gain with scarification of optical confinement factor.

The modal cutoff confinement laser is a new concept which is not previously reported. There is much room for improvement in device structural design and processing recipes. One of the immediate problems to be solved is the lateral optical output coupling. Since the modal cutoff idea can be applied for micro- or nanobending passive optical waveguide, it is natural to consider the integrated device of modal cutoff lasers with nanobending optical waveguide by patterning MSM structures. This may be the solution for ultra-dense photonic integration circuit in future, which includes millions of nanolasers transmitting optical signals through microbending waveguides confined by MSM modal cutoff. The concept of mirror gain is also fascinating topic to investigate. According to the threshold condition with mirror gain, it may be possible to have semiconductor nanolasers without gain in the cavity. Another interesting study is the high-speed modulation response by changing the mirror reflectivity in the MSM region. As a finishing remark of the dissertation, we believe that there are still many exciting topics to investigate in front of us. The future of photonics is very bright.